UNIVERSITÀ DEGLI STUDI DI PADOVA

Dipartimento di Fisica e Astronomia "Galileo Galilei"

Master Degree in Physics

Final Dissertation

Monte Carlo based dosimetry using PET/CT and SPECT/CT imaging in radiopharmaceutical therapy in the context of the ISOLPHARM project

Thesis supervisor

Prof. Marcello Lunardon

Thesis co-supervisors

Dr. Alberto Andrighetto

Prof. Giorgio Russo

Dr. Luca Morselli

Candidate

Alberto Arzenton

Academic Year 2020/2021

Contents

Abstract

The ISOLPHARM project has the aim of producing a set of innovative, high specific activity, carrier-free radioisotopes for target radionuclide therapy exploiting the ISOL technique at the SPES facility of INFN-LNL. The success of a particular radiopharmaceutical cancer treatment relies on an accurate assessment of the tissue response and toxicity. Since biological effects are mediated by the absorbed dose, which is defined as the energy absorbed per unit mass of tissue, internal dosimetry is of fundamental importance because it allows for the maximization of the therapeutic effect while minimizing the radiation burden to other organs. This thesis work consists in the calculation of internal absorbed dose, following radiopharmaceutical treatments — e.g. with ^{18}F, ^{111}In or ^{111}Ag — by means of different Monte Carlo based approaches (using the Geant4 software) coupled with PET/CT and SPECT/CT images of mice acquired by the ISOLPHARM group.

Riassunto

Il progetto ISOLPHARM nasce con lo scopo di produrre una serie di radioisotopi innovativi per l'utilizzo in terapia radiofarmaceutica sfruttando la tecnica ISOL nella facility SPES di INFN-LNL. Il successo di un trattamento radiofarmaceutico su un tumore dipende da un'accurata valutazione della risposta del tessuto e della tossicità. Poiché gli effetti biologici sono mediati dalla dose assorbita, definita come energia assorbita per unità di massa del tessuto, la dosimetria interna è d'importanza fondamentale per permettere la massimizzazione dell'effetto terapeutico minimizzando l'irraggiamento degli altri organi. Il lavoro di tesi consiste nel calcolo della dose assorbita internamente a seguito di trattamenti radiofarmaceutici — per esempio con ^{18}F, ^{111}In o ^{111}Ag — avvalendosi di diversi approcci basati sul metodo Monte Carlo (utilizzando il software Geant4) abbinato a immagini PET/CT o SPECT/CT murine acquisite dal gruppo ISOLPHARM.

Introduction

The initial part of this thesis is meant to provide the reader with some background information needed to understand properly the requirements, the choices and the strategies that will characterize the following research. In order to accomplish this purpose, the first chapter will be dedicated to a general recap of medical physics methods: after a preliminary exposition of the main radiobiological quantities at stake, an introduction to Target Radionuclide Therapy (TRT) will be given; then, an *excursus* will be held about the medical imaging techniques which will be used later in this work, i.e.:

- Computed Tomography (CT);
- Single Photon Emission Computed Tomography (SPECT);
- Positron Emission Tomography (PET).

Achieved this, Chapter 2 will introduce to the reader the story, the main goals, the research methods and the technologies involved in the INFN-ISOLPHARM project [1]. The Isotope Separation On-Line (ISOL) technique for the creation of Radioactive Ion Beams (RIBs) will be presented in detail as a fundamental feature of the entire experiment; that will be followed by an explanation of how the ISOL technique can be matched to the production of highly pure carrier-free radionuclides thanks to chemical processes and, later, of the final radiopharmaceuticals to be used in nuclear medicine for therapy, diagnosis or — as it will be shown — both at the same time.

Subsequently, the reader will be ready to face the research activities carried out in the context of this master thesis. These studies deal with dosimetric predictions of the effectiveness of innovative radiopharmaceuticals in biological tissues, in particular those of a sample of mice; the reasons why such calculation is so important to ISOLPHARM will be widely discussed in Chapter 2. The different methods used are two, and they both have recourse to medical imaging and to Monte Carlo simulations from the Geant4 software [2].

The first strategy, exposed in Chapter 3, consists in generating virtual volumes of several tissues subdivided in concentric shells or in voxels (namely 3D pixels), simulating either monoenergetic electrons or radioisotopic sources not dependent on time and building a database of mean absorbed dose per event values. These coefficients, called *Dose Point Kernels* (DPKs) in the shell case and *Voxel S-Values* (VSVs) in the voxel one, form a kernel that can be convolved with a function expressing the activity — e.g. taken from a PET or a SPECT — in order to estimate the dose absorbed by the tissues from a real source. Certain radionuclides already used in medical physics will be studied and compared with the existing literature and then the innovative species of ISOLPHARM such as ^{111}Ag will be analyzed.

Regarding the second method, which will be treated in Chapter 4, PET/CT and SPECT/CT coupled images will be exploited to reproduce virtual voxel-made murine bodies (using CT) as sensitive volumes of Geant4 and to get information about the time evolution of the activity biodistribution (PET, SPECT). In this way, the radiation dose could be directly simulated for any radionuclide inserted in a radiopharmaceutical whose biodistribution is equivalent to the ones used during the imaging processes. The final aim is to build a tool able to predict and study the dose maps that will characterize the "in vivo" experiments scheduled by the ISOLPHARM collaboration with the produced radiopharmaceuticals.

x

Part I

Scientific background

Chapter 1

Some concepts of medical physics

It is worthwhile to begin this master thesis with a short recap of certain features of medical physics that will be helpful for a complete comprehension of the following topics. First of all, some general notions about the physical quantities used in dosimetry and radiobiology will be provided; then some modern techniques of radiation therapy will be introduced, with particular attention paid to Target Radionuclide Therapy (TRT) because of its primary relevance in the ISOLPHARM experiment. Finally, as disclosed in the Introduction, the imaging techniques which may be useful for predictive dosimetry calculation will be presented in detail: we are talking about Computed Tomography (CT), Positron Emission Tomography (PET) and Single Photon Emission Computed Tomography (SPECT).

1.1 Main quantities

Since we are going to deal with medical applications of radioactivity, the first physical quantity to introduce is naturally the *activity* of a source, i.e. its radioactive decays per time unit; it can be thought as the opposite time derivative of the number of nuclides of a decaying population: calling $A(t)$ the activity and $N(t)$ the total number of undecayed nuclei at time t, we can write

$$A(t) \equiv -\frac{dN(t)}{dt} \tag{1.1}$$

In the International System of Units (SI), activity is measured in *becquerel*, defined as

$$1\,\mathrm{Bq} = \frac{1\,\mathrm{decay}}{1\,\mathrm{s}} \tag{1.2}$$

and clearly having the dimensions of an inverse time; an alternative unit is the *curie*, defined as $1\,\mathrm{Ci} = 37\,\mathrm{GBq}$. Since $N(t)$ in such systems shows a negative exponential trend

$$N(t) = N_0\, e^{-\lambda t} \tag{1.3}$$

where N_0 is the initial number of nuclides of that species and λ is the *radioactive disintegration constant* (or simply *decay constant*), the following equation holds

$$A(t) = -\frac{d}{dt}\big(N_0\, e^{-\lambda t}\big) = \lambda N_0\, e^{-\lambda t} = \lambda N(t) \tag{1.4}$$

meaning that, if $A(t)$ is measured from a source of a known species, we also know the number of nuclei $N(t)$, being λ a constant. The latter can be related as well to observable quantities, since defining the two time quantities *mean lifetime* τ and the *half-life* $t_{1/2}$ we have

$$\lambda = \frac{1}{\tau} = \frac{\ln 2}{t_{1/2}} \tag{1.5}$$

In particular $t_{1/2}$, which represents the time after whom the initial population is halved, is of great importance for the nuclide selection in nuclear medicine. As we will show in the fourth chapter, the

Particles	w_R
γ	1
e, μ	1
p, charged π	5
α, heavy ions	20
n	2.5÷21

Table 1.1: Typical values of w_R. [3]

concentration of a (radio)pharmaceutical in a tissue follows a similar decay trend due to the biological elimination of the "foreign" substance.

Let us now focus on dosimetry, the branch of medical physics that studies the effects of ionizing radiation on organic (or organic-like[1]) matter. The most general physical quantity in this sector is the *absorbed dose*, corresponding to the energy released by the incident radiation per mass unit. Again, in the SI, the used unit is the *gray*, defined as

$$1\,\text{Gy} = \frac{1\,\text{J}}{1\,\text{kg}} \tag{1.6}$$

However, even though it would already be an appropriate indicator for this work, which does not include clinical analyses but only dosimetric predictions, this quantity shows some limits; as a matter of fact, no information is provided about neither the nature of the radiation nor the radiosensitivity of the irradiated tissue. Another factor which is not considered by the absorbed dose is the irradiation time, but trivially if an absorbed dose D is reached in $1\,\text{s}$ rather than in $1\,\text{h}$, the tissue's response could become slightly different, as the cells would have less time to repair eventual sublethal damage in their DNA (*dose-rate effect*).

In order to solve the first two problems, mostly in the radiation protection sector two variants of the absorbed dose are used. The *equivalent dose* is defined as the absorbed dose multiplied by a weighting factor w_R associated to the type of radiation R; assuming that a volume is irradiated by different contributions, the formula reads

$$H = \sum_R w_R\,D_R \tag{1.7}$$

where D and H indicate the absorbed and equivalent doses. In the same way, one can append another weighting factor w_T depending on the irradiated tissue, obtaining the *effective dose*, E:

$$E = \sum_{R,T} w_R\,w_T\,D_{R,T} = \sum_T w_T\,H_T \tag{1.8}$$

Typical values of the weighting factors w_R and human w_T are reported in Tables 1.1 and 1.2. Since these factors are dimensionless, the equivalent and effective doses maintain the same dimensions as the absorbed one, i.e. those of an energy divided by a mass, but in order to distinguish them a different SI unit is formally used instead of the gray: the *sievert*, Sv. Anyway, as already said, using just activity and absorbed dose will be enough in our context. [3] [4] [5]

1.2 Radiobiology

This section's goal is to describe briefly and qualitatively the mechanism laying under the cellular damage caused by an incident ionizing radiation. When a ray hits a cell, the energy deposition inside it generates a plenty of free radicals and reactive oxygen species, like hydroxyl groups and peroxides, which are highly reactive and difficult for the cell to dispose of. The situation worsens if the radiation hits and mutilates DNA in the cell nucleus: even though the cell is generally capable to repair damages affecting just one DNA strand by reading the complementary information contained in the

---

[1]As we will se, water often represents a good approximation for some biological tissues.

Human tissues	w_T
Bone marrow, colon, lung, stomach, breast, remainder tissues (6)	0.12
Gonads (1)	0.08
Urinary bladder, esophagus, liver, thyroid (4)	0.04
Bone surface, brain, salivary glands, skin (4)	0.01
Total (15)	1

Table 1.2: Typical values of human w_T; the nomenclature *remainder tissues* includes: adrenals, extrathoracic region, gall bladder, heart, kidneys, lymphatic nodes, muscle, oral mucosa, pancreas, prostate (male), small intestine, spleen, thymus and uterus/cervix (female); the number of organs in each group is in brackets. [3]

other one, a high concentration of free radicals can interfere and hinder this process; moreover, if the incoming radiation mutilates both strands in the same positions, repairing without errors becomes almost impossible. These situations then lead to chromosomal aberrations, which can result lethal for the cell itself at the division stage.

It is clear that the intracellular concentration of oxygen plays an important role in the cell response to radiation, as the indirect damage induced by free radicals are estimated to contribute to about 2/3 of the total; experimentally, hypoxic[2] cells (e.g. certain kinds of tumour) show increased resistance to radiation with respect to oxygenated ones. Such effect can be quantified through the so-called *oxygen enhancement ratio*, OER $= D_{hyp}/D_{oxy}$, which is an index comparing the absorbed dose required by populations of hypoxic and aerated cells to attain the same damage quantified in cell death, or the same *surviving fraction*.

In addition to cell death, which can be practically considered as a deterministic effect of radiation happening when a certain threshold of absorbed dose is overtaken, from a medical and radioprotection point of view one must take into account the stochastic mutation effects; such events have no threshold and can lead to serious pathologies like cancers, cataract or heritable diseases (if germ cells are interested), their incidence increasing linearly with the absorbed dose. For this reasons, in every branch of medical physics involving ionizing radiation, it is always fundamental to avoid or at least to minimize the risks resulting from events hitting healthy tissues. [4] [5]

1.3 Therapy

The chance of curing cancer by means of ionizing radiation is one of the greatest results of applied physics and is probably in the forefront of today's scientific and technological progress. Mankind discovered that ionizing radiations may have a therapeutic effect by the end of the XIX century, when the Austrian surgeon Leopold Freund managed to remove a hairy mass from a patient by using X-rays in 1896. In the following decades, such treatments were extended to more dangerous tumours and embraced different kinds of radiation sources. Nowadays, there are several therapies adopted to treat diverse types of cancers; at the most general level, we can identify two approaches: External Beam Radiation Therapy (EBRT) and Internal Radiation Therapy (IRT).

EBRT makes use of beams especially of X-rays or electrons, but therapies with neutrons, protons or heavy ions — constituting the so-called *hadron therapy* — are as well available in a limited number of infrastructures all around the world. The mechanism of these therapeutic procedures is to hit a localized tumour exactly where the energy loss of the incident particles is maximized; as an indicator of it, we can define the *stopping power*, S, as the opposite space derivative along the beam direction x of the energy of the incident particles E:

$$S(x) = -\frac{dE(x)}{dx} \tag{1.9}$$

In fact, for each kind of radiation, the stopping power shows a maximum that may correspond to different levels of penetration along x, depending on the particle species, on its energy and on the density

---

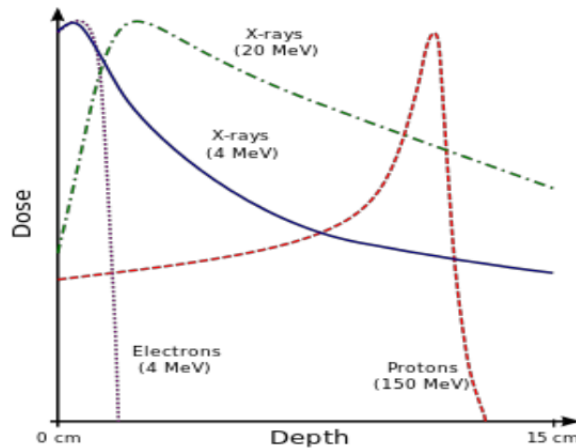[2]Presenting *hypoxia*, i.e. lack of oxygen.

Figure 1.1: Examples of dose-depth curves of incident X, e$^-$ and p rays; the p curve shows Bragg's peak. [6]

and composition of the material. Generally, electrons and photons lose most of their energy next to the surface of incidence, while protons and other charged ions show a quite sharp peak, called *Bragg's peak*, just before the energy gets completely lost, hence at higher depths (Figure 1.1). In conclusion, medical physicists and radiotherapists have the chance to choose among several fashions of therapies with different particles at different energies, in order to assess the best treatment for any localized cancer. Of course, it is fundamental to obtain stopping power peaks which are as sharp as possible and to lower the rest of the $S(x)$ curve, in order to avoid dose deposition on the surrounding healthy tissues as far as possible; this is achievable by accurately creating monochromatic beams by means of scattering foils or magnetic fields. Furthermore, narrowing the beams with collimators prevents excessive lateral scattering. Modern techniques permit to select a treatment starting from the dose requirement and producing an adequate beam; this is the case of Intensity Modulated Radiotherapy (IMRT), which allows to irradiate the patient from different directions, and Image Guided Radiotherapy (IGRT), which exploits the morphological information provided by an associated imaging tool. Concerning IRT, the first method we are exposing is *brachytherapy* (or *endocurietherapy* after Marie and Pierre Curie). It was the first invented IRT, dating back to the early 1900s, and consists in placing directly a radioactive source inside the oncological patient; this is possible in two modes:

- intracavitary brachytherapy, positioning the radiation source in cavities next to the tumour (common strategy for cervical, prostate and esophageal cancer);

- interstitial brachytherapy, inserting the source just inside the cancer, using radioactive needles or wires.

Obviously, these methods are again referred to localized cancers and provide a high dose only to the immediate source surroundings. But is it possible for radiation to act even on diffused tumours? With γ-emitting radiotracers, as we will see in the next section, one can localize a cancer through molecular receptors. Similar mechanisms can be extended as well to therapeutic radionuclides with α, β^- or Auger radiation, and in fact another kind of IRT, called Target Radionuclide Therapy (TRT), Radiopharmaceutical Therapy (RPT) or Molecular Radiotherapy (MRT), is currently developing and is considered very promising. Due to its huge relevance in this thesis work, TRT deserves a more detailed description that will be offered in the following paragraph. [7]

1.3.1 Target Radionuclide Therapy (TRT)

As anticipated, several species of radioactive nuclei can be administered to the patients, either orally or intravenously; they have to be bound to more or less complex molecules, whose task is to transport the nuclei towards and into the target organs. The first radionuclide to be ever injected in a living thing for scientific or medical purposes was ^{212}Pb, used as a radiotracer in 1923 by the Hungarian radiochemist George de Havesy during his researches on the metabolic processes of the plant *Vicia faba* (vulgarly *broad bean*); his studies were awarded with the Nobel Prize in Chemistry in 1943.

Radiation	E_m	R	LET	Examples of emitters
α	$3 \div 6\,\mathrm{MeV}$	$28 \div 100\,\mu\mathrm{m}$	$80 \div 240\,\mathrm{keV}/\mu\mathrm{m}$	^{211}At, ^{223}Ra, ^{225}Ac
β	$0.1 \div 2.2\,\mathrm{MeV}$	$2 \div 10\,\mathrm{mm}$	$0.1 \div 1\,\mathrm{keV}/\mu\mathrm{m}$	^{90}Y, ^{131}I, ^{177}Lu
Auger	$1 \div 10\,\mathrm{keV}$	$< 5\,\mu\mathrm{m}$	$4 \div 26\,\mathrm{keV}/\mu\mathrm{m}$	^{111}In, ^{123}I, ^{125}I

Table 1.3: General features of the radiations used in TRT. [4]
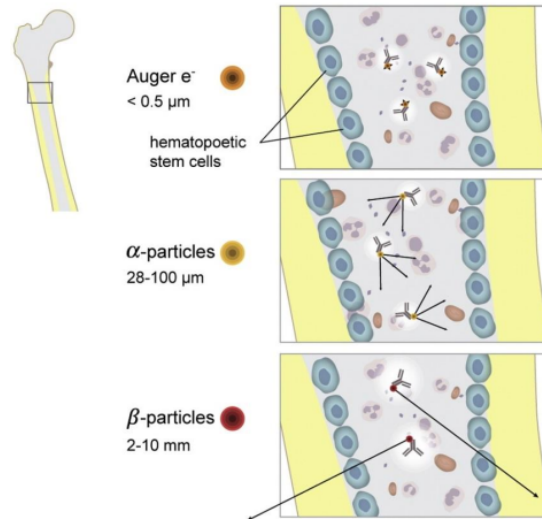
Figure 1.2: Illustration of α, β^- and Auger e$^-$ ranges for TRT in bone tissue. [8]

The very first target therapeutic treatment on a human patient instead dates back to 1941, when the American doctor Saul Hertz cured a patient suffering from Graves' disease, a form of hyperthyroidism, with a mixture of ^{130}I and ^{131}I; later, in 1951, radioactive ^{131}I-NaI was approved by the Food and Drug Administration (FDA), and it may be also considered the first *theranostic*[3] radionuclide, since it combines a β^- radiation, usable in therapy, with a following γ emission, suitable as radiotracer, when decaying to its isobar ^{131}Xe; with both properties, one can monitor if the dose is being released in the correct sites and how much. Anyway, theranostic radiopharmaceuticals can also contain different isotopes or even different elements, having separate therapeutic and diagnostic contributions.

In conditions of hyperthyroidism, one can exploit the huge concentration of sodium in the ill thyroid and the simple ionic bond between sodium and iodine to take the radioactive drug into the organ; however, different pathologies may need different radionuclides to be treated effectively, together with molecules suitable to bring them to their final destination. As for the nuclides, at least two main features must be taken into account: the mean emission energy E_m, which is strictly connected to the dose that will be absorbed by the organic tissues, and the half-life, which has to guarantee that the radionuclide does not decay immediately after its production but also that it will not stay for too much time in the patient's body; typical half-life values range from a few hours to a few days. Furthermore, a short radiation range R is usually required in therapy to accompany the high degree of selectivity reached by the carrier molecules and avoid rays escaping to healthy tissues. Finally, the *linear energy transfer* LET $= \frac{dE(l)}{dl}$, defined as the energy absorbed by the medium per unit path length l — similar to the stopping power but evaluated from the material's (and not the radiation's) point of view — plays an important role since it determines the effectiveness of the radiation in damaging the DNA of the cancer cells.

Finally, Table 1.3 reports the main features of the emissions used in TRT; as we can see, α and Auger particles show higher LET and lower R with respect to β, which are anyway more energetic than Auger electrons. Some radioisotopes, mostly α-emitters such as ^{225}Ac, generate radioactive daughters that can present therapeutic effects themselves. We can notice as well that the Auger range is comparable with the cell diameter, therefore it is necessary for an Auger treatment to bring the radionuclides

---

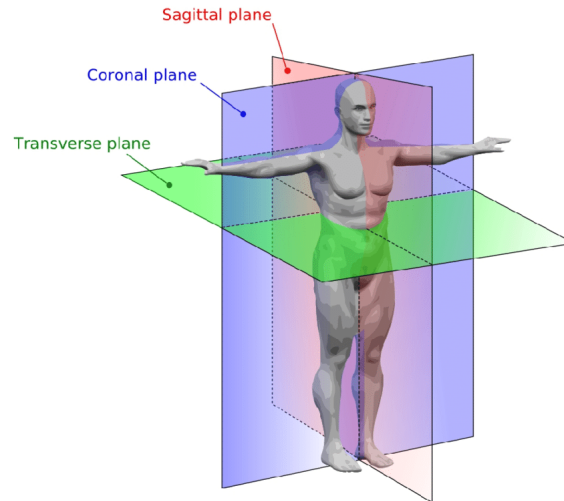[3]Or *theragnostic*: both therapeutic and diagnostic.

Figure 1.3: The three anatomical planes: *transverse*, *coronal* and *sagittal*. [10]

inside the nuclear membrane or at least inside the cell; once there, a single nucleus can emit up to a few dozens of e^-. A particular behavior belongs to the β^+ decay: due to the annihilation of the emitted positron with an electron, it generates in most cases a couple of collinear photons which make β^+ suitable for diagnostic and theranostic applications. [4]

1.4   Diagnostics

Medical physics is present in several sectors of medicine beyond oncology, if one considers the plenty of diagnostic technologies we can rely on nowadays, for instance in orthopedics or in gynecology; very simply, the possibility to look inside the patient's body and obtain morphological and functional information without physically opening it has been playing a revolutionary role in modern medicine. The methods used in the daily routine of our hospitals involve Nuclear Magnetic Resonance (NMR), ultrasounds and infrared imaging, but in this work our attention must be focused on the techniques exploiting ionizing radiations and descending from the traditional X-ray radiography, i.e. CT, SPECT and PET, since they can be used in order to achieve dosimetric calculation.

1.4.1   Radiography

The first medical application of X-rays was historically radiography, invented by the British doctor John Hall-Edwards in 1896, just one year after the X-rays were discovered by Wilhelm Röntgen. Its working principle is the following. An X-ray tube accelerates electrons emitted from a cathode filament by thermionic emission towards an anode made of heavy metals; when these projectiles collide with the anode, X-rays are produced by Bremsstrahlung or by orbital transitions following e^- e^- scattering. Part of this radiation passes through a window, gets adequately filtered and reaches the patient's body. Now, if we call I_0 the initial intensity of X-ray beam, when penetrating in a tissue along direction x it will decrease as

$$I(x) = I_0\, e^{-\mu x} \tag{1.10}$$

where μ represents the *linear attenuation coefficient* and depends on the tissue and on the incident energy. Image receptors, like traditional films or modern detectors, positioned on the other side of the patient, reveal the intensity getting out of the body and reconstruct a 2D image whose brightness is proportional to the registered μ. Filtering is really important not only to obtain a clean signal but also because the lower energies would never leave the patient's body, just resulting in useless ionizing radiation dose; in order to achieve a high degree of cleanness, an anti-scatter grid is also placed between patient and detector. The evolution of this method has brought technologies such as *fluoroscopy*, which allows a real time visualization of the interesting body region, *angiography*, permitting to see the blood
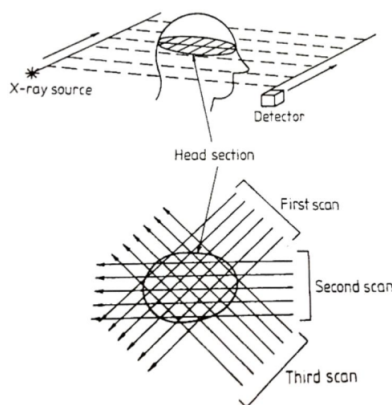
Figure 1.4: Basic working principle of the CT scan. [9]

vessels thanks to a radiopaque[4] contrast agent, *mammography* and of course CT. [9]

1.4.2   Computed Tomography (CT)

Like classic radiography, CT uses X-rays and provides morphological images of the patient's body, but this time in 3D. The underlying concept of tomographic reconstruction was formalized by the Austrian mathematician Johann Radon in 1917, but developed at medical level only in 1972 by the British engineer Godfrey Hounsfield and the South African physicist Allan MacLeod Cormack (winners of the Nobel Prize in Physiology or Medicine in 1979). Its strategy is to produce a series of sliced images ("tomography" comes from the Greek words *tómos*, "slice", and *gráphó*, "writing") lying on one of the three anatomical planes (Figure 1.3), usually the transverse one, using external planar X-ray beams from multiple directions around the body. Figure 1.4 schematically represents the essence of the CT working principle.

From a mathematical point of view, processing the acquired data is not immediate, since we are interested now in a more precise assessment of the linear attenuation coefficient $\mu = \mu(x,y)$ as a function of the scanning plane. Let us call θ the scanning angle, for whom it will be sufficient to be $\theta \in [0, \pi)$ to avoid redundant information, and r the proper spatial coordinate of the scan (see Figure 1.5). The imaging process gives us a set of intensity profiles, one for each θ: calling L the scanning line corresponding to (θ, r) and ds its infinitesimal line element, one has

$$I_\theta(r) = I_0 \, e^{-\int_L \mu(x,y) \, ds} \tag{1.11}$$

from which one can find the total attenuation profiles, namely

$$p_\theta(r) \equiv -\ln \frac{I_\theta(r)}{I_0} = \int_L \mu(x,y) \, ds \tag{1.12}$$

To make sense, we need a new frame of reference for $\mu(x,y)$; we can choose the r coordinate and the new s coordinate, perpendicular to r and parallel to L (see again Figure 1.5, where L can be assimilated to the $\overline{AB}$ segment). It is easy to see that the frame (r,s) differs from (x,y) by a rotation θ, so the transformation matrices will be

$$\begin{pmatrix} r \\ s \end{pmatrix} = \begin{pmatrix} \cos\theta & \sin\theta \\ -\sin\theta & \cos\theta \end{pmatrix} \begin{pmatrix} x \\ y \end{pmatrix} \tag{1.13}$$

and, with $\theta \to -\theta$,

$$\begin{pmatrix} x \\ y \end{pmatrix} = \begin{pmatrix} \cos\theta & -\sin\theta \\ \sin\theta & \cos\theta \end{pmatrix} \begin{pmatrix} r \\ s \end{pmatrix} \tag{1.14}$$
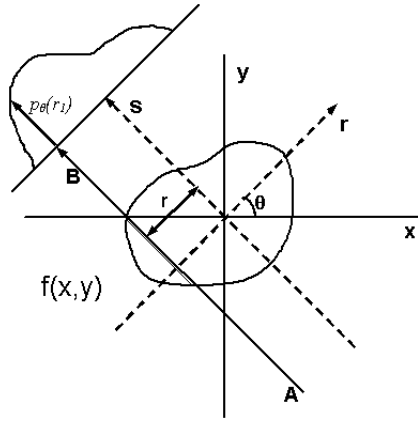
---

[4]With the property of absorbing X-rays.

Figure 1.5: Reference frames used in a tomographic reconstruction. [11]

which applied to Eq. 1.12 gives

$$p_\theta(r) = \int_L \mu(r\cos\theta - s\sin\theta,\, r\sin\theta + s\cos\theta)\, ds \tag{1.15}$$

The complete set of all the $p_\theta(r)$ projections is called *sinogram*, whereas $p_\theta(r)$ is also indicated as the *Radon transform* of the function μ, $\mathcal{R}[\mu(x,y)]$. However, what we are looking for is $\mu(x,y)$, thus we need a strategy to evaluate the Radon anti-transform

$$\mu(x,y) = \mathcal{R}^{-1}[p_\theta(r)](x,y) \tag{1.16}$$

The *projection-slice theorem* can help us to perform this calculation, as it states that the 1D Fourier transform of our projection (normalization constants set to 1)

$$\mathcal{F}_1[p_\theta(r)](k) = \int_{-\infty}^{+\infty} p_\theta(r)\, e^{-2\pi i k r}\, dr \tag{1.17}$$

is equivalent to the 2D Fourier transform of the unprojected function $\mu(x,y)$

$$\mathcal{F}_2[\mu(x,y)](k_x, k_y) = \int_{-\infty}^{+\infty} \int_{-\infty}^{+\infty} \mu(x,y)\, e^{-2\pi i (k_x x + k_y y)}\, dx\, dy \tag{1.18}$$

being $k_x = k\cos\theta$ and $k_y = k\sin\theta$. If the latter identities for k_x and k_y hold, one can check that, applying them in Eq. 1.18 and changing the coordinates $(x,y) \to (r,s)$, Eq. 1.17 can be obtained (note that the determinant of the transformation matrix is equal to 1).
Therefore, if we compute $\mathcal{F}_1[p_\theta(r)]$ in a polar grid for all the (θ, r) couples available by our CT device, those values will correspond to $\mathcal{F}_2[\mu(x,y)]$; at this point, an inverse 2D Fourier transform will yield

$$\mathcal{F}_2^{-1}\big[\mathcal{F}_2[\mu(x,y)]\big] = \mu(x,y) \tag{1.19}$$

After this back-projection process, which can be accomplished by means of several algorithms and filters, the result is a detailed, highly defined (resolution even better than 1 mm of pixel size) 2D image in the form of a matrix. Repeating this operation for more slices, one builds a 3D tensor (specific formats are used, like the DICOM files, dcm), whose elementary cells take the name of *voxels*. The coefficients stored in the voxels are traditionally the *Hounsfield units*, defined as

$$\text{HU} = 1000 \cdot \frac{\mu - \mu_w}{\mu_w - \mu_a} \tag{1.20}$$

where μ, μ_w and μ_a are respectively the linear attenuations of the assigned voxel, water and air (μ_a is actually very close to 0 and is often neglected) for the radiation used. [9]

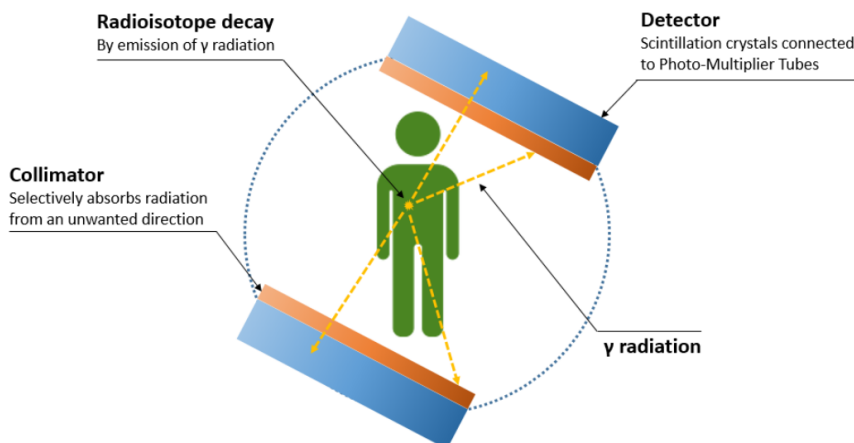**Single-Photon Emission Computed Tomography (SPECT)**

Figure 1.6: Essential schema of the SPECT working principle. [14]

1.4.3   Single Photon Emission Computed Tomography (SPECT)

After viewing the morphological imaging methods that will be used in this study, a short introduction to functional imaging techniques exploiting ionizing radiations is necessary. The purpose of a functional analysis is to provide, rather than anatomical details, information about the behavior of certain organs or tissues. For instance, the methods we are going to expose allow to locate tumour masses amongst the patient's body. They are enormously important in this research for two reasons:

- they can be combined with morphological imaging in order to carry out dosimetric assessments;

- one of the goals of the ISOLPHARM project is to produce radiopharmaceuticals suitable for this kind of analyses.

Like in TRT, the radionuclides used for diagnosis should have a half-life of at least some hours and not longer than a few days. The molecular transport mechanisms are basically the same, with the drug binding the target and irradiating, but a big difference regards the radiation that can be used, which must be traceable and is typically γ. As a matter of fact, γ-rays are way more penetrating than the other emissions, hence they deposit less energy in the patient and have by far a higher probability to exit and reach the detectors. As said at the end of the TRT paragraph, also β^+ decays are accepted in these field because of the consequent $e^+ e^- \rightarrow 2\gamma$ annihilation. The earliest technique following this principles was *scintigraphy*, born in the '50s, which provides 2D images by collecting γ decays in the so-called *γ-camera*, a device containing collimators (to ensure that the counted events come exclusively from the desired direction), scintillation detectors and photomultipliers.

SPECT imaging was invented in 1962 by David Edmund Kuhl, an American doctor specialized in nuclear medicine. Multiple γ-cameras are placed all around the patient similarly to the CT case, but this time, since radiation comes from the inside, an angle of 2π must be covered (Figure 1.6). Like in CT, a 2D sinogram is built, but a simple back-projection reconstruction is no longer precise enough, due to the uncertainty on the emitting position. To solve such a problem, the Maximum Likelihood – Expectation Maximization (MLEM) method has been developed; this procedure, formalized by Dempster, Laird and Rubin in 1976, follows a Bayesian approach and iteratively maximizes the probability for the image to be correct if a given value is measured. The iterative formula yielding the radioactivity distribution in a pixel Λ_j is the following:

$$\Lambda_j^{new} = \frac{\Lambda_j^{old}}{\sum_i c_{ij}} \sum_i \frac{c_{ij}\, q_i}{\sum_k c_{ik} \Lambda_k^{old}} \tag{1.21}$$

where c_{ij} represents the probability for the pixel Λ_j to contribute to the sinogram bin i and q_i is the number of counts in i. Repeating the process for subsequent planes one finally arrives to a voxelized
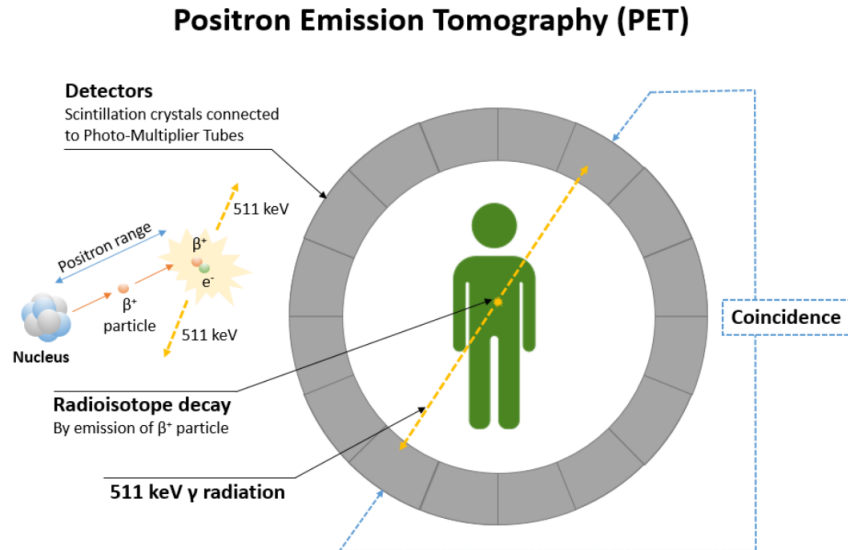
Figure 1.7: Essential schema of the PET working principle. [14]

3D image.

Obviously, also in SPECT imaging one has to face the different attenuations of the biological tissues, as γ radiation is not 100% penetrating, especially in dense materials like bones or teeth. The information needed is gained from preliminary tests with external sources, as well as from CT images: in the latter case, we can talk about hybrid SPECT/CT imaging, for whom an attenuation correction can be managed taking the μ values directly from the Hounsfield units. Finally, since we are actually discretizing a continuous distribution, an application of the *Nyquist-Shannon sampling theorem* for signal processing sets a lower limit for the number of angular detecting positions n around the patient: calling d the slice diameter and a the pixel size, this limit is established by

$$n \geq \frac{\pi d}{2a} \tag{1.22}$$

The most used pure γ-emitter in this sector is certainly ^{99m}Tc, a metastable nucleus decaying to its ground state (g.s.) ^{99}Tc with $t_{1/2} = 6.0072$ h and $E_m = 142.6836$ keV. Another example, that will return later, is ^{111}In, undergoing electron capture (EC) in $t_{1/2} = 2.8047$ d towards the stable nuclide ^{111}Cd, which de-excites with an appreciable γ radiation in the $100 \div 300$ keV window, optimal for radiodiagnostics. [4] [9] [12]

1.4.4 Positron Emission Tomography (PET)

Another phenomenon which can be exploited in order to achieve functional diagnostic tests is the positron emission by β^+ decay; this is what happens in PET imaging, that was developed in different stages from the early '50s to the middle of the '70s. The main, big advantage with respect to SPECT is that the annihilation occurring between the emitted e^+ and an e^- from the surrounding matter produces a collinear couple of photons with the same energy of 511 keV. Such collinearity permits to evaluate 2γ coincidences instead of single photons and, therefore, to avoid collimators and significantly increase the efficiency of the signal collection (Figure 1.7). Another advantage is the possibility, for the same reason, to use not just 2D but also 3D PET devices, as coincidences only depend on the time interval Δt between the two counts and can be detected even in two different slices; 3D instruments, characterized by the absence of septa between contiguous slices, provide higher efficiency but also more noise and more random coincidences. The image reconstruction is usually obtained by back-projection, but other algorithms such as MLEM can be used, too; like for SPECT, an attenuation correction is required and hybrid PET/CT and PET/NMR imaging systems have been developed. An example of common radioisotope — and probably the most common so far — for PET applications is certainly ^{18}F which, decaying β^+ to stable ^{18}O with $t_{1/2} = 109.77$ min, is widely used in this branch

of nuclear medicine.

Coincidences can be handled using the following formula for the rate R_c of random coincidences between two detectors counting respectively C_1 and C_2 events per second: $R_c = 2\tau C_1 C_2$, where τ indicates the proper time window of the detectors, whose order of magnitude is typically 10 ns. Random coincidences come from two (nearly) simultaneous events that lose a γ each in the patient and are fallacious. Multiple coincidences, i.e. simultaneous events with no γ loss, and scatter coincidences, i.e. when at least one γ is scattered but anyhow reaches a detector, can instead be considered. State-of-the-art technologies use particular scintillating crystals with very fast response in order to measure the time of flight (TOF) of the coincident photons and, knowing their speed is c, estimate directly the position of the annihilation event[5]: this technique, that allows to inject even less activity in the patient, is known as TOF PET.

Eventually, it is important to remark that CT, SPECT and PET devices have been developed not just for clinical use but also for pre-clinical studies on animal — murine — samples. Smaller organ dimensions are involved in these experiments, so the highest resolutions reachable are necessary to visualize well defined results. A wide use of such images will be made in the next chapters. [4] [9] [12]

---

[5]Which is next to the β^+ decay position due to the short range of e^+ in a macroscopic scale.

Chapter 2

The ISOLPHARM project

This work has been commissioned by the ISOLPHARM (ISOL technique for radioPHARMaceuticals) project headed by the Legnaro National Laboratory (LNL) of the Italian National Institute for Nuclear Physics (INFN). ISOLPHARM was born in 2016 with the purpose of exploiting the II generation ISOL facility SPES (Selective Production of Exotic Species) at LNL in order to obtain innovative radionuclides of medical interest with high purity. Being a strongly multidisciplinary collaboration, it requires several kinds of professionists from different fields, such as physicists, engineers, biologists and chemists. Besides INFN, many institutions are taking part to the experiments, like the University of Padova with the Department of Physics and Astronomy "Galileo Galilei", the Department of Chemistry and the Department of Pharmaceutical and Pharmacological Sciences.

The project is subdivided in three main tasks:

- Task 1, carrying on the experiments of nuclear physics and the development of the ISOL targets and extraction technologies;

- Task 2, studying the chemical processes to isolate the radionuclides without losing pureness and synthesize the radiopharmaceuticals;

- Task 3, including the biological testing of the new radiopharmaceuticals *in vitro* and *in vivo*.

Furthermore, up to now, two pilot experiments have been running:

- ISOLPHARM_Ag (2018-2019), with the aim of producing by neutron capture small quantities of ^{111}Ag, which — as we will see — is probably the most innovative radionuclide obtainable by means of the ISOL technique, and preliminarily studying its properties;

- ISOLPHARM-EIRA (2020-2022), meant to begin the in vitro and in vivo sperimentation.

The current chapter will mainly focus on the physical part and on the interesting radionuclides, before finally giving a precise collocation to this thesis work inside the whole project. [1]

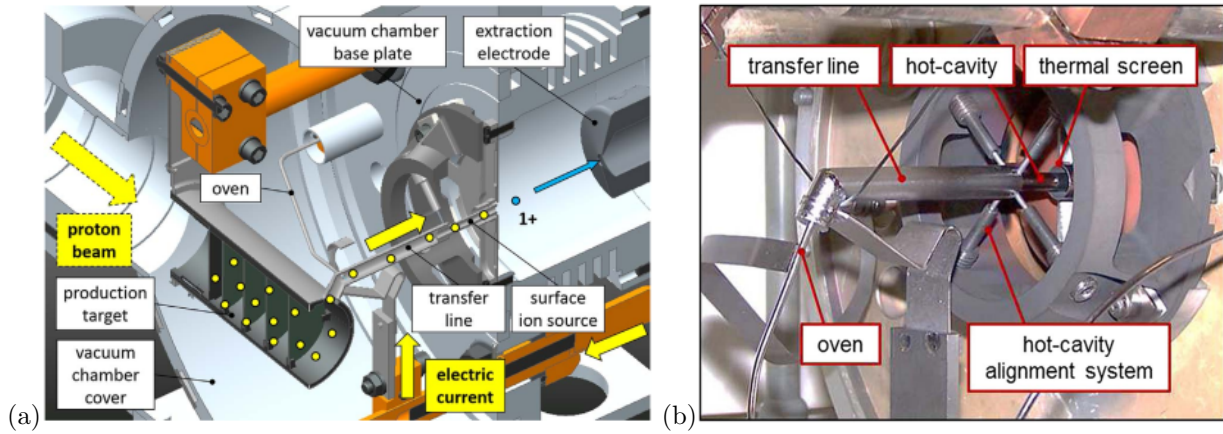Figure 2.1: INFN-LNL and ISOLPHARM official logos. [1]

Figure 2.2: (a) ISOL-SPES explanatory schema. (b) Surface Ionization Source. [13]

2.1 The ISOL technique

As we were saying, the ISOL (Isotope Separation On-Line) method has been chosen in order to produce the radionuclides, since it allows to generate the RIBs (Radioactive Ion Beams) with a high level of selectivity. The strategy consists in hitting a solid target with a proton beam accelerated by a cyclotron; typical values of energy and intensity of this beam are tens of MeV and tens or hundreds of μA. The nuclear reactions happening in the target produce a great variety of exotic nuclei, depending on the target composition and on the proton energy. The most important target for ISOLPHARM is a *fissile* (i.e. admitting nuclear fission reactions) target made up by seven uranium carbide disks, whose diameter and thickness are 40 mm and 0.8 mm. Uranium carbide is a mixture of uranium dicarbide (UC_2), graphite (C) and, in lower concentration, uranium monocarbide (UC); due to its heterogeneity, it is often referred to as UC_x. Figure 2.3 shows which region of Segrè's chart can be populated with UC_x. Examples of non-fissile targets under study are instead titanium carbide (TiC), zirconium germanide (ZrGe) and gadolinium boride (GdB_4).

The obtained nuclides diffuse all over the target and, since the temperature reaches (and is maintained at) 2000°C, the elements which are volatile[1] in these conditions evaporate and effuse through a structure called *transfer line*. Such line leads them to an ionizing high vacuum chamber, kept at a pressure of about $10^{-6} \div 10^{-5}$ mbar. In the chamber the nuclides get ionized to the +1 charge state and become ready to be extracted and accelerated by means of a high voltage that can reach 40 kV, thus generating the RIBs. Actually, not every nuclide arrives to the accelerator: each mentioned stage owns a proper efficiency depending on the atomic species. Hence, one can assign to each element a coefficient ϵ given by the product of the contributions in efficiency for each process. These coefficients are influenced by the geometry of the production target and by the selected ionization source. In the context of SPES-ISOLPHARM, the studied sources are:

- SIS (Surface Ion Source), developed for the elements in the first two groups of the periodic table; it consists of a 34 mm long tubular cavity with a diameter of 4.1 mm, able to achieve temperatures of 2000÷2200°C by means of Joule effect and to ionize elements with ionization potential up to 7 eV once they interact with the surface (a schematic representation of ISOL-SPES and a SIS are shown in Figure 2.2);

- PIS (Plasma Ion Source), for elements characterized by higher electronegativity; classifiable as a FEBIAD (Forced Electron Beam Induced Arc Discharge) source, it is mainly composed by a tantalum cathode, a molybdenum anode and a cylindric discharge chamber, surrounded by a solenoid originating a magnetic field; the cathode, heated by Joule effect until 2200°C, generates a thermionic emission of electrons which are gathered by the anode (the electrodes having a 150 V voltage between each other) and injected in the chamber, forming a plasma that can be accelerated by the magnetic field and sent towards the neutral nuclides passing by in order to

---

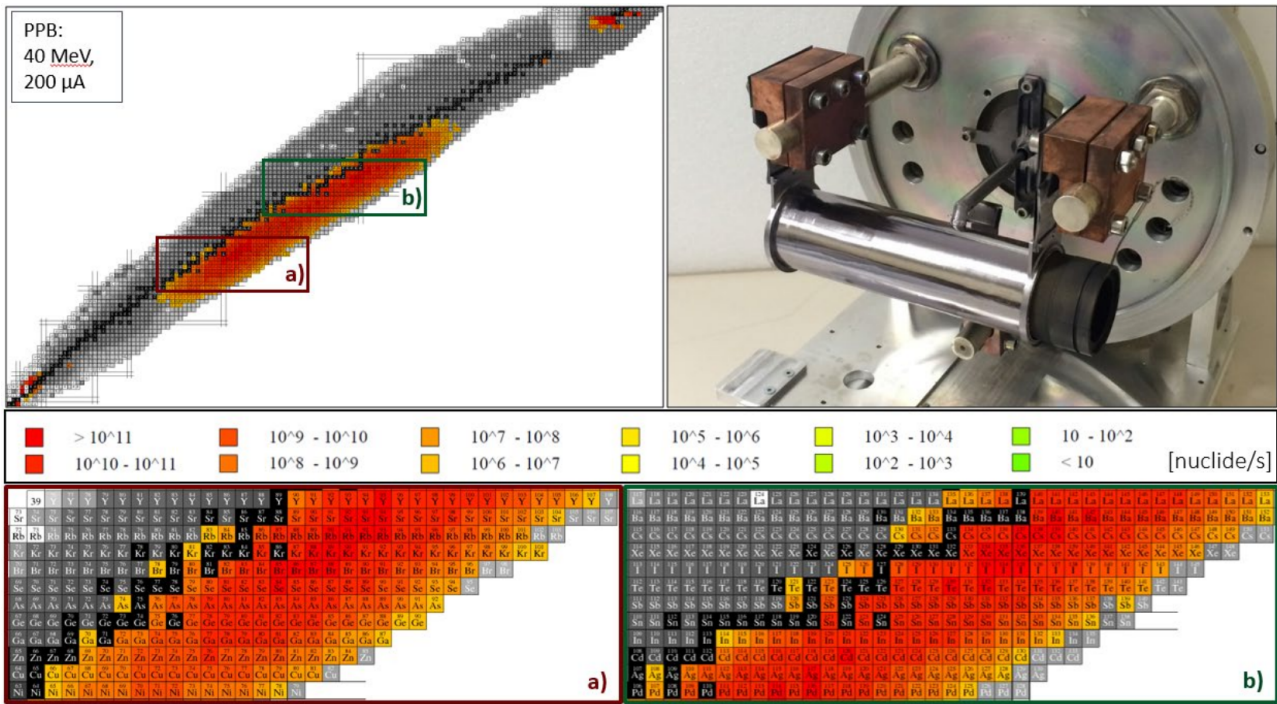[1]Otherwise they are referred to as *refractory*.

Figure 2.3: Regions of the nuclide chart that can be populated starting from a target in UC_x and production efficiency with a proton beam at 40 MeV and 200 μA. [14]

ionize them.

- LIS (Laser Ion Source) is currently under study; atoms can be ionized by an incident laser and, for each radionuclide of interest, the laser wavelength optimizing this process can be investigated.

It is important to underline how reaching a high temperature is fundamental for the correct functioning of the entire apparatus: to achieve this, the choice of the incident beam's features and of the materials composing the production target must maximize the power dissipated by the nuclear reactions. Contextually, a cooling system is required for the ionizing high vacuum chamber and, for certain types of targets, even for the target itself. In order to attain this, a cooling system exploiting the thermal conduction of water and liquid litium is utilized.

In conclusion, the ISOL technique results convenient since it allows to obtain high quantities of different radionuclides and, changing the composition of the target, to focus the production in several regions of the nuclide chart, opening the possibility to study even unconventional radioisotopes, which may be difficult and/or too expensive to be produced using ordinary accelerators or nuclear reactors. [13] [14]

2.2   The ISOLPHARM chain

After the ISOL stage we have just described, once the chosen radionuclides are ionized with a certain efficiency, it is possible to accelerate them by means of an electric field, sending a RIB towards a mass selector. Here, the nuclei are distinguished depending on their mass number, which affects their deflection angle and thus their flight trajectory. The resulting isobaric RIB, containing just the nuclide of interest and its isobars, is finally deposited into a collection target. This selection stage is expected to be highly reliable, with $\epsilon \sim 100\%$. A part of the isobars can decay towards the interesting one, e.g. when handling chains of β-emitters moving diagonally along the nuclide chart, but anyway a chemical treatment is needed in order to attain a satisfactory purification. Subsequently, the pure radionuclide is bound to a carrier molecule, obtaining the radiolabelled drug. Such molecule can be divided in three components (Figure 2.4):

- the *chelator*, that stably binds the radionuclide with coordination covalent bonds;
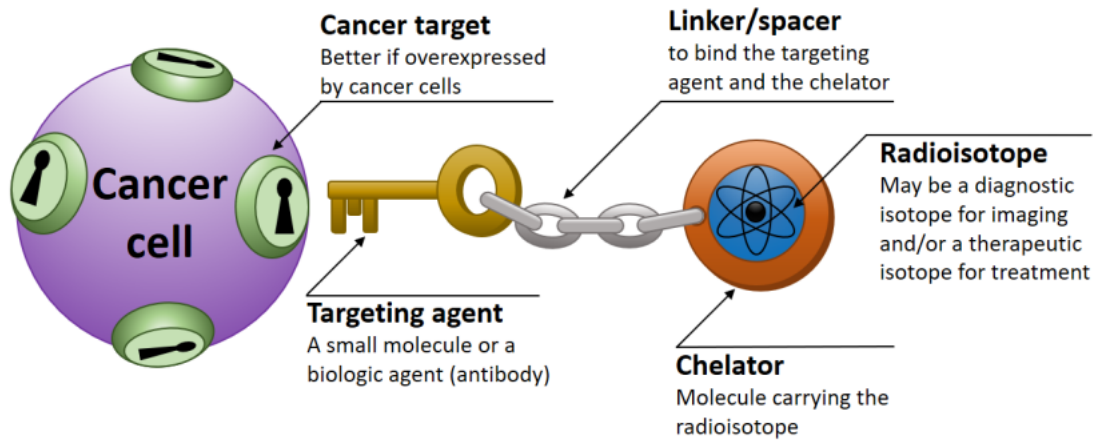
Figure 2.4: Targeting mechanism and structural subdivision of a radiopharmaceutical carrier molecule. [14]
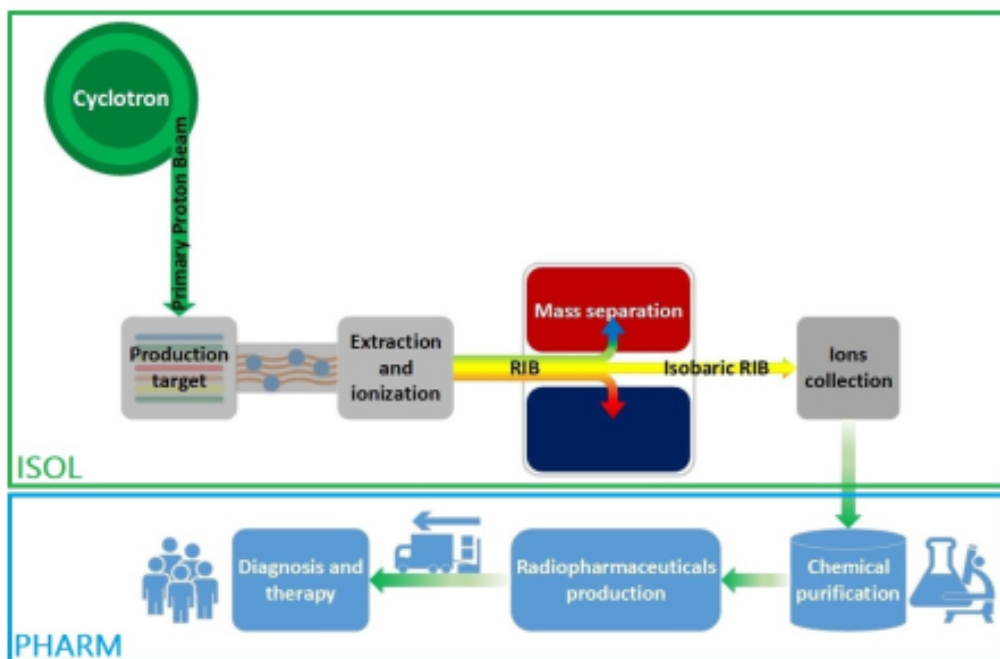

Figure 2.5: Representation of the complete ISOLPHARM radiopharmaceutical production chain. [14]

- the *targeting agent*, whose function is to take the radionuclide to (or into) the cancer cells interacting with specific receptors overexpressed in their plasma membrane;

- the *linker*, or *spacer*, which connects the previous two and avoids interactions between them.

Before being commercialized, such radiopharmaceuticals have to undergo a series of *in vitro* and *in vivo* experiments in order to test if they distribute correctly in the ill sites, if they irradiate those tissues with an appropriate dose and how much they damage healthy organs. An exhaustive schema which summarizes all the explained processes is visible in Figure 2.5. [14]

2.2.1 Innovative radiolabelling

Let us now have a short look at the main candidate radionuclides that could be produced by the ISOLPHARM project (Figure 2.6), highlighting the features that make them eligible for a medical use. The most important nuclide studied up to now is ^{111}Ag. Such silver isotope has never been used in medical physics because of the difficulties and the costs to face in its production, whereas the ISOL technique with the use of the UC_x target would solve these issues; however, it decays β^- with a mean energy of $E_\beta = 360.4$ keV — suitable for cancer therapy — and with a half-life of $t_{1/2} = 7.45$ d — not
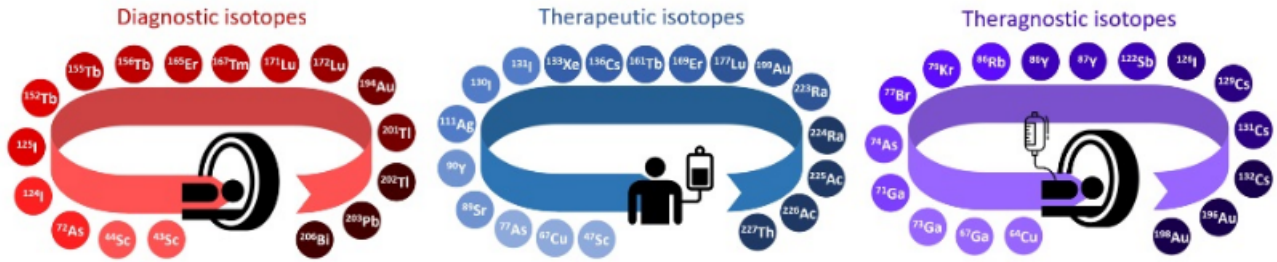
Figure 2.6: Main radioisotopes of actual or possible medical interest producible with the ISOL technique. [14]

too short to be transported to the hospitals and not too long-living in the patient's body —. Moreover, as we will see later, the de-excitation of its daughter nucleus ^{111}Cd emits a γ radiation which could make a drug radiolabelled with ^{111}Ag traceable, hence perhaps leading to a fully theranostic effect. Regarding its isobars, ^{111}Ag belongs to a chain of β^- unstable nuclei which start from the neutron drip line and, with increasing half-lives, approach the valley of stability of the Segrè chart until the stable isotope ^{111}Cd. Due to the decays and the chemical properties of the elements involved, the collection target will just receive ^{111}Cd, ^{111}Ag and a small contribution of its mother nucleus ^{111}Pd, decaying with $t_{1/2} = 23.4$ min and presenting a metastable state, ^{111m}Pd, with $t_{1/2} = 5.5$ h. Analytic calculation of the activity attainable in the collection target can be performed by solving Bateman's differential equations [15] [16].

The ISOL technique combined with an UC$_x$ target can produce pure β^--emitters as well, suitable for therapy, such as ^{89}Sr and ^{90}Y; these isotopes are characterized by an intense β^- emission (the latter has $E_\beta = 932.4$ keV) and a negligible γ radiation once decayed. Other important obtainable radionuclides are ^{131}I, ^{136}Cs and ^{153}Sm, that show a lower β^- energy with respect to the pure β^--emitters but an appreciable γ radiation which might be used for SPECT diagnosis. Among these radioisotopes, together with ^{111}Ag, ^{136}Cs assumes as well a special relevance for the ISOLPHARM collaboration since its medical use is still in the early stages and the high volatility of cesium ensures that great quantities of it could successfully be extracted from the production target. [12] [13] [14] [15]

2.3 Purposes

In this context, the aim of such a work is to establish a connection between the physical and the biological tasks of the ISOLPHARM project, starting a new series of studies of the same kind. Instruments and notions taken from nuclear, medical and biological physics will be exploited in order to build a computational predictive model for the dose absorbed by the biological tissues of a murine sample during a TRT using innovative radiopharmaceuticals.

More specifically, two powerful tools will characterize this work in the following chapters:

- Monte Carlo simulations, provided by the Geant4 software [2], developed at CERN and widespread among research in physics of the fundamental interactions, which will be used to simulate the effects of radiation for a high number of decay events;

- medical PET/CT and SPECT/CT combined imaging, which will give information about the activity distribution and the morphology of the murine body.

This computational dosimetry study will be carried out in the next chapters with two different approaches. The first one, in Chapter 3, will use Monte Carlo simulations to examine the effectiveness of either monoenergetic or radioisotopic radiation in small biological volumes and then this information will be added to the PET or SPECT imaging in order to estimate the absorbed dose maps; we will see how this is possible computationally by following a convolution procedure. The second method, instead, consists in a direct Monte Carlo based dosimetry, which runs the simulations directly in a computer reproduction of the mouse's body — the so-called *phantom* — built from the CT and uses, again, the functional PET or SPECT imaging for the decay events; this strategy, together with an

Figure 2.7: Geant4 official logo. [2]

analytic model for the biodistribution of the activity provided by means of biophysical arguments, will be exposed later in Chapter 4.

Part II

Computed dosimetry

Chapter 3

Dosimetry with MIRD schema

As well-known, the Monte Carlo principle consists in simulating a high number of stochastic events in order to extract the behavior of a physical system. The first method we are going to use for dose calculation exploits Monte Carlo simulations to study the behavior of a radiation source in a material in terms of deposited energy at a certain distance. The technique is then based on a computational procedure of convolution and on medical physics imaging, in particular emission tomography tools which can provide information about an activity distribution. The first section of this chapter will expose in detail the adopted schema and, once all the main aspects will be clarified, it will explain how they will participate to the current research.

3.1 The MIRD formalism

This method was proposed by the Committee on Medical Internal Radiation Dose (MIRD) of the American Society of Nuclear Medicine & Molecular Imaging (SNMMI) and, for this reason, it is known as MIRD schema [17]; its strategy includes four main steps.

1. The creation of a virtual volume made of a given material or tissue, subdivided in elementary units such as concentric shells or voxels (in Geant4, they can be classified as sensitive volumes in order to count the deposited energy).

2. The collocation of a radiation source inside the volume, paying attention to its symmetries.

3. The Monte Carlo simulation of a high number of time-independent radiation events, followed by the calculation of the mean absorbed dose per event in every shell (*Dose Point Kernel*, DPK) or voxel (*Voxel S-Value*, VSV).

4. The convolution between the obtained kernel and a function expressing the activity distribution in the sample, namely a PET or SPECT 3D image.

Let us now focus for a while on the meaning of such a convolution operation, considering the voxel case. First of all, it is important to understand that, from a physical point of view, VSVs and DPKs represent a tensor kernel, whose coefficients are connected to the effectiveness of a source emitting from its center. Our sample will correspond to a voxelized volume with the dimensions and resolution of the image; the kernel used must have the same voxel size. Following the time-independent MIRD
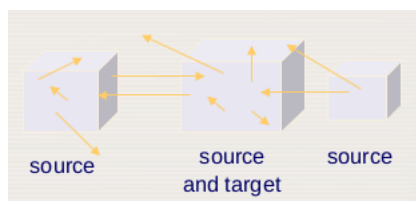

Figure 3.1: Basic concept of the MIRD schema; of course every target voxel may be itself a source voxel. [4]
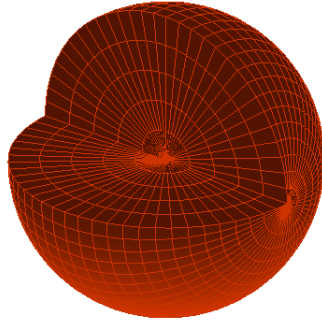
Figure 3.2: Spherical volume with 5 concentric shells of water created with Geant4 (radial planes have been drawn just to ease the 3D view and do not represent any border between surfaces); a quarter is missing in order to visualize the shells.

formulation under the assumption that the masses involved do not change during the irradiation, we can define the dose rate in a voxel r_t of the sample at the image acquisition time t as (Figure 3.1)

$$\dot{D}(r_t, t) = \sum_s A(r_s, t) \, S(r_t \leftarrow r_s) \tag{3.1}$$

where $S(r_t \leftarrow r_s)$ is the S-value in r_t given by the kernel centered in the voxel r_s and $A(r_s, t)$ indicates the activity in r_s provided by the image.[1] A more rigorous definition of the S-value in r_t for a radioactive source placed in r_s can be given as follows: calling m_t the mass of r_t, E_i the mean energy of the ith decay mode, Y_i its branching ratio and $\phi(r_t \leftarrow r_s, E_i)$ the average fraction of E_i deposited in r_t, one has

$$S(r_t \leftarrow r_s) = \frac{1}{m_t} \sum_i E_i \, Y_i \, \phi(r_t \leftarrow r_s, E_i) \tag{3.2}$$

Repeating for the whole sample, or for a single organ, the final result is a 3D dose rate map; the implementation of more kernels referring to different tissues (e.g. with the help of a CT) leads to more precise estimations. If a series of subsequent PET or SPECT images is available, one can reconstruct the activity curve and integrate over a period T, obtaining the time-integrated activity

$$\tilde{A}(r_s, T) = \int_0^T A(r_s, t) \, dt \tag{3.3}$$

and finally the total absorbed dose after T

$$D(r_t, T) = \sum_s \tilde{A}(r_s, T) \, S(r_t \leftarrow r_s) \tag{3.4}$$

Of course the integration over T could also be applied to the dose rate $\dot{D}$, but this would require to apply a convolution for each image instead of only once.

The purpose of this chapter is then to provide a database, validated by the comparison with the pre-existing literature, containing the DPKs and the VSVs of the ISOLPHARM radionuclides of interest for several tissues and voxel sizes. Finally, an example of VSV convolution using a murine sample will be proposed. DPK convolution is possible as well by means of additional calculation, but this will not be done in this context even if the coefficients will be inserted in the database.

3.2 Dose Point Kernels (DPK)

Let us begin this study with the DPKs. On Geant4 one can build a spherical volume subdivided in concentric shells, as in Figure 3.2(a), and fill it with a selected material. The first simulations will run with monoenergetic and isotropic e$^-$ sources in order to become familiar with the model and see if

---

[1]The indices s and t stand for *source* and *target*.

Particles	Cut-off range [mm]
γ, n	1
e	0.1
p, π, μ	0.05
α, ^{3}He	0.01
Ions	0.001

Table 3.1: Typical cut-off ranges in the Electromagnetic Standard Option 3 library; 1 mm is the default value in Geant4. [2]
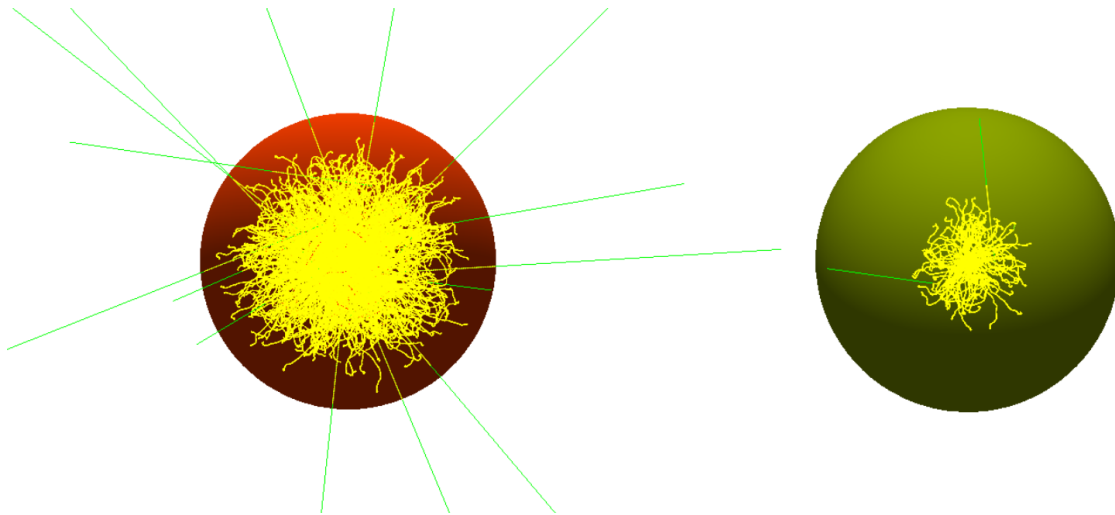

Figure 3.3: Monoenergetic electron source at 500 keV in water, on the left, and compact bone, on the right; yellow and green trajectories represent electrons and photons respectively.

it is reliable and in accordance with the references; then, a method to assess the uncertainty of such Monte Carlo simulations will be proposed. Subsequently, radioactive sources will be inserted and the effectiveness of some of the main ISOLPHARM radionuclides will be studied. Due to the spherical symmetry of the volumes, the sources will always be placed in their center.

For DPKs, two materials were used: water and compact bone. Water is often utilized in this field as a good approximation for most of the human soft tissues because of its hydrogen and oxygen composition and its density $\rho_w = 1$ g/cm^3; moreover, many studies of microdosimetry in literature, concerning either simulations or experiments, make use of water in this context. All the materials simulated in this research activity, here and in the following chapter, are available on the Geant4 material database but can be also generated manually by the user.

Regarding particle interactions and nuclear reactions in Geant4, the chosen library was the physics list *Electromagnetic Standard Option 3*, developed especially for applications of nuclear physics requiring high precision on low energy processes involving electrons, hadrons and ions. An interesting parameter is the *cut-off* range: in order to lighten the computational mole, particles get killed (i.e. they cease to be traced in the Monte Carlo) when their energy falls below a certain threshold, which is related to a penetration range in the material they are going through; otherwise, if this does not happen, a particle is normally killed when it gets out of the simulation world, i.e. an air box containing the sphere. Table 3.1 shows the cut-off ranges of the cited physics list for the main particles involved in our simulations. To enable decays the list *Radioactive Decay Physics* was added.

3.2.1 Monoenergetic electron sources

For this first part, e$^-$ sources with energy E_0 of 10, 50, 100 and 500 keV were considered and the reference study was Botta et al., 2011 [18], where a different Monte Carlo code, FLUKA [19], was used. Figure 3.3 illustrates two equal spheres made of water and compact bone with a monochromatic source of e$^-$ at 500 keV located in their centers. We can immediately notice a different degree of penetration

E_0 [keV]	dr [μm]	$\rho R_{csda}|_w$ [g/cm^2]	$\rho R_{csda}|_{cb}$ [g/cm^2]
500	20	$1.766 \cdot 10^{-1}$	$1.898 \cdot 10^{-1}$
100	2	$1.431 \cdot 10^{-2}$	$1.545 \cdot 10^{-2}$
50	0.6	$4.320 \cdot 10^{-3}$	$4.681 \cdot 10^{-3}$
10	0.04	$2.515 \cdot 10^{-4}$	$2.761 \cdot 10^{-4}$

Table 3.2: Shell thickness and e$^-$ range in water and compact bone [21] used at the various energies.
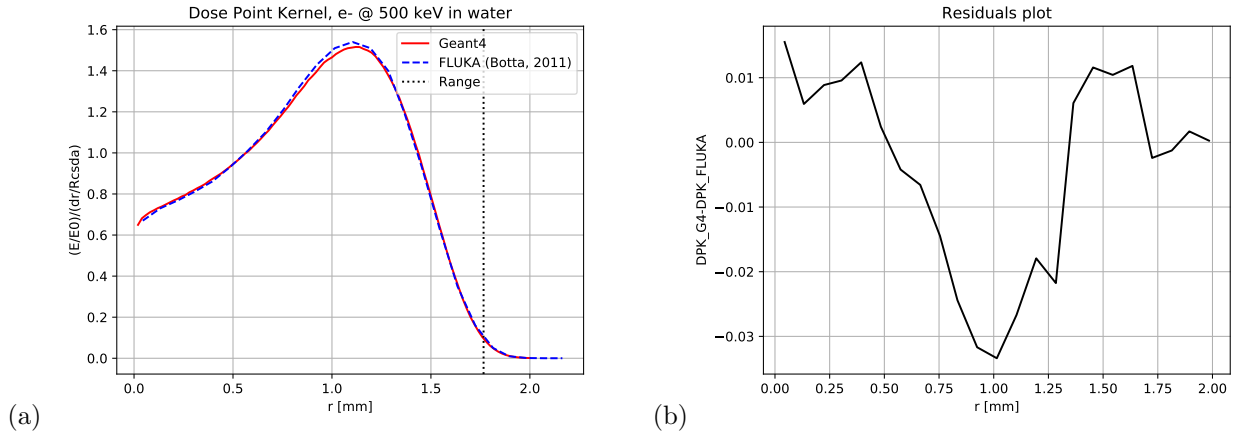
Figure 3.4: (a) DPK curves of 500 keV e$^-$ in water using Geant4 with 10^6 events, compared with Botta et al., 2011 using FLUKA. (b) Residuals plot.

due to the higher density of compact bone, namely $\rho_{cb} = 1.85$ g/cm^3; moreover, intuitively, a radiation with lower energy results less penetrating: for this reason, in order to obtain precise curves, 100 shells with equal thickness dr were always created, as in literature, with dr decreasing for lower energies. The radius of the sphere, clearly obtainable multiplying dr by 100, was always long enough to contain at least all the non-γ trajectories.

The results of the first simulation, with e$^-$ at 500 keV in water and compact bone, are shown in Figures 3.4 and 3.5 (all the graphs were produced by means of the Python3 software [20]). The curves obtained with Geant4 are compared to the ones obtained by FLUKA in Botta et al., 2011; in order to facilitate this comparison, the same units were used. Defining the radiation range R_{csda} as the particle path in the material before losing all its energy in the *Continuous Slowing Down Approximation*, where the energy loss is considered equal to the stopping power of the material:
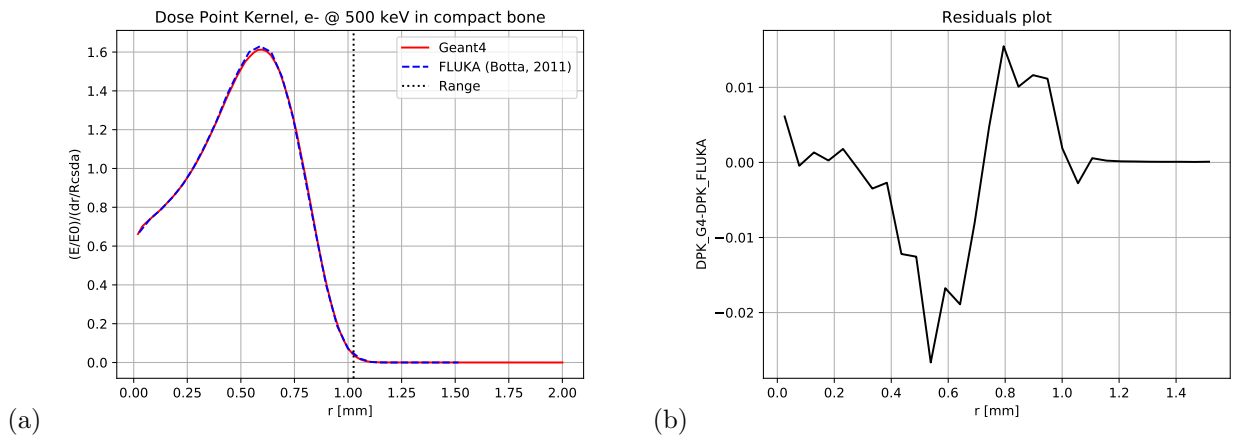
Figure 3.5: (a) DPK curves of 500 keV e$^-$ in compact bone using Geant4 with 10^6 events, compared with Botta et al., 2011 using FLUKA. (b) Residuals plot.

(a)

(b)

(c)
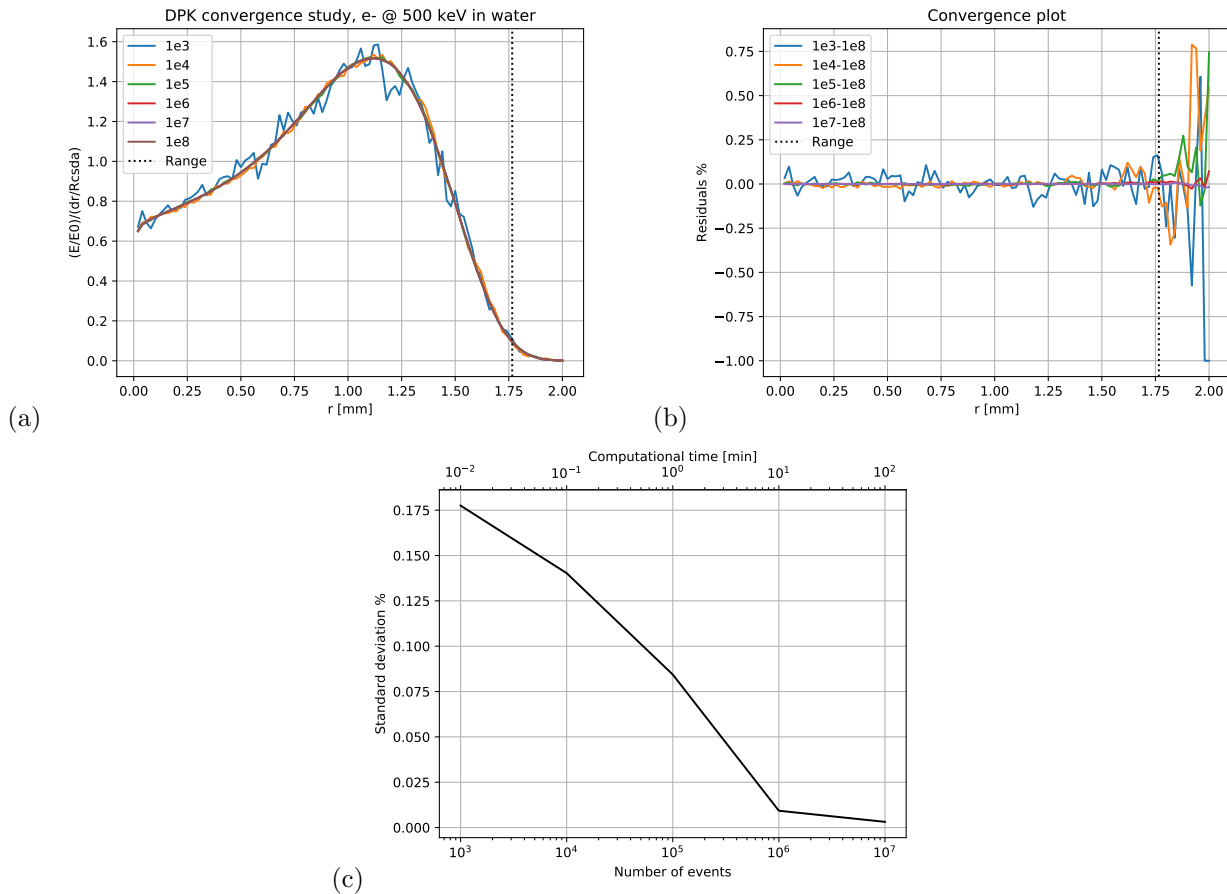
Figure 3.6: Convergence study for DPKs with e$^-$ at 500 keV in water.

- in the abscissa the external radius of each shell r is expressed in mm;

- in the ordinate we find a dose-like quantity defined as the ratio E/E_0, being E the energy deposited in the shell and E_0 the initial energy, divided by dr/R_{csda}.

The R_{csda} values, shown in Table 3.2 together with dr, were taken from the NIST *estar* database [21]. Anyway, the DPKs in our database are simply expressed in keV/g per event. At $E_0 = 500$ keV we notice a substantial agreement with the reference study, as visible also in the residuals plots. Like we expected, the compact bone curve appears sharper than the water one, since they both go to zero near their own ranges; the spherical shells used in the simulations were exactly the same, hence we can see that, contrary to water, compact bone absorbs almost all the radiation within half the total radius.

A thing that could already be done with this first results is finding a method to estimate the uncertainty of this calculation and, especially, to have an idea of how many events we need to simulate for reliable results. With this purpose, let us now have a look at the convergence study in Figure 3.6; graph (a) compares six simulations of 500 keV electrons in water with the number of events growing from 10^3 to 10^8. One can immediately distinguish the poor quality of simulations with a small number of events and the nearly total absence of noise in the 10^8 case. Thus, we can assume the latter as our model and calculate the percentage residuals of the other simulations with respect to it, in graph (b); the final step is then to compute the percentage standard deviation of each simulation with less than 10^8 events, as in graph (c). In our case, we may be interested in having fluctuations below 1% until R_{csda} is reached; looking at these plots, we find out that such a precision with respect to the highest statistics of 10^8 events is achieved by at least 10^6 events. A simulation of this kind takes about 10 min with CPU Intel i5-9600 (6) @ 4.6 GHz, which is of course an acceptable time (the upper abscissa in the last graph shows a rough estimate of the computational time based on this measured value); for this reason, all the other simulations in the current section will be characterized by 10^6 events. Since radioactive sources have complex radiation spectra and are consequently more time-expensive
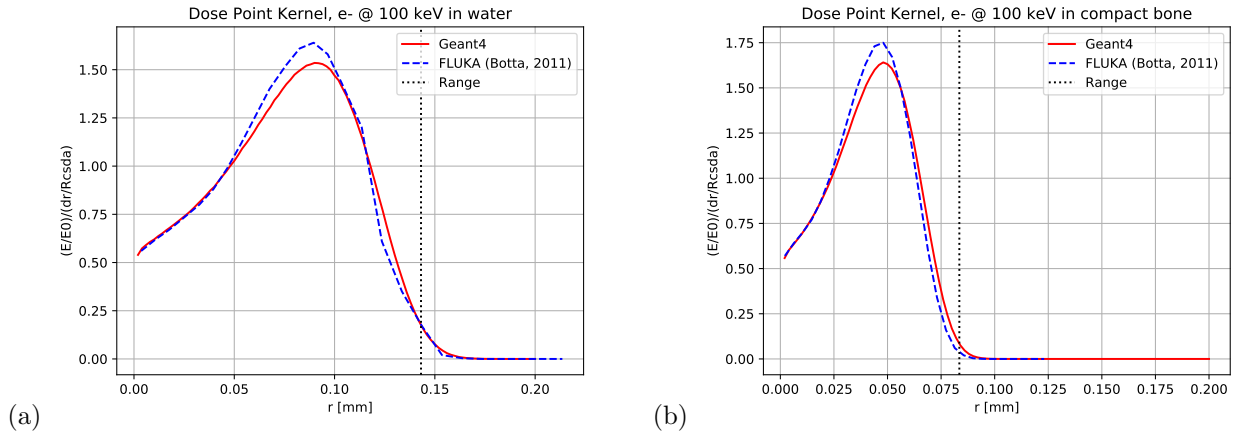
Figure 3.7: DPK curves of 100 keV e$^-$ in (a) water and (b) compact bone using Geant4 with 10^6 events, compared with Botta et al., 2011 using FLUKA.
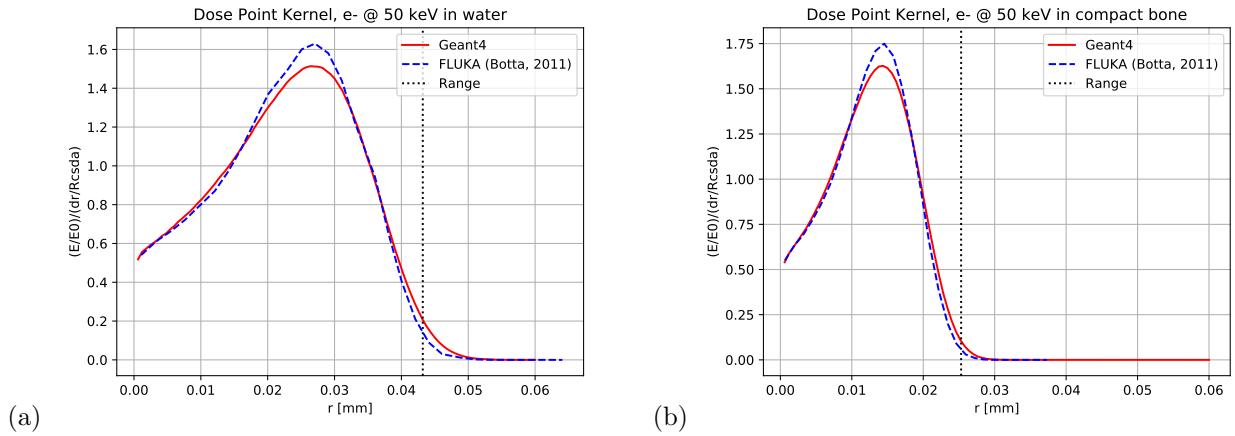

Figure 3.8: DPK curves of 50 keV e$^-$ in (a) water and (b) compact bone using Geant4 with 10^6 events, compared with Botta et al., 2011 using FLUKA.
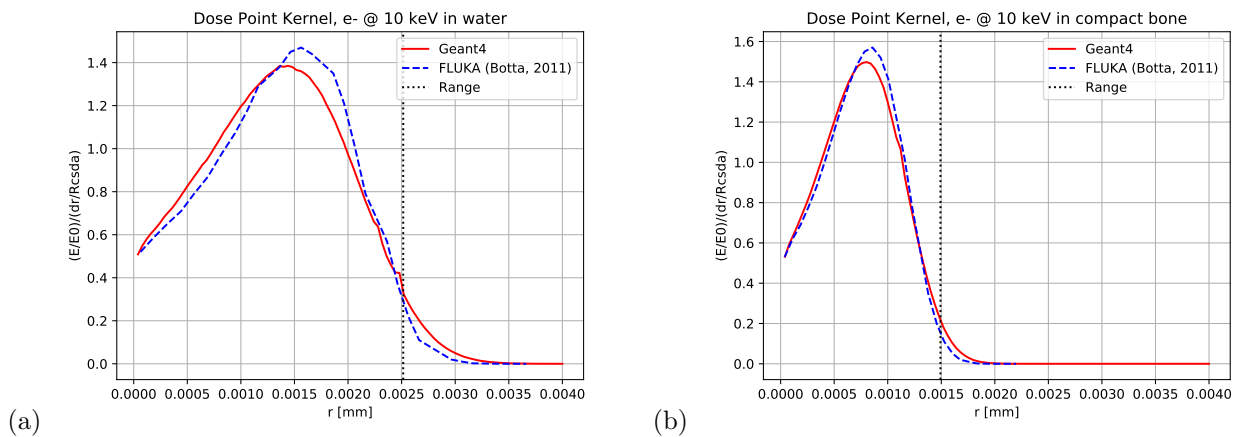

Figure 3.9: DPK curves of 10 keV e$^-$ in (a) water and (b) compact bone using Geant4 with 10^6 events, compared with Botta et al., 2011 using FLUKA.
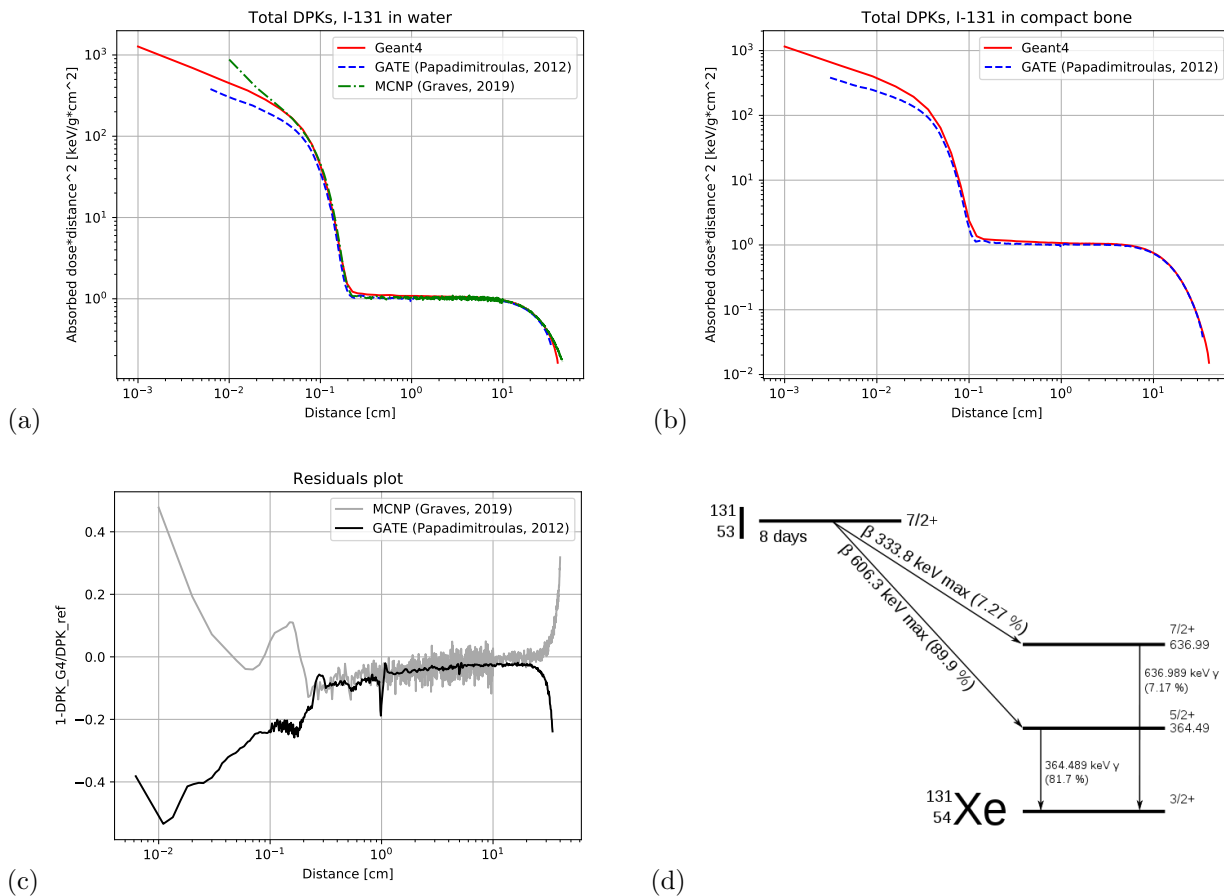
Figure 3.10: DPK curves of ^{131}I in (a) water and (b) compact bone using Geant4 with 10^7 events, compared with Papadimitroulas et al., 2011 using GATE and Graves et al., 2019 using MCNP. (c) Residuals plot for water. (d) ^{131}I decay scheme [27].

to a computer, these considerations will be applied again in the following sections.

The first examined E_0 gave a quite good result if compared with literature; however, if we consider Figures 3.7, 3.8 and 3.9, the agreement worsens for lower values of E_0. This could be due to some differences in the two Monte Carlo algorithms, such as different cut-off settings or other parameters. Also, the version of FLUKA used is at least 10 years old and more recent updates may have added some improvements. Anyway, what matters is that the energy deposition pattern is basically the same and we can proceed with the next simulations.

3.2.2   Radioactive sources

After observing the results of the monochromatic e$^-$ DPKs, we are ready to study radioisotopic sources. An important difference from the previous case is that γ radiation assumes more relevance now, since we are analyzing heterogeneous nuclear emissions. This is why the Geant4 sphere needs to be enlarged: 200 shells were set with progressively growing thickness for a total radius of 402 mm. Increasing thickness was chosen as a compromise between the small volumes required to have a precise assessment of β radiation and the computational trouble deriving from a too high number of sensitive shells. With $dr_0 = 0.02$ mm the thickness of the first shell (i.e. the radius of the central core), the ith shell was $i \cdot dr_0$ thick. Dealing with the reference literature, the studies consulted for this DPK calculation were Papadimitroulas et al., 2012 [22] and Graves et al., 2019 [23], who used respectively the Monte Carlo codes GATE [24], which is actually an user-friendly interface of Geant4, and MCNP [25]; such works employed different shell thicknesses as well. Another pertinent and extremely recent paper belongs to Mendes et al., 2021 [26].

Let us begin with the case of ^{131}I, since it is the most studied in literature among the radionuclides of our interest. We are talking about a β^--emitter from whose decay we anyway expect a consistent γ

(a)

(b)

(c)
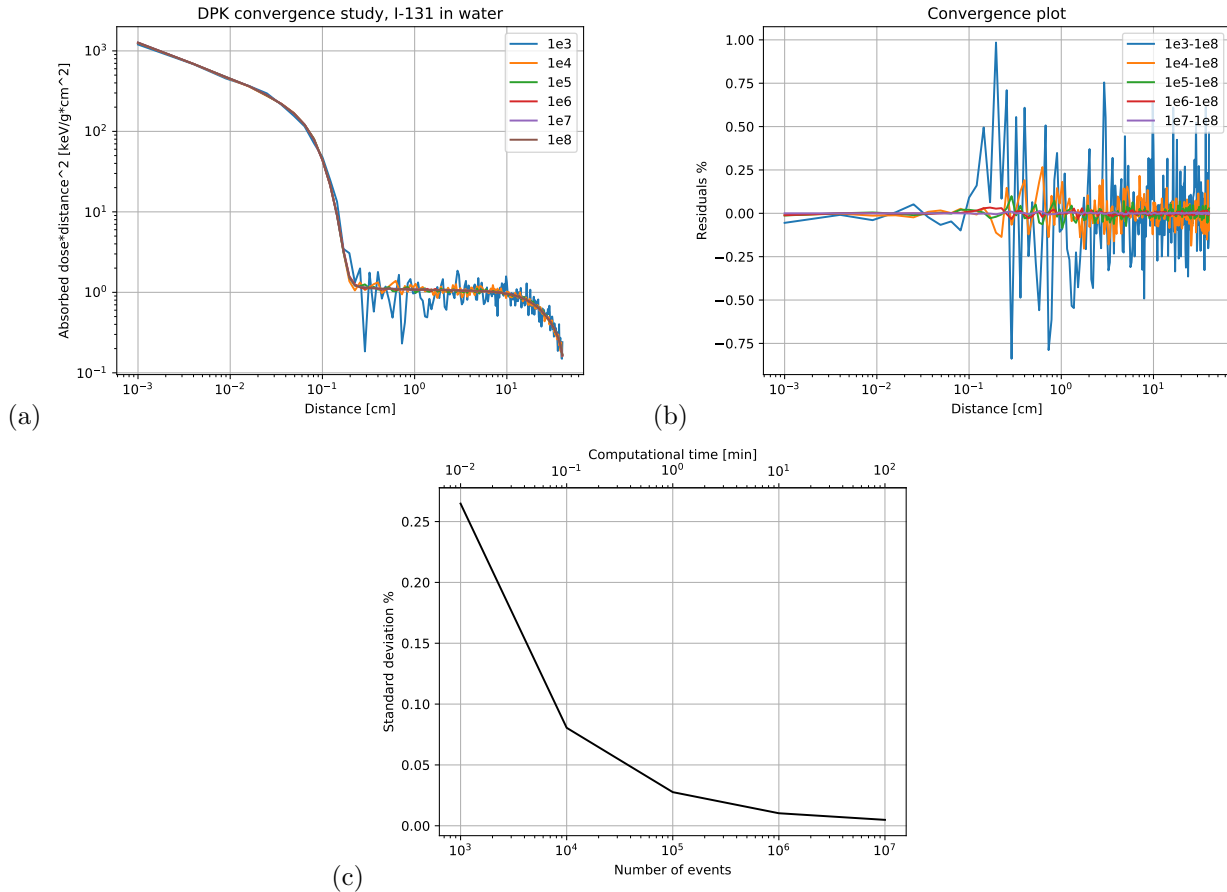
Figure 3.11: Convergence study for DPKs of ^{131}I in water.

radiation due to the de-excitation of its daughter ^{131}Xe. From Figure 3.10, we immediately recognize two shoulders corresponding to the low-range β^- and high-range γ emissions. This time the ordinate plots the absorbed dose (expressed in keV/g) multiplied by the squared distance r^2. Such a visualization mode, common in literature, highlights the fact that for photons there is a *plateau* as long as the deposited energy per shell goes like $dE \propto dr$, since in these conditions $dE/dm \propto dr/(r^2 dr) = r^{-2}$. From Figure 3.10(b) we deduce that, such as in the monoenergetic e$^-$ case, the shape of the curve does not depend on the material crossed: compact bone shows just a faster absorption of the β^- contribution than water. Dealing with literature, we notice a very good agreement in the whole γ shoulder and in the β^- one after 1 mm, while the part below 1 mm reveals different interpretations even from the two references themselves; the residuals plot for water in Figure 3.10(c) shows that Geant4 has a wide percentage difference in lack or excess from the references at the shortest distances, while the discrepancy at long distance is due to zero approaching. Since this issue appear to be proper of the physics libraries used by the Monte Carlo codes, a substitution of the adopted one with the list *Electromagnetic Livermore Physics* was tried, but no significant improvements were registered. On the other hand, the differences occurring from 2 mm on seem really small.

10^7 decay events were simulated, and this decision was again supported by a convergence study; the three steps are illustrated in Figure 3.11, where we can see a different trend with respect to the previous situation. Looking again for an uncertainty under 1% with respect to 10^8 events, the choice fell on 10^7 for all the simulations of this type; 10^6 was no more enough to guarantee that, due to the longer radius covered by these simulations. The CPU time became ~ 100 min (depending on the nuclide) with our devices, but it was anyway acceptable since such kernels have to be calculated just once.

Now we are focusing on a powerful instrument characterizing codes like Geant4 and MCNP: the possibility to program manually the particle killing. One can kill all the produced particles of a certain species, for example all photons, in order to compute exclusively the other contributions. Obviously, removing a particle species speeds up the simulations: this is why neutrinos, typically produced in β
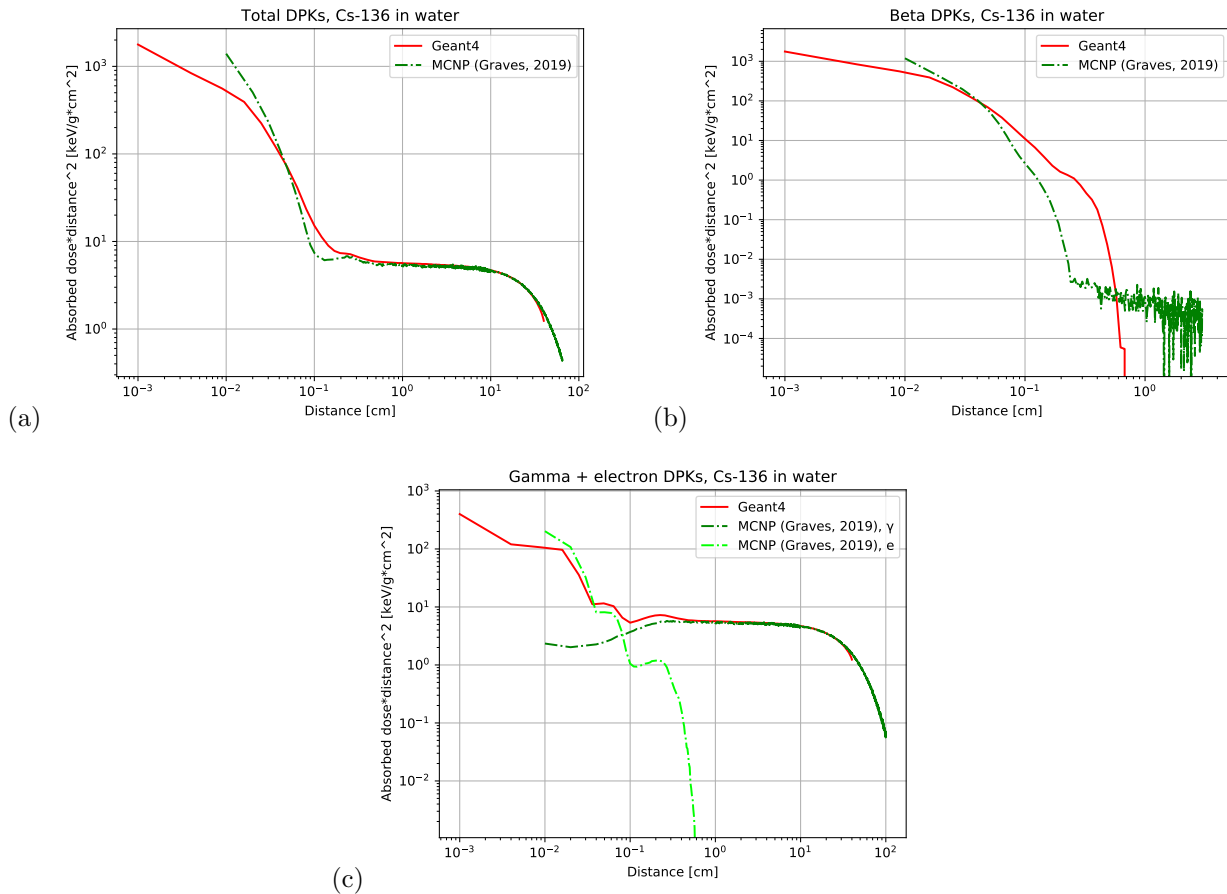
Figure 3.12: (a) DPK total curve of ^{136}Cs in water using Geant4 with 10^7 events, compared with Graves et al., 2019 using MCNP. (b) β curve. (c) γ plus Auger and internal conversion curve.

decays but not interacting with matter, can be neglected and killed.

To provide an example of this, let us switch radionuclide to ^{136}Cs: producible by ISOLPHARM in high quantities, low energy β^- emitter (mainly $E_\beta < 100$ keV), it however emits a considerable γ radiation, with the brighter ray appearing in almost all decays with energy $E_\gamma = 818.514$ keV [12]. In Figure 3.12(a) we can see the comparison of the total curve with Graves et al., 2019: again, the reference is higher at shorter distances, but this time there is also a difference where the two components meet. As visible in Figure 3.12(b), where only the β^- rays are considered, there is a noticeable disagreement between the Monte Carlo codes when simulating this particular radiation. Moving instead to Figure 3.12(c), we realize that γ rays alone are not enough to reproduce the radiation if the β^- electrons are missing, but one can not neglect the effectiveness of other e$^-$ coming from Auger emission or internal conversion (the curve colored in lime). Anyhow, for β^--emitters this contribution usually hides under the β^- dose. In conclusion, the observable discrepancies derive from a different interpretation of the β^- component, while other e$^-$ and γ find a good agreement.

We might now dwell on the behavior of our most representative radionuclide, ^{111}Ag, whose properties have already been discussed. Figure 3.13 illustrates its DPK total curve simulated with Geant4 together with its two components β and γ (actually γ plus Auger and internal conversion). Since this isotope has not been used in nuclear medicine yet, its literature is poor: we only found a γ curve in Graves et al., 2019, which in Figure 3.13(b) is compared to our γ and non-β electrons.

Another interesting radionuclide is an isobar of the previous one, namely ^{111}In, whose γ radiation was already described when talking about SPECT imaging. However, it appeared as well in Table 1.3 as an Auger e$^-$ emitter used in TRT, and in fact in Figure 3.14(a) both Geant4 and Papadimitroulas et al., 2012 show an irregular left shoulder which may describe this Auger radiation; looking also at Figure 3.14(b), which represents the same situation but in compact bone instead of water, three main humps are visible before the γ shoulder, meaning that at least three different e$^-$ ranges are contributing.
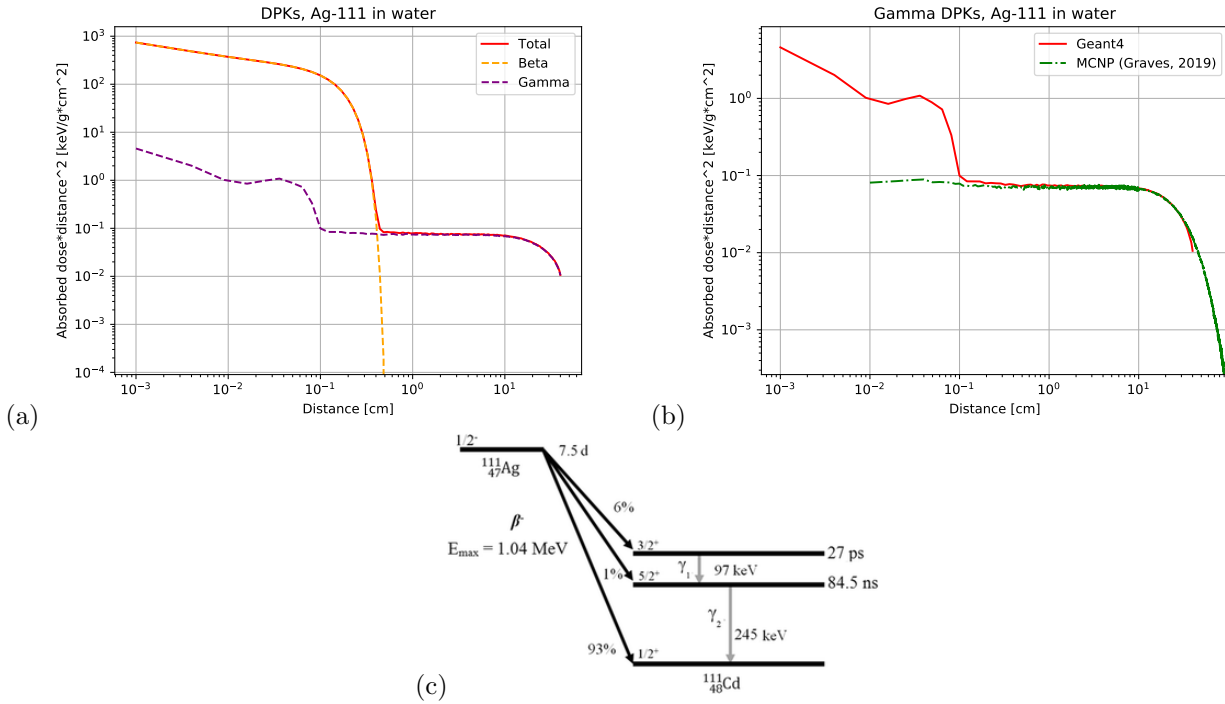
(a)   (b)

(c)

Figure 3.13: (a) DPK total curve of ^{111}Ag in water using Geant4 with 10^7 events. (b) γ plus Auger and internal conversion curve compared with γ curve from Graves et al., 2019 using MCNP. (c) ^{111}Ag decay scheme [28].

Finally, Figure 3.15 reports the results for ^{90}Y, a pure β^--emitter whose average E_β exceeds 900 keV. γ emissions are very rare for this radionuclide and in fact its γ shoulder presents values about one order of magnitude smaller than ^{111}Ag, two orders smaller than ^{131}I and ^{111}In and three orders smaller than the best γ-emitter we have seen so far, i.e. ^{136}Cs. The agreement with Papadimitroulas et al., 2012 looks good especially in water (Figure 3.15(a)) and is probably the best up to now.

We conclude illustrating other radioactive sources of medical interest — here placed in water but available in compact bone as well in the DPK dataset — having an equivalent study in Papadimitroulas et al., 2012; these nuclides, represented in Figures 3.16 and 3.17, are ^{68}Ga, ^{99m}Tc, ^{153}Sm and ^{177}Lu. The Geant4 curves, mostly in the γ part, match quite well with the reference except for ^{99m}Tc (Figure 3.16(b)), where a possible explanation is that GATE may have had some trouble simulating a metastable state: the β^- shoulder, belonging to the g.s., seems indeed correct, but the γ side is way too low for a common and widely used γ-emitter like this. Other DPK curves obtained from radionuclides of medical interest — ^{18}F, ^{64}Cu and ^{89}Sr — are reported in Appendix A.

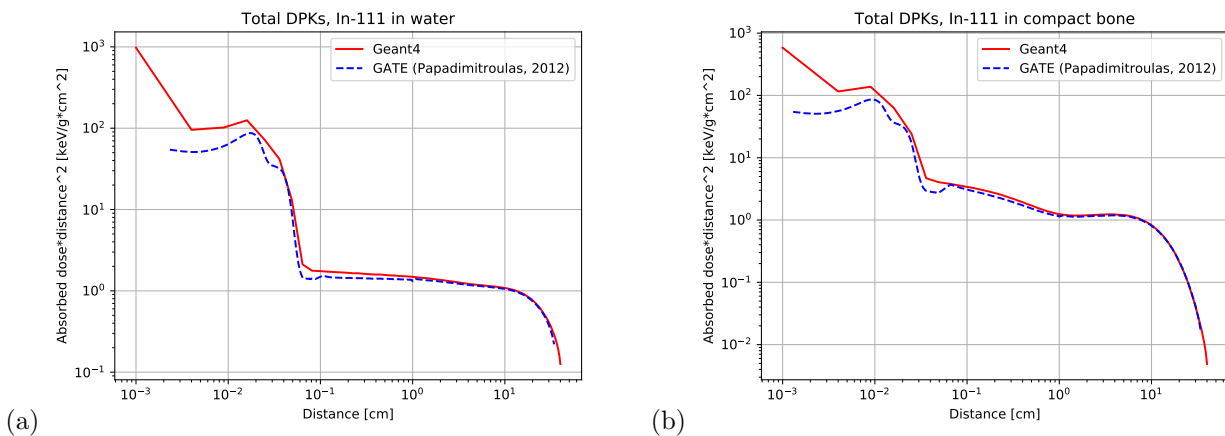(a)   (b)

Figure 3.14: DPK total curve of ^{111}In in (a) water and (b) compact bone using Geant4 with 10^7 events, compared with Papadimitroulas et al., 2012 using GATE.
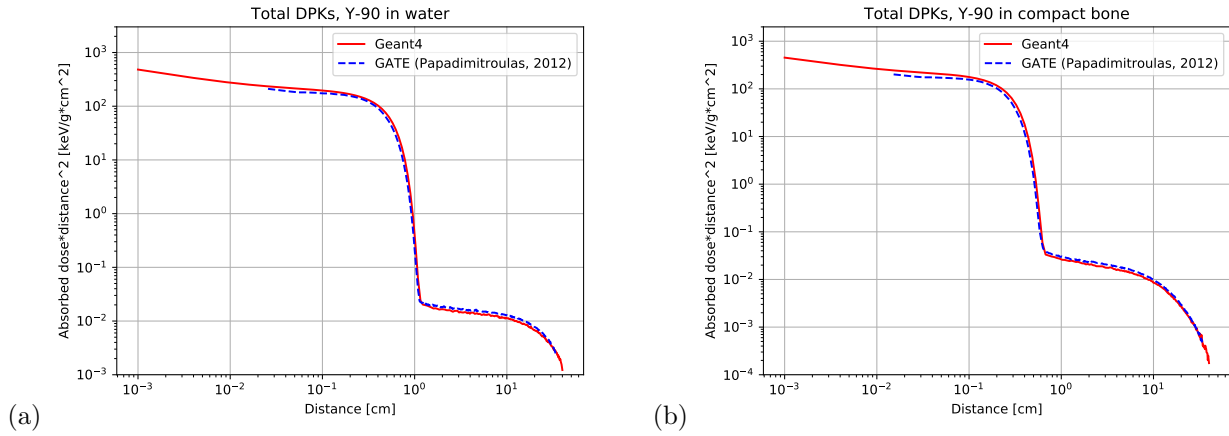
32

(a)
(b)

Figure 3.15: DPK total curve of ^{90}Y in (a) water and (b) compact bone using Geant4 with 10^7 events, compared with Papadimitroulas et al., 2012 using GATE.
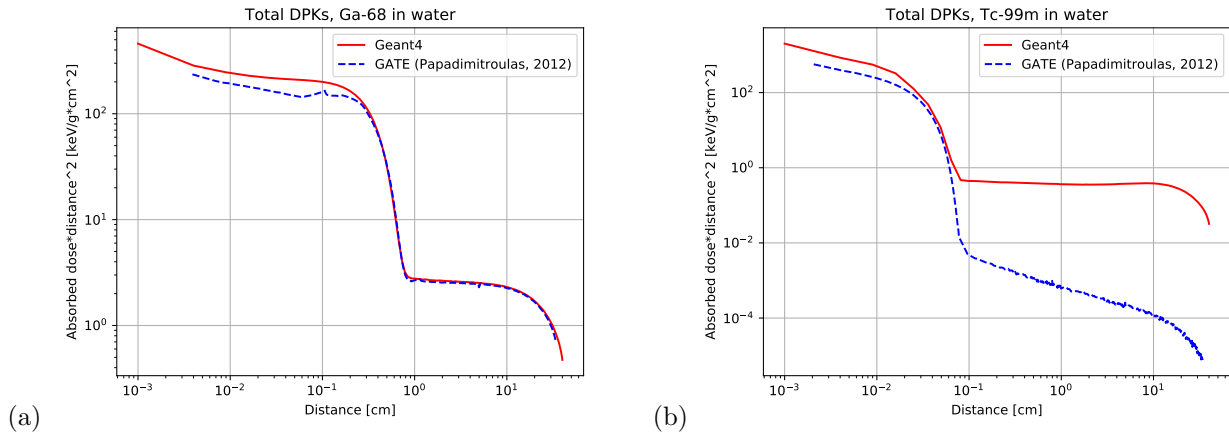

(a)
(b)

Figure 3.16: DPK total curve of (a) ^{68}Ga and (b) ^{99m}Tc in water using Geant4 with 10^7 events, compared with Papadimitroulas et al., 2012 using GATE.

(a)
(b)
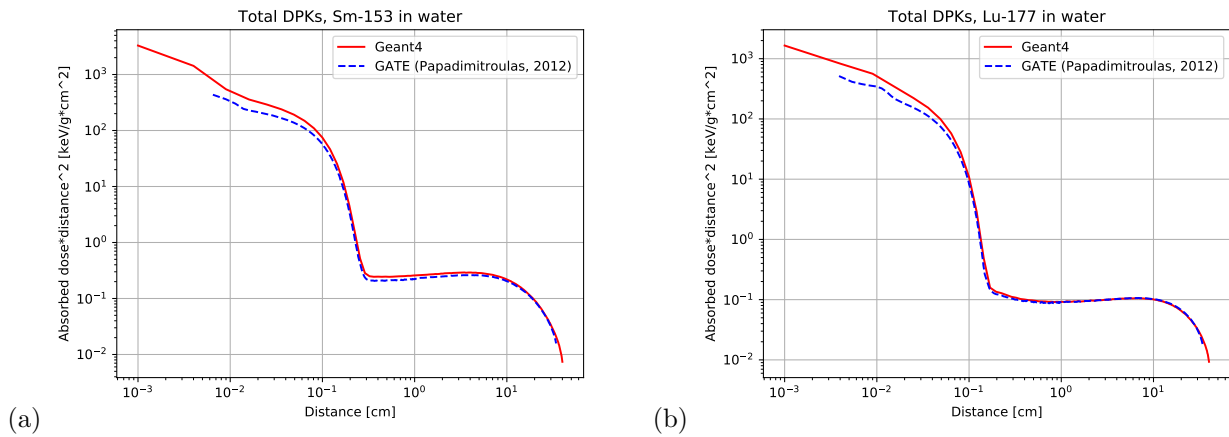
Figure 3.17: DPK total curve of (a) ^{153}Sm and (b) ^{177}Lu in water using Geant4 with 10^7 events, compared with Papadimitroulas et al., 2012 using GATE.
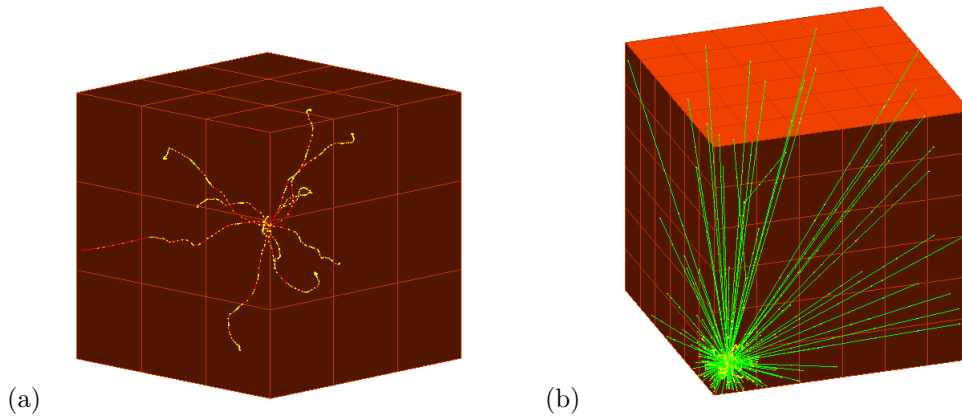
Figure 3.18: (a) Geant4 voxel-made cube with central source. (b) Source placed in a vertex.

3.3   Voxel S-Values (VSV)

Once completed the DPK part of the dataset, which will contain DPKs for all the mentioned nuclides both in water and compact bone, we are ready to move in the voxelized world that will host nearly all the remaining work from now on. The reason for that, as learned in Chapter 1, is that every medical image handled — CT, PET or SPECT — will be made of voxels. We can already point out that VSVs will not reach the same granularity at short range as the DPKs, since it is convenient for the former to have the same voxel size as the emission tomographies in order to convolve properly: typical voxel sizes in medical physics belong to the order of magnitude of 1 mm, for clinical imaging, or 0.1 mm, for pre-clinical studies on mice, whereas with DPK we reached about 0.01 mm in the inner shells.

As what matters is the dose at a certain distance from the source, this time the symmetry of the volume plays a more important role. One may intuitively think that, once built a virtual cube with an odd number of voxels N in its size, the central voxel should be chosen as source, like in Figure 3.18(a). However, this is not the best way to approach the problem, because it does not maximize the number of accessible distances from the source. Let us make a trivial example: if the source is centered, the eight vertices will stay exactly at the same distance from it, and this length — half the diagonal — will also be the maximum reachable. Instead, putting the source in a vertex, as in Figure 3.18(b), would unlock the access to several higher distances: considering again the vertices for simplicity and referring to a voxel in space using its own center, one will have

- the source voxel itself, at zero distance;

- three voxels with distance equal to the cube size, $L = (N-1)\,dx$ with dx being the voxel size;[2]

- three voxels with distance equal to the diagonal of a face, $\sqrt{2}L$;

- one voxel, the one on the opposite vertex, with distance equal to the diagonal of the cube, that will also be the farthest, $\sqrt{L^2 + 2L^2} = \sqrt{3}L$.

Furthermore, there is no more need to set an odd N. In conclusion, putting the source in a vertex allows to simulate the same distances as a cube almost[3] eight times bigger, with a great saving of both computational time and memory. The price to pay is a bit of statistics, since now each distance except zero has a lower multiplicity[4], but simulations with many events will not significantly suffer from this issue.

As also found in the reference studies Lanconelli et al., 2012 [29] and Amato et al., 2013 [30], since in a real medical voxelized image one does not know the exact position of the source inside a voxel, the decay events in the simulation should be uniformly distributed in the voxel volume. Besides the mentioned papers, which used respectively the Monte Carlo code DOSXYZnrc [31] and a previous release of Geant4, other valuable references are Pacilio et al., 2009 [32] and Lee et al., 2017 [33].

---

[2]If we have e.g. $N = 3$ voxels in a row, the distance from the center of first to the center of the third will be $2 \cdot dx$.

[3]The three slices containing the source voxel can not be repeated.

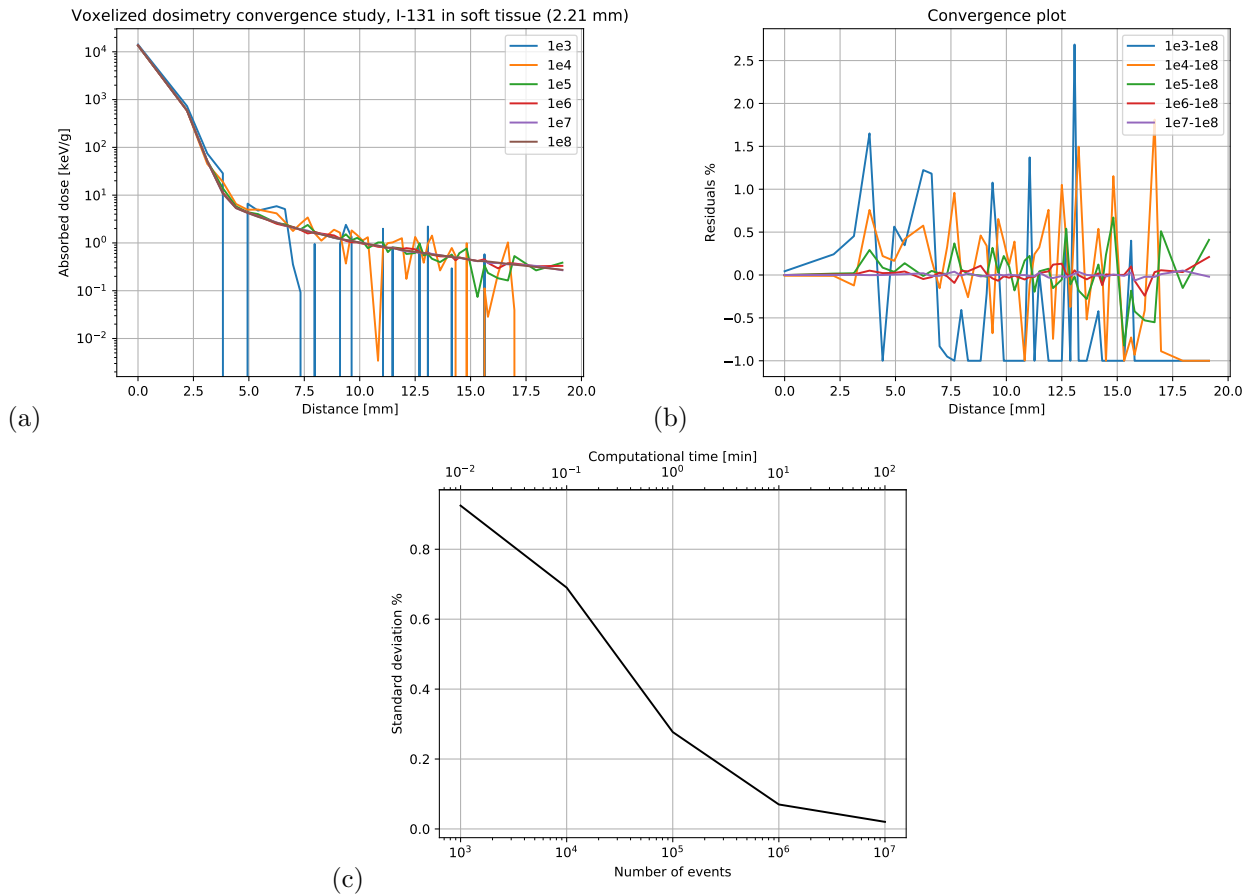[4]It is averaged on a lower number of voxels.

(a)

(b)

(c)

Figure 3.19: Convergence study for VSVs of ^{131}I in soft tissue; $N = 6$, $dx = 3$ mm.

It is clear that, placing the source in a vertex, a consistent part of the decay events will exit from the sensitive volume (1/2 of the total directly from the source voxel, since it has three internal and three external faces and the emission is isotropic). The outer world, initially composed by air, was turned into the same material of the cube in order to evaluate if there was a significant contribution of backscattered particles returning in. The result was practically identical, so the outer world was set to void in order not to waste computational time in tracing gone particles.

Dealing with VSVs, the ISOLPHARM database has the following features:

- it contains all the nuclides for whom the DPKs have been calculated;

- the materials used are compact bone and soft tissue ($\rho_{st} = 1.03$ g/cm^3), a generic compound approximating all the human soft tissues, chosen instead of water to better match with the pre-existing literature;

- the voxel size represents a variable as well: all the nuclides were simulated with $dx = 2.21$ mm and $dx = 3$ mm, which are typical parameters of clinical imaging devices, and with the pre-clinical value $dx = 0.5$ mm;

- $N = 6$ was adopted for every simulation.

For these simulations a 0.01 mm cut-off range was set for e and γ, as CPU time did not significantly increase. Occasionally, the most innovative nuclides such as ^{111}Ag may have also kernels computed in lung tissue and at higher clinical dx (5 mm and 9.28 mm); a complete summary of the VSV database content is inserted in Table 3.3. This time the plots will simply show absorbed dose in keV/g versus distance in mm.

Once again, ^{131}I is present in both references and will be used as a pilot radionuclide, as well as in the usual convergence study, illustrated in Figure 3.19. Like for the radioisotopic DPKs, we choose 10^7 events that in this case would keep the fluctuations below about 2% with respect to the highest

dx	^{18}F	^{64}Cu	^{68}Ga	^{89}Sr	^{90}Y	^{99m}Tc	^{111}Ag	^{111}In	^{131}I	^{136}Cs	^{153}Sm	^{177}Lu
0.50 mm	s,b,l	s,b	s,b	s,b	s,b	s,b	s,b	s,b,l	s,b	s,b	s,b	s,b
2.21 mm	s,b	s,b	s,b	s,b	s,b	s,b	s,b	s,b	s,b	s,b	s,b	s,b
3.00 mm	s,b	s,b	s,b	s,b	s,b	s,b	s,b	s,b	s,b	s,b	s,b	s,b
5.00 mm							s,b			s,b		
9.28 mm							s,b			s,b		

Table 3.3: All the material and dx combinations contained by the VSV part of the database; the letters s,b,l stand for soft tissue, bone and lung.
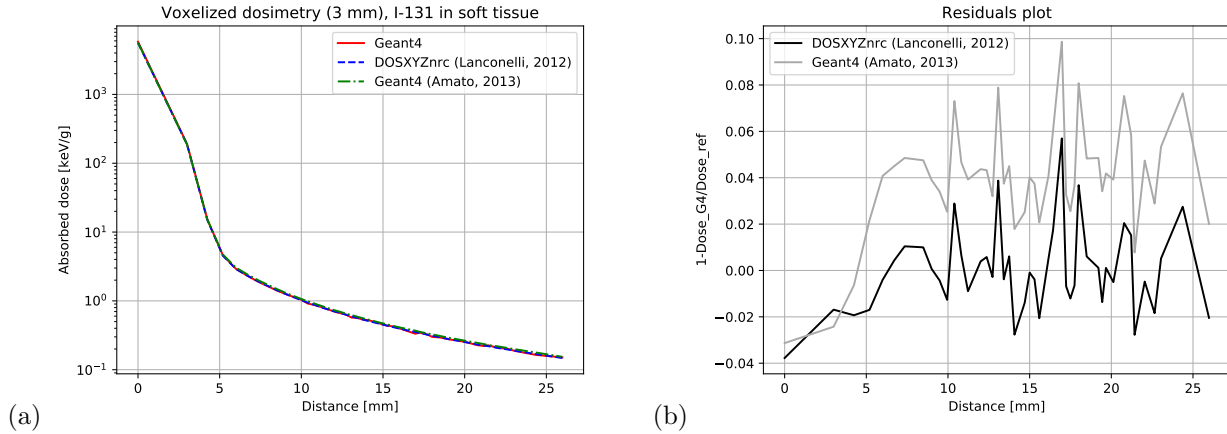

Figure 3.20: (a) VSV curve of ^{131}I in soft tissue using Geant4, compared with Lanconelli et al., 2012 using DOSXYZnrc and Amato et al., 2013 using Geant4; $N = 6$, $dx = 3$ mm. (b) Residuals plot.

statistics of 10^8. From the VSVs in Figure 3.20(a) we can see again a steep slope β^- shoulder and a slight slope γ; the agreement between the three curves looks excellent, whereas the residuals in Figure 3.20(b) say that the difference between the two releases of Geant4 is higher with respect to this study and DOSXYZnrc.

Passing to ^{111}Ag, which in this case was completely absent from literature, we can observe the behavior of the VSVs under variation of tissue, as in Figure 3.21(a), and of voxel size, as in Figure 3.21(b); it is clear that in the latter case we can expect very different values in the first voxels, as dx becomes way longer than the average range R_{csda} of the β^- electrons emitted by ^{111}Ag, which is about 1 mm [21]. This means that volume and mass go like dx^3, while the radiation core increases very slowly after R_{csda}, assigning lower doses to bigger voxels.

Now, since the previous section instilled some doubts about the coefficients of ^{99m}Tc, we can proceed with Figure 3.21(c); surprisingly, we notice that the disagreement has moved from the γ shoulder to the β^-. Actually, a possible explanation might be that the reference, contrary to this research, did not include the subsequent β^- decay from ^{99}Tc to the stable isobar ^{99}Ru; so literature, whose β^- curve is one order of magnitude smaller, may be representing just the internal conversions and Auger emissions of the metastable state, that compete against photons with branching ratio $\sim 11\%$. Under this assumption, what matters to us is that the γ side agrees perfectly, corroborating the hypothesis of GATE dysfunction we made in the previous section for ^{99m}Tc. Anyway, the decision to kill the g.s. in the simulation makes sense, since it has not the same half-life as the metastable: it is actually much longer, $t_{1/2}^g = 2.111 \cdot 10^5$ y versus $t_{1/2}^m = 6.0072$ h [12], so a real situation would be hardly affected by its contribution. The best choice for a VSV database would probably be to simulate both states separately, as the information about the activity of ^{99m}Tc provided by SPECT can be renormalized to ^{99}Tc and one may perform two subsequent convolutions to reproduce the real situation; a simple model on how to do this will be developed in Appendix B.

Figure 3.21(d) shows instead a pre-clinical VSV example for ^{18}F — the most common radionuclide in PET, as stated in Chapter 1 — with $dx = 0.5$ mm; those VSVs will be useful in the next section for the convolution. Two pure β^--emitters (^{89}Sr and ^{90}Y) and two heavier nuclei (^{153}Sm and ^{177}Lu) are

(a)

(b)

(c)

(d)

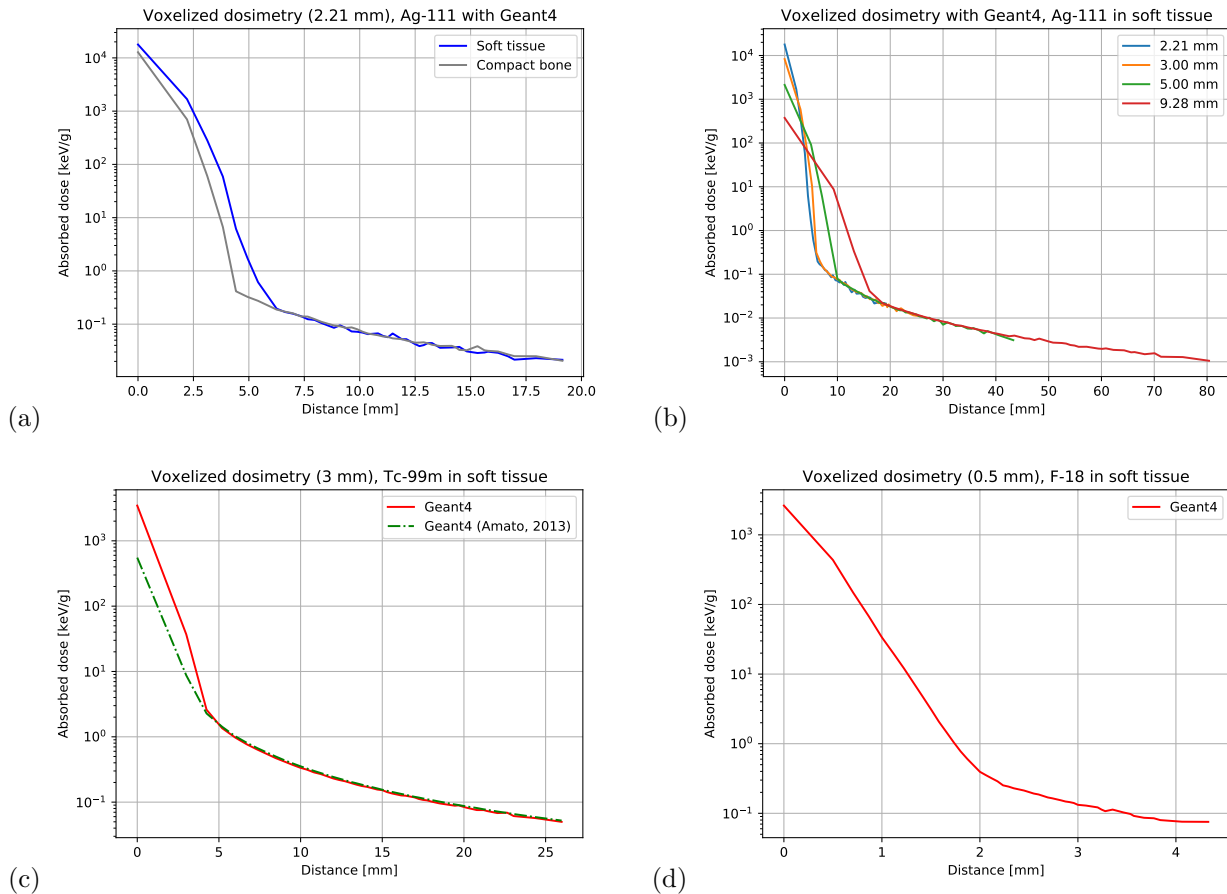Figure 3.21: (a) VSV curves of ^{111}Ag in soft tissue and compact bone using Geant4; $N = 6$, $dx = 2.21$ mm. (b) VSV curves of ^{111}Ag in soft tissue using Geant4 at different values of dx.(c) VSV curve of ^{99m}Tc in soft tissue using Geant4, compared with Amato et al., 2013; $N = 6$, $dx = 3$ mm. (d) VSV curve of ^{18}F in soft tissue using Geant4 at the pre-clinical voxel size of $dx = 0.5$ mm.

then treated in Figure 3.22:

- the former demonstrate an excellent agreement in the β^- shoulder, eased by the high statistics descending from the high E_β (about 600 and 900 keV) that generates a lot of secondary e$^-$; for the same reason, having poor statistics, the γ side presents a certain level of noise;

- the latter agree very well with Lanconelli et al., 2012, whereas there is an underestimate of the γ contribution with respect to Amato et al., 2013, probably due to the older release of Geant4 used in that study.

Finally, a summarizing point of view is offered in Figure 3.23, where all twelve investigated radionuclides are compared to each other. If we proceed focusing on the therapeutic β radiation, the most energetic nuclei are of course the two pure β^--emitters mentioned a little while ago, together with ^{68}Ga. Such nuclide, a β^+-emitter suitable for PET and already employed in nuclear medicine, is very particular because it unites an amount of photons comparable to ^{18}F to a massive energy deposition in the first few mm from the source; naturally, these features make it really powerful from a theranostic point of view. After these three, we find our most interesting candidate, ^{111}Ag. Its radiation appears very similar to the one of ^{177}Lu but with a higher energy release from the β^- particle (see the thick lines in the graph); ^{177}Lu is currently used in cancer therapy even with theranostic application [34], therefore if the ISOLPHARM goal of producing radiopharmaceuticals labelled with ^{111}Ag will be accomplished, there is no reason not to think that, in the future, such radiolabelled drugs could be approved for theranostics by the national and international agencies. Then all the other nuclides follow until the last one, ^{111}In, which is obviously the least energetic since it is the only one not to undergo any β decay.
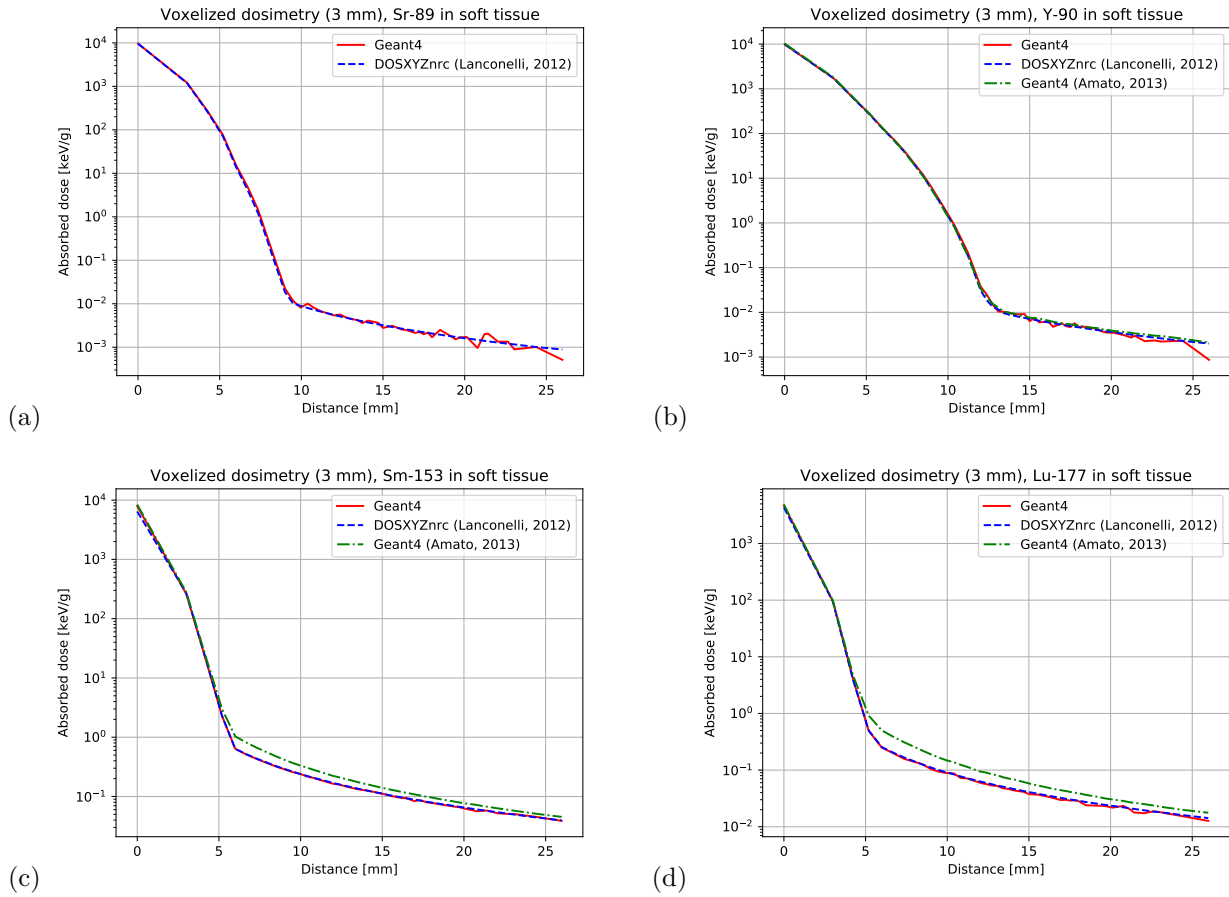
Figure 3.22: VSV curves of (a) ^{89}Sr, (b) ^{90}Y, (c) ^{153}Sm and (d) ^{177}Lu in soft tissue using Geant4, compared with Lanconelli et al., 2012 using DOSXYZnrc and Amato et al., 2013 using Geant4; $N = 6$, $dx = 3$ mm.
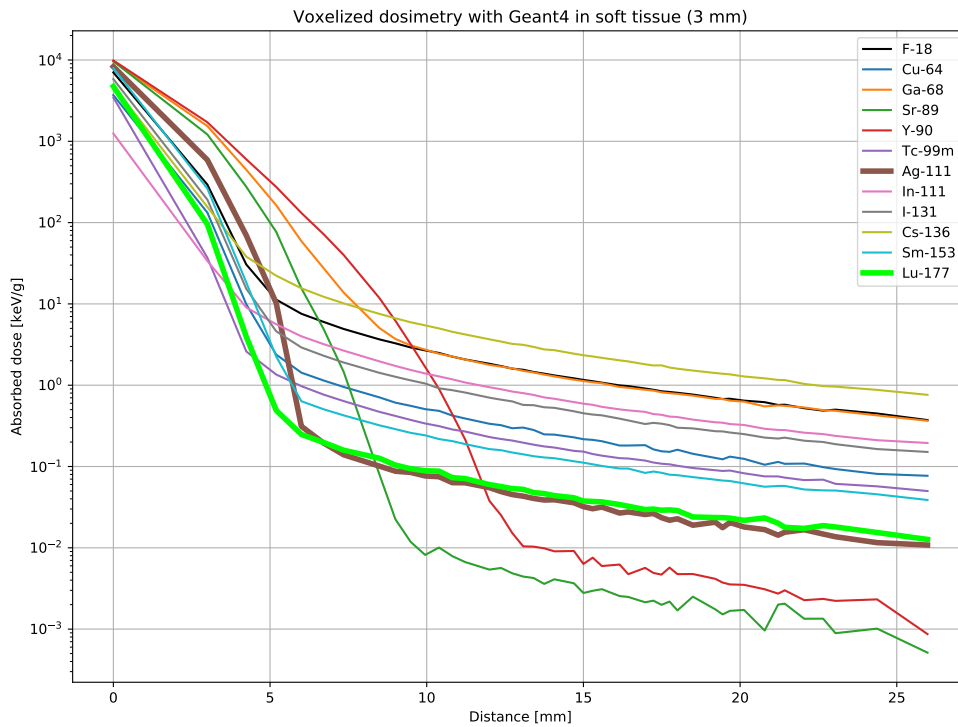

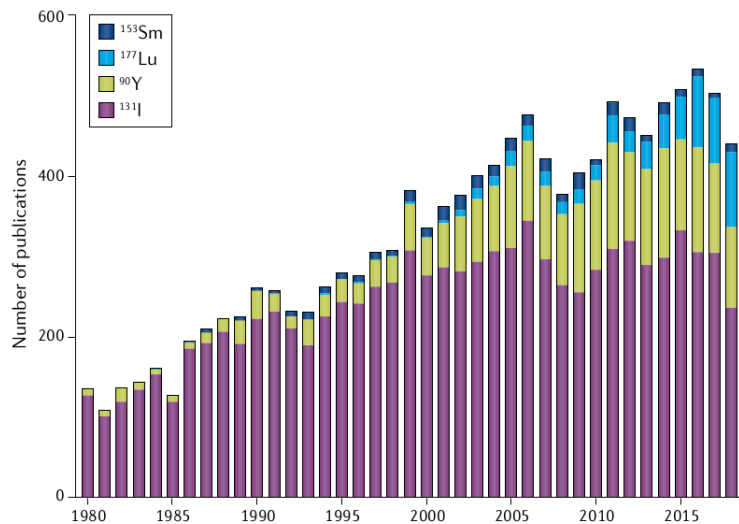Figure 3.23: VSV curves of all the nuclides of interest in soft tissue using Geant4; $N = 6$, $dx = 3$ mm.

Figure 3.24: Scientific publications dealing with β^--emitters in TRT in the latest years. [35]

We conclude by showing Figure 3.24, that displays the latest research trend of β^--emitters in TRT; the employment of ^{177}Lu is constantly growing, so we might hypothesize that a similar role could be played by ^{111}Ag in the future.

3.4 Convolution

Now that the VSV database has been built, it may be useful to provide a demonstration of how it can work. The convolution operation could reveal itself computationally very expensive if applied to an emission tomography, as ordinary numbers of voxels in such a 3D image are, considering just the order of magnitude, $10^2 \times 10^2 \times 10^2$, corresponding to $\sim 10^6$ voxels. Fortunately, one can speed up the counts recurring to the Fourier transforms, which can turn the convolution into a simpler product in the following way.

The *convolution theorem* states that the Fourier transform of the convolution between two functions is equal to the pointwise product of their transforms, namely

$$\mathcal{F}[A * S] = \mathcal{F}[A] \cdot \mathcal{F}[S] \tag{3.5}$$

where A and S stand for our functions of activity and S-values, $*$ represents the convolution as previously defined and $\cdot$ is the pointwise product. It is then sufficient to apply the inverse Fourier transform to both members to see that

$$A * S = \mathcal{F}^{-1}\big[\mathcal{F}[A] \cdot \mathcal{F}[S]\big] \tag{3.6}$$

which is the exactly the equation we were searching for. A discrete $\mathcal{F}$ must be used due to the discrete nature of our objects. All these operations can be done using the FFT (Fast Fourier Transform) functions available on the Python3 library *Numpy* and take just a few seconds.

Of course, to show an example we need an image: the one we are going to use comes from a pre-clinical hybrid PET/CT imaging of a mouse, performed at INFN Southern National Laboratory (LNS) with the γ emission of the radiolabelled drug ^{18}F-FDG. FDG stands for *fluorodeoxyglucose*, i.e. a glucose analog containing a fluorine atom which can obviously be a radioisotope. The resolution is 0.5 mm for both PET and CT, so the VSV kernel to use is precisely the one reported in Figure 3.21(d).

Figure 3.25 shows, in the upper row, the superimposed PET/CT of the mouse; CT is represented in greyscale in the background, as it will always be from here on, whereas the red and yellow colormap represents the activity per voxel volume (in kBq/mL) provided by the PET. The numbers around the graphs represent the number of voxels in the three dimensions (originally $148 \times 160 \times 160$ but some empty slices were cut to speed up the counts); our kernel has $N = 6$, so an equal tensor having the VSVs in its $11 \times 11 \times 11$ core was built. We should dwell for a while on this view, which first of
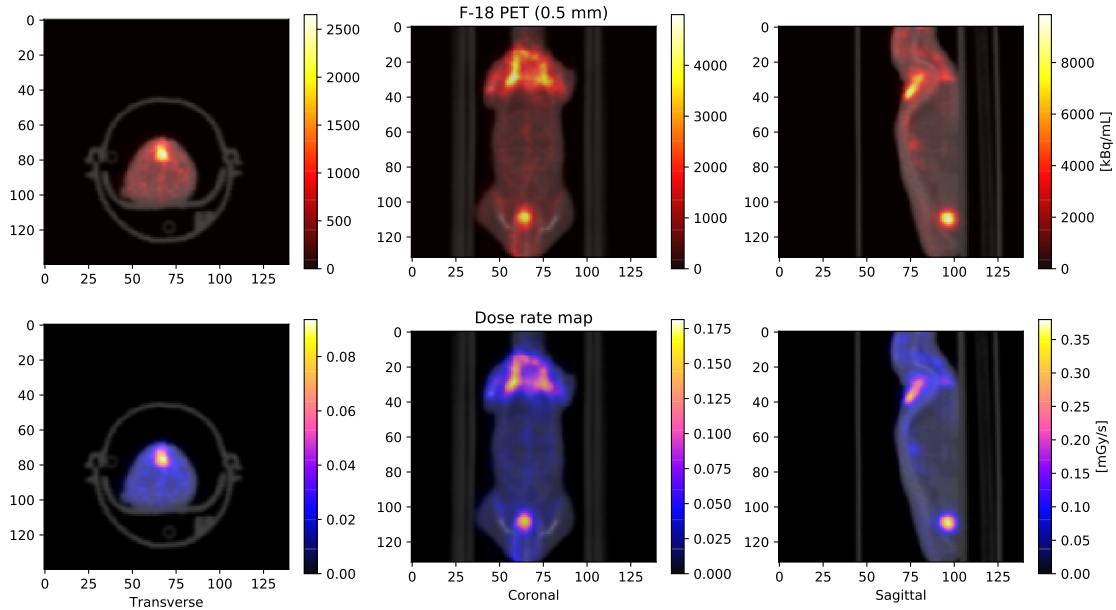
Figure 3.25: Upper row: ^{18}F-FDG PET/CT image of LNS mouse in the three anatomical planes. Lower row: dose rate map computed by convolution in the 100% soft tissue approximation.

all allows us to face what is happening in the murine body. The brighter zones in the upper coronal and sagittal planes correspond more or less to the mouse's shoulders, i.e. the region where usually tumours are inserted in pre-clinical experiments; a high concentration of glucose is expected in cancer masses, so a great amount of radiopharmaceutical should be found there. The other bright spot in the lower body corresponds instead to the urinary bladder; such an organ is also expected to contain a lot of activity, being the final collector of the excretory system which gradually removes undesired substances like FDG; naturally, depending on the PET acquisition time, the urinary bladder can be found more or less filled with radioactive urine due to urination. Finally, the grey objects around the mouse are clearly part of the instrumentation.

As our first try, let us work under the approximation that the whole phantom is composed by soft tissue. If a convolution between the PET activity and the ^{18}F VSVs at $dx = 0.5$ mm is performed, one obtains the results displayed in the lower row of Figure 3.25, i.e. the dose rate in each voxel, here expressed in mGy/s. The activity distribution is pretty much reflected in the dose rate map and in fact, remembering the shape of our kernels, we can expect a higher deposition of energy right next to the radiation sources. For completeness, an analogous convolution using the ^{18}F DPKs in water (which are visible in Figure A.1(a), Appendix A) has been performed. This was possible by means of a conversion procedure that appended the DPK interpolated values to a $11 \times 11 \times 11$ tensor kernel; this tensor allowed to include most of the γ contribution, but also a bigger kernel could be used. The result is displayed and compared with the VSV in soft tissue in Figure 3.26: neglecting the small discrepancy between water and soft tissue, the dose rate distribution appears less peaked on the sources, probably because, contrary to the tiny DPK core ($dr_0 = 0.02$ mm), the size of the source voxel dx is comparable to the average range of the β^+ radiation of ^{18}F in water, $R_{csda} \sim 0.6$ mm [21]. This means that VSVs already reach their maximum dose at the shortest distance, whereas DPKs form a hump.

The approximation of 100% soft tissue is not so far from reality, but further attempts can be made in order to improve this first result. For instance, using the masking tools provided by Python3, it is possible to perform the convolution only on a region of the phantom: this means that one can convolve different organs with the kernels calculated in the associated tissues. To do this, first of all, we have to deal with the CT; as we will see, murine Hounsfield units in pre-clinical experiments often need a calibration and one can not relate them *a priori* to a particular tissue. As this CT was not calibrated,

Figure 3.26: Upper row: dose rate map of LNS mouse computed by DPK convolution in the 100% soft tissue approximation. Lower row: difference between this dose rate and the VSV result.
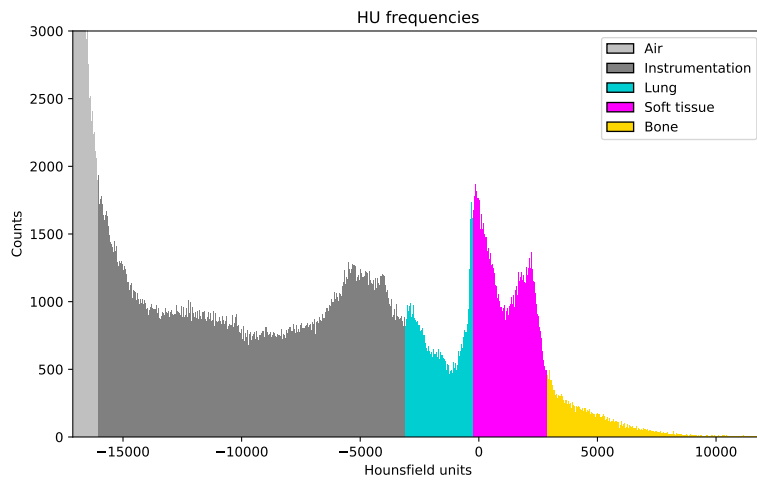
Figure 3.27: Histogram of the Hounsfield units frequencies for LNS mouse highlighting the most characteristic tissues.

Tissues	HU interval
Air	$[-17117, -16000]$
Instrumentation 1	$[-16000, -9700]$
Instrumentation 2	$[-9700, -2500]$
Lung	$[-3100, -200]$
Soft tissue	$[-200, 2900]$
Compact bone	$[2900, 32766]$

Table 3.4: Hounsfield units intervals corresponding to the main tissues in LNS mouse.

41
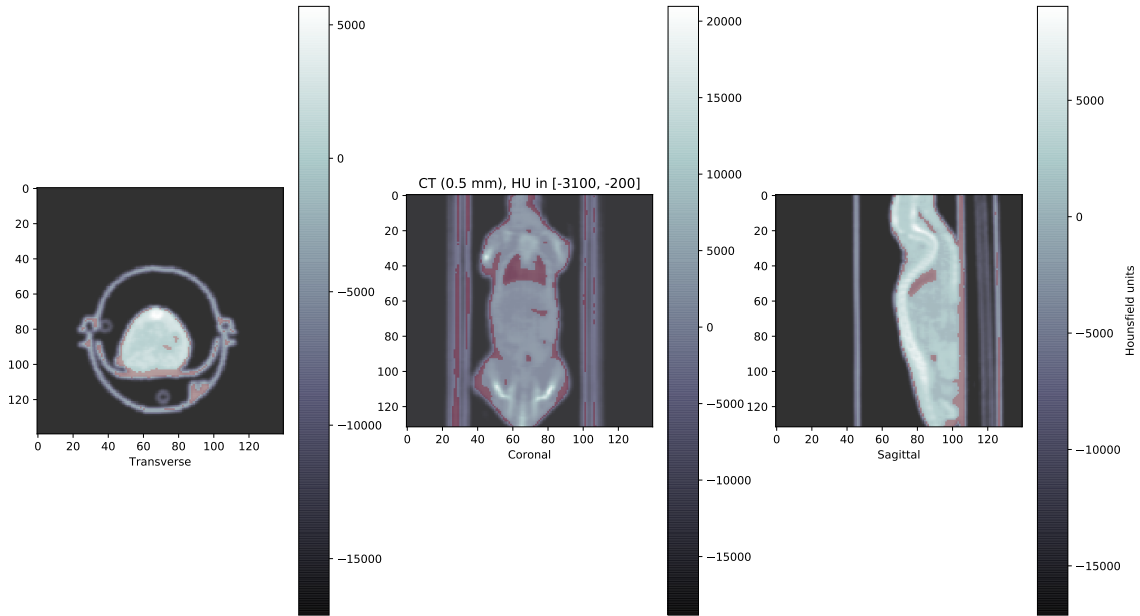
Figure 3.28: CT with the window HU $\in [-3100, -200]$, supposed to host the lungs, highlighted in red.

a Python3 tool was developed to approximately calibrate the HU by visualizing certain selected tissues and assessing their HU window. It is important to underline that our current requirements imply that also the CT must have a resolution of 0.5 mm to correctly execute the cuts with the masking tools. However, 0.5 mm is not the best resolution for pre-clinical CT imaging, so the borders between organs will not always be clear with this images, but we will try as well to isolate some organs.

It turned out that the Hounsfield units in our CT were staying in the interval HU $\in [-17117, 32766]$. The most important tissues to be identified are at least two, i.e. the farthest from the definition of soft tissue:

- compact bone, which as we saw is denser than soft tissues;

- lung, expected to be less dense instead.

With our tool we are able to observe the distribution of the Hounsfield units, like in Figure 3.27, investigate a particular HU interval, as in Figure 3.28 with lung, and calibrate the HU for the tissues we are interested in (again Figure 3.27 with the colored regions and Table 3.4). As appearing from the figures and the table, HU overlaps between different tissues are not unusual; we can see for instance that the lung interval includes some other minor organs — maybe pancreas, deducing from the coronal plane in Figure 3.28 — and part of the instrumentation, too. Of course in the histogram some peaks may appear, but they do not have to be automatically associated to a particular tissue, due to overlaps especially for soft organs and to the different volumes occupied by the tissues; bone, for instance, seems to follow a shoulder trend rather than a sharp peak, since it is not present below HU $= 2900$.

With this information, it is possible to implement the cuts in our Python3 convolution procedure just like in Figure 3.29, where the compact bone and lung masks are compared to the complete CT. Both cuts include some fragments of intruder tissues due to overlaps or border effects; the latter characterize the lung tissue since it always presents lower HU than the soft tissues and, when these share a discontinuity with the outer (or sometimes inner) air, HU typical of the lung can be found. As a matter of fact, in the lower row it seems like the mouse's skin is made by lungs. Anyway, CT images with lower dx together with methods to reach a much higher precision will be adopted in the following chapter, where some of this problems will be solved.
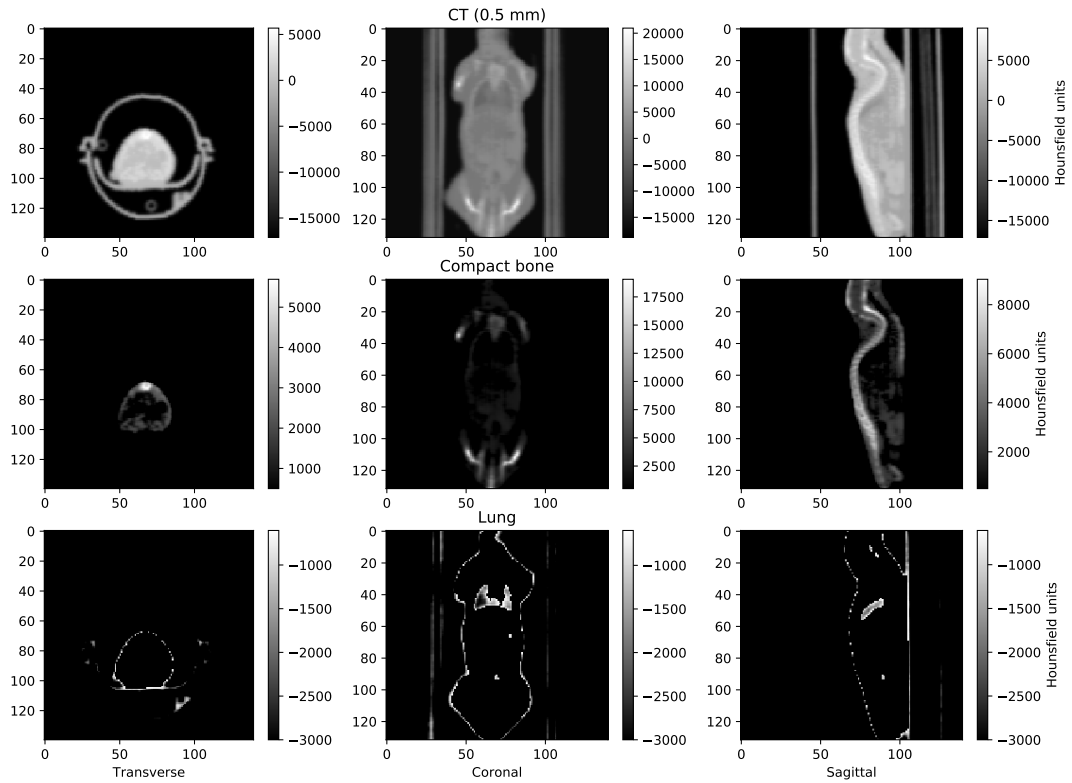
Figure 3.29: Full CT compared with the cuts of compact bone and lung in the three anatomical planes.
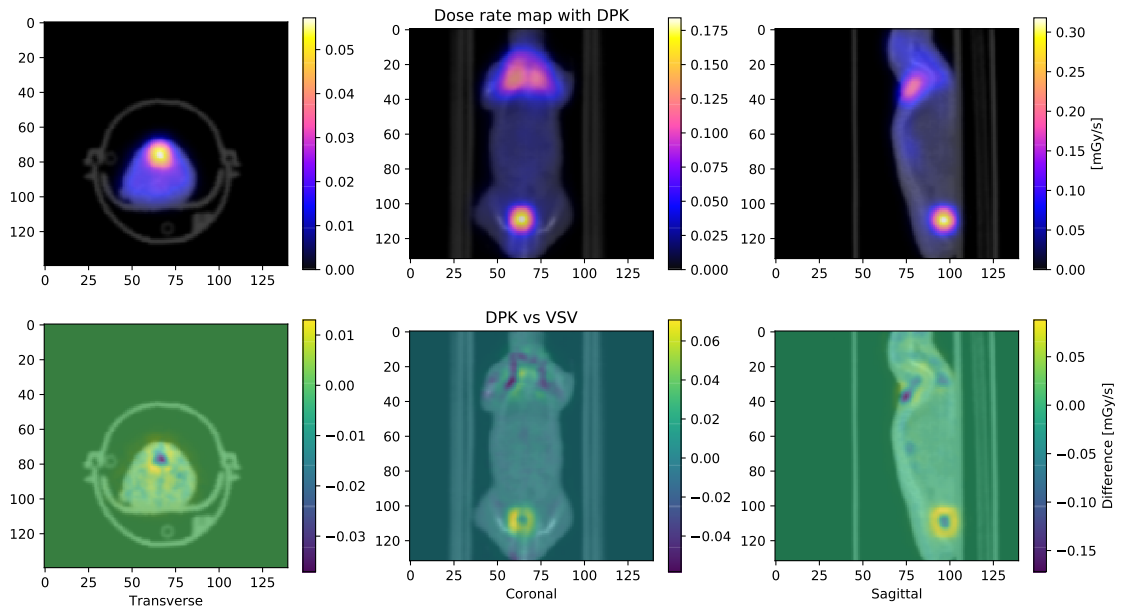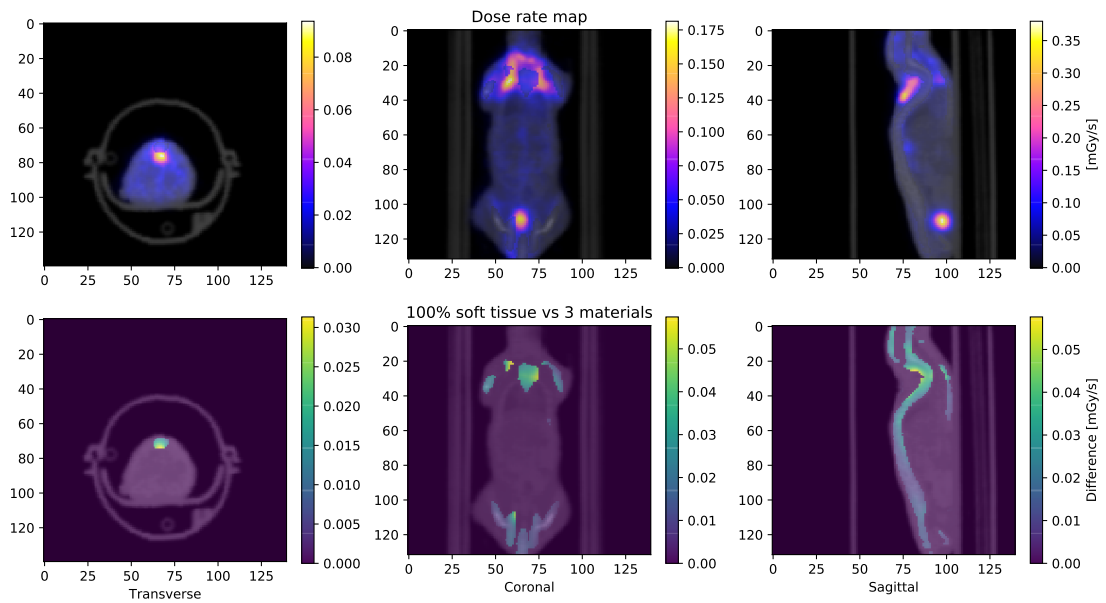

Figure 3.30: Upper row: dose rate map of LNS mouse computed by convolution in the 3 tissues (soft-bone-lung) approximation. Lower row: difference between and the 100% soft tissue result and this dose rate.

Since the aim of this section is just to give an example of how the MIRD schema works, we can finally move to Figure 3.30, where the masks were applied to the convolution. Obviously, VSVs for ^{18}F in compact bone and lung were computed and added to the database. In the upper row we can visualize some darker spots in the most radioactive zones due to the presence of bones; the lower row shows the difference between the 100% soft tissue approximation and this case: as expected, there is a clear hindrance in bones, since their density is quite higher and the absorbed dose is inversely proportional to the mass where the energy is deposited. On the other hand, we do not appreciate substantial variations in lungs probably because the Geant4 material database considers empty lungs, with no air inside and density $\rho_l = 1.04$ g/cm^3, practically equivalent to the other soft tissues. We will look for a more realistic representation of this tissue in the next chapter.

Chapter 4

Direct Monte Carlo

The second technique of computed dosimetry that will be employed in this thesis can be simply identified as Direct Monte Carlo. It is conceptually simpler than the MIRD schema — even though the simulation part is heavier and more time-expensive — and it is expected to be more precise. The common features with the MIRD formalism are the use of the Monte Carlo method, even if at different levels, and the importance of PET or SPECT images to obtain information about the activity distribution, as well as CT for the morphological characteristics of the sample. First of all, the method will be introduced and then we will connect to the end of the previous chapter by applying the Direct Monte Carlo dosimetry to the same phantom used there.

4.1 Working principle

This procedure is present in several published researches; as reference literature, we suggest the papers Gupta et al., 2019 [36] and Pistone et al., 2020 [37]. The working principle is quite easy and consists in the following main points.

1. Voxelized reproduction of the entire sample, including its material composition, by exploiting the CT in a Monte Carlo software like Geant4.

2. Taking the activity from the PET or SPECT imaging in the sample as a probability distribution for the Monte Carlo events.

3. Simulation of an arbitrary number of events to be later normalized or directly of the number of events corresponding to the total activity in the PET or SPECT (Figure 4.1).

4. Collection in each voxel of the dose rate or, if the activity was cumulative, of the absorbed dose in a time window.

Most of this steps, actually all apart from the first one, can be automatized by means of Geant4, Python3 and ROOT [38] scripts. The construction of a sample corresponding to the CT requires instead an accurate analysis of the Hounsfield units as we did in Section 3.4 and an appropriate
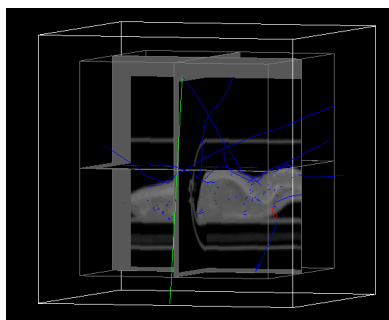

Figure 4.1: Direct Monte Carlo simulation on a murine phantom with the Geant4 interface GATE.

Geant4 materials	Composition	Density [g/cm^3]
Air	N 76%, O 23%, C, Ar	0.00120479
Water	H 67%, O 33%	1
Soft tissue ICRP	O 60%, C 26%, H 11%, N, Na, P, S, Cl, K	1.03
Compact bone ICRU	O 41%, C 28%, Ca 15%, P 7%, H 6%, N, Mg, S	1.85
Lung ICRP	O 78%, H 11%, C 8%, N, Na, P, S, Cl, K	1.04
Lung MOBY	O 74%, H 10%, C 10%, N, Ca, P	0.30

Table 4.1: Used materials from Geant4 with their density, composition and percentage fraction of the main (> 5%) components. [2] [3] [39] [40]

handling of the 3D images, for example reading files in DICOM format with the software mentioned above. We could focus for a while on this point, since up to now we talked about tissues from the Geant4 material database without giving any further details in addition to density. It is now worthwhile to introduce what it means to consider a material on Geant4.

The Geant4 software permits to build a virtual volume and fill it with a material. The composition and density of this material are mimicked with the goal of reproducing in a reliable way the reactions and the scattering of an incident radiation. A dataset of materials — from which we already took air, water, compact bone, soft tissue and lung — is available in the user documentation. Anyway, there is also the possibility to generate a material by oneself, providing the information about its density, its ionization energy, its atomic components and their percentages. One can also find such information for the tissues already appearing in the database. Table 4.1 shows the characteristics of the materials used up to now, and adds an alternative definition of lung found in the user documentation of GATE. This lung model, tagged as MOBY [40], comes from a set of 3D and 4D[1] murine phantoms available on the market in order to perform accurate simulations for pre-clinical experiments. Since it approximates a proper murine lung instead of a human one, it may result convenient to use it, also to give a better characterization of lungs, which should be less dense than soft tissues at least in a respiration average. Anyway, we will still use lung ICRP in the next simulation in order to compare its dose rate map with the convolution.

In conclusion, one should be able firstly to read the CT images accessing to their values in Hounsfield units and develop an algorithm capable to assign correctly the corresponding materials to an empty voxelized phantom. In the next example, the same HU intervals as in Chapter 3 (Table 3.4) will be used, but later we will try to improve our strategy.

4.2 Comparison with MIRD schema

Now that the Direct Monte Carlo dosimetry procedure and the Geant4 definition of material have been clarified, we can try and replicate the final results of Chapter 3 in order to compare the two techniques. Simulations of $1.65 \cdot 10^7$ events, corresponding to the total activity in Bq measured by the PET, were launched on the Geant4 interface GATE; practically, an instantaneous photograph of the dose rate was obtained by running all the decays that occur in 1 s. In Figure 4.2, upper row, the dose rate map obtained with the new method in the 100% soft tissue approximation is illustrated and, if we move to the lower row, the difference between this map and the one computed by convolution in the same approximation reveals a good agreement, with deviation below 10%. In particular, we observe that the direct method tends to have a small excess of dose with respect to the other. This probably occurs because the use of VSVs calculated with $N = 6$ means a tensor kernel with size $11 \times 11 \times 11$ voxels, i.e. for each source the information about what happens outside this cube gets lost; the brightest γ radiations, such as the one following the β^+ decay of ^{18}F used here, should be affected by this behavior more than short range emitters. A few voxels present also a negative difference, anyway really small, probably due to fluctuations in the Monte Carlo.

Using the same mechanisms as before to assign the tissues to the sample's voxels — i.e. roughly

---

[1]Including time effects like respiration and heartbeat.

Figure 4.2: Upper row: dose rate map of LNS mouse computed by Direct Monte Carlo in the 100% soft tissue approximation. Lower row: difference between this dose rate and its homologous obtained following the MIRD schema.
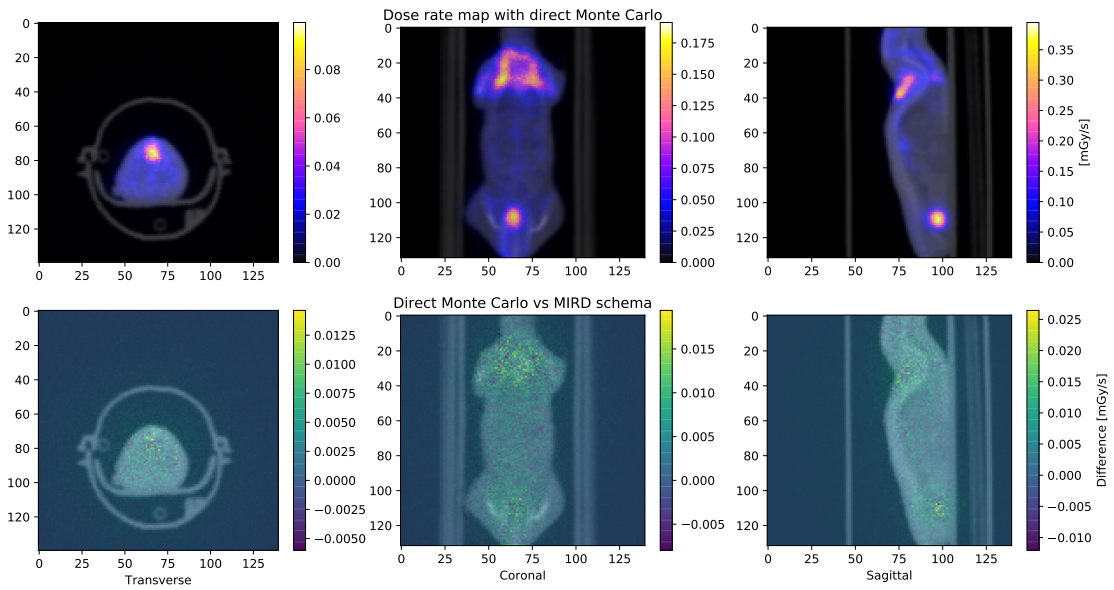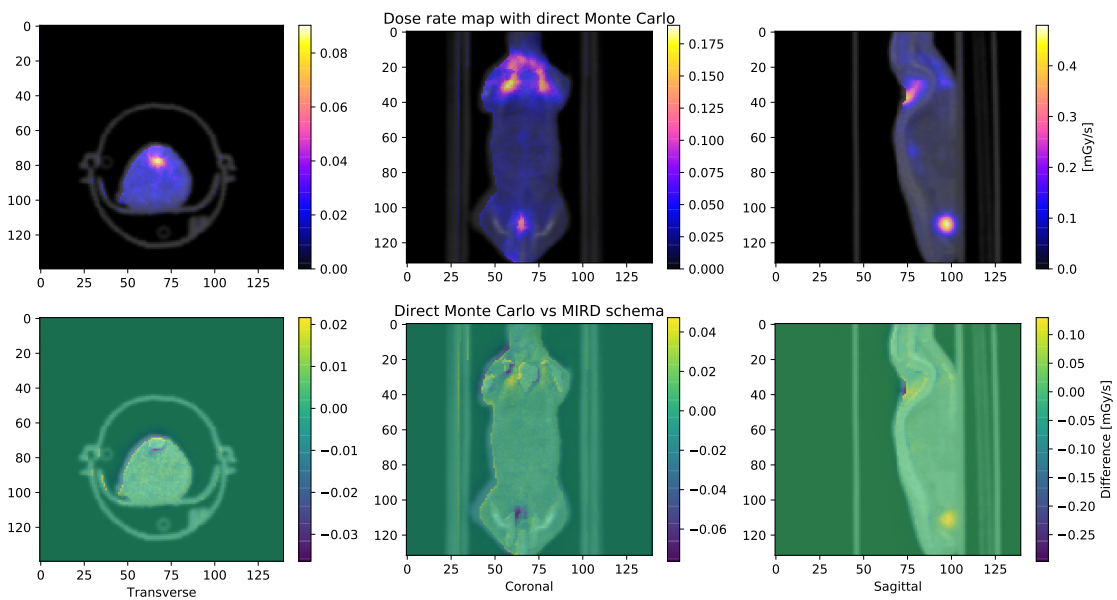

Figure 4.3: Upper row: dose rate map of LNS mouse computed by Direct Monte Carlo in the air-soft-bone-lung approximation. Lower row: difference between this dose rate and its homologous (without air) obtained following the MIRD schema.

identifying all voxels having their Hounsfield units within a certain interval with the correspondent material —, we proceed with the Direct Monte Carlo dosimetry in a phantom made of air, soft tissue, compact bone and lung (ICRP). The material selection appeared to be easier on Geant4 rather than on its interface GATE so, remembering that the underlying software is literally the same, we returned to the main version of Geant4. Furthermore, error diagnostic is more comfortable and a higher number of features can be controlled by the user. The first effort was made inserting air outside the mouse's body, where the Hounsfield units allowed it; however, in this way, huge amounts of dose rate appeared in the air voxels, since the small deposited energy divided by the smaller air mass yielded divergent values. This problem was solved by sending automatically to zero the dose rate in air, as we are not interested in it. The results are represented in Figure 4.3, upper row. In the lower row this simulation is compared with its homologous computed by the MIRD schema, which actually had soft tissue instead of air. We can still see a border effect due to air just outside the mouse, where in fact the convolution has higher values. Other discontinuity effects are visible inside the body; two main issues may occur indeed in the MIRD schema:

- the radiation getting out from a tissue A and passing through another tissue B is not counted, since different kernels undergo separate convolutions: Direct Monte Carlo may result higher in B;

- in the case of a double discontinuity of the kind ABA, the dose from the first A layer can bypass B and reach the second A layer: there, Direct Monte Carlo may be lower or higher depending on the density of B with respect to A.

In conclusion, from this section it emerges that, when considering different tissues, the MIRD schema might not reproduce the results as precisely as the Direct Monte Carlo dosimetry for the reasons we have just underlined. The main advantage of the former method is computational time, namely a few seconds versus about 100 min with CPU Intel i5-9600 (6) @ 4.6 GHz for a simulation of this type (assuming to already have the convolution kernels), but, on the other hand, the latter guarantees an undoubtedly higher precision. Thinking of what we are going to do next in this work, the computational time of Direct Monte Carlo is certainly sustainable; therefore our decision is to choose the second method for the remaining activities, whose goal is to provide a few indications about how to theorize a radiopharmaceutical biodistribution in time and, using such a model, how to integrate a dose rate over a time interval in order to finally obtain the absorbed dose.

4.3 Biodistribution model

This section will try to develop a reliable mathematical model for the time evolution of a radiopharmaceutical biodistribution mediated by transport kinetics. In particular, we are interested in the activity in a region of interest (ROI) or volume of interest (VOI) — such as an organ, a tissue or a cancer — after a time t from the injection. The following considerations are partially inspired by the works of Shevtsova and Shevtsova, 2017 [41], Sato et al., 2021 [42] and Watabe et al., 2006 [43].
Let us imagine a system representing the whole murine or human body and subdivided into two compartments:

- compartment 1, corresponding to the ROI;

- compartment 0, comprehending the rest of the body.

From a biological point of view, the key of this theoretical scaffold is the transport mechanism mediated by the cell membrane. Suppose to inject a radiopharmaceutical intravenously: it will travel in blood (compartment 0) until it binds a cell receptor of the ROI (compartment 1) or until it gets collected by the excretory system for the elimination. Anyway, even in the ROI a certain number of drug molecules per time unit will undergo the inverse process and return to compartment 1: a continuous exchange happens, and it would go on indefinitely, if radioactive decay and biological expulsion did not play their own roles. Hence, there are at least three physical and biophysical processes that must be considered in the development of such a model:

- the radioactive decay of the radionuclide, mediated by the disintegration constant λ;

- the radiopharmaceutical exchange between the compartments, modulated by the transition rates $0 \to 1$ and $1 \to 0$, which will be called h and k;

- the elimination of the radiopharmaceutical from compartment 1 due to the excretory system, which collects it in the urinary bladder in order to expel it; the transition rate $0 \to$ elimination will be referred to as l.

Like λ, the transition rates have the dimensions of an inverse time; such a characterization is typical of *Markov processes*, i.e. stochastic processes where the transition between two states does not depend on how the first state was reached. With these definitions, one can now write the following homogeneous linear system of differential equations with constant real coefficients, identifying the number of radionuclides in the two compartments N_0 and N_1 at time t:

$$\begin{cases} \dot{N}_0 = -(\lambda + h + l)N_0 + kN_1 \\ \dot{N}_1 = hN_0 - (\lambda + k)N_1 \\ (N_0(0), N_1(0)) = (N_{in}, 0) \end{cases} \tag{4.1}$$

with λN_{in} being the total injected activity (TIA). Summing over the compartments, we obtain the behavior in the whole body:

$$\dot{N} = \dot{N}_0 + \dot{N}_1 = -\lambda(N_0 + N_1) - lN_0 = -\lambda N - lN_0 \tag{4.2}$$

Defining $h' \equiv -(\lambda + h + l)$ and $k' \equiv -(\lambda + k)$, the system can be written in the matrix form

$$\begin{pmatrix} \dot{N}_0 \\ \dot{N}_1 \end{pmatrix} = \begin{pmatrix} h' & k \\ h & k' \end{pmatrix} \begin{pmatrix} N_0 \\ N_1 \end{pmatrix} \tag{4.3}$$

or simply, calling M the transition matrix,

$$\dot{\vec{N}} = M\vec{N} \tag{4.4}$$

with the initial conditions of the Cauchy problem $\vec{N}(0)$. Its solution can be expressed as

$$\vec{N}(t) = e^{tM}\vec{N}(0) = \Phi(t)\Phi(0)^{-1}\vec{N}(0) \tag{4.5}$$

with $\Phi(t)$ a solving matrix. Thus, in order to calculate e^{tM} we need to start from the eigenvalues τ of M:

$$\begin{aligned} \det(M - \tau\mathbb{I}) &= \det \begin{pmatrix} h' - \tau & k \\ h & k' - \tau \end{pmatrix} \\ &= (h' - \tau)(k' - \tau) - hk \\ &= \tau^2 - (h' + k')\tau + h'k' - hk \overset{!}{=} 0 \end{aligned} \tag{4.6}$$

The discriminant of such a quadratic equation is

$$\Delta = (h' - k')^2 + 4hk \tag{4.7}$$

and finally the determinant is equal to zero when

$$\tau_{12} = \frac{h' + k' \pm \sqrt{\Delta}}{2} \tag{4.8}$$

Notice that $\Delta > 0$ since the transition rates are $\in [0, +\infty)$ by definition, hence $\tau_{12} \in \mathbb{R}$. Finding the eigenvectors related to a generic eigenvalue τ:

$$\begin{pmatrix} h' - \tau & k \\ h & k' - \tau \end{pmatrix} \begin{pmatrix} p \\ q \end{pmatrix} = \begin{pmatrix} p(h' - \tau) + qk \\ ph + q(k' - \tau) \end{pmatrix} \overset{!}{=} \begin{pmatrix} 0 \\ 0 \end{pmatrix} \tag{4.9}$$

we obtain the following eigenspaces

$$\begin{cases} p = \frac{\tau - k'}{h} q \\ q \in \mathbb{R} \end{cases} \longrightarrow v_{12} = \begin{pmatrix} \frac{\tau_{12} - k'}{h} \\ 1 \end{pmatrix} \tag{4.10}$$

yielding

$$\varphi_{12}(t) \equiv v_{12}\, e^{\tau_{12}t} = \begin{pmatrix} \frac{\tau_{12} - k'}{h} e^{\tau_{12}t} \\ e^{\tau_{12}t} \end{pmatrix} \tag{4.11}$$

The solving matrix is then

$$\Phi(t) = \big(\varphi_1(t),\ \varphi_2(t)\big) = \begin{pmatrix} \frac{\tau_1 - k'}{h} e^{\tau_1 t} & \frac{\tau_2 - k'}{h} e^{\tau_2 t} \\ e^{\tau_1 t} & e^{\tau_2 t} \end{pmatrix} \tag{4.12}$$

from whom we have

$$\begin{aligned}
\Phi(0)^{-1} &= \begin{pmatrix} \frac{\tau_1 - k'}{h} & \frac{\tau_2 - k'}{h} \\ 1 & 1 \end{pmatrix}^{-1} \\
&= \Big(\frac{\tau_1 - k'}{h} - \frac{\tau_2 - k'}{h}\Big)^{-1} \begin{pmatrix} 1 & -\frac{\tau_2 - k'}{h} \\ -1 & \frac{\tau_1 - k'}{h} \end{pmatrix} \\
&= \frac{h}{\tau_1 - \tau_2} \begin{pmatrix} 1 & -\frac{\tau_2 - k'}{h} \\ -1 & \frac{\tau_1 - k'}{h} \end{pmatrix}
\end{aligned} \tag{4.13}$$

where we used the inversion formula for 2×2 matrices

$$\mathcal{A}^{-1} = \begin{pmatrix} \alpha_1 & \alpha_2 \\ \alpha_3 & \alpha_4 \end{pmatrix}^{-1} = \frac{1}{\det \mathcal{A}} \begin{pmatrix} \alpha_4 & -\alpha_2 \\ -\alpha_3 & \alpha_1 \end{pmatrix} \tag{4.14}$$

The solution of our Cauchy problem will be finally

$$\begin{aligned}
\begin{pmatrix} N_0(t) \\ N_1(t) \end{pmatrix} &= \begin{pmatrix} \frac{\tau_1 - k'}{h} e^{\tau_1 t} & \frac{\tau_2 - k'}{h} e^{\tau_2 t} \\ e^{\tau_1 t} & e^{\tau_2 t} \end{pmatrix} \frac{h}{\tau_1 - \tau_2} \begin{pmatrix} 1 & -\frac{\tau_2 - k'}{h} \\ -1 & \frac{\tau_1 - k'}{h} \end{pmatrix} \begin{pmatrix} N_{in} \\ 0 \end{pmatrix} \\[2mm]
&= N_{in} \frac{h}{\tau_1 - \tau_2} \begin{pmatrix} \frac{\tau_1 - k'}{h} e^{\tau_1 t} - \frac{\tau_2 - k'}{h} e^{\tau_2 t} \\ e^{\tau_1 t} - e^{\tau_2 t} \end{pmatrix}
\end{aligned} \tag{4.15}$$

that is, returning back to the system form,

$$\begin{cases} N_0(t) = N_{in}\Big(\frac{\tau_1 - k'}{\tau_1 - \tau_2} e^{\tau_1 t} - \frac{\tau_2 - k'}{\tau_1 - \tau_2} e^{\tau_2 t}\Big) \\[3mm] N_1(t) = N_{in} \frac{h}{\tau_1 - \tau_2}(e^{\tau_1 t} - e^{\tau_2 t}) \end{cases} \tag{4.16}$$

Note that $\tau_1 - \tau_2 > 0$ if at least one of the transition rates or the radioactive disintegration constant is not zero, which is a necessary condition for our system to make sense.

Now, let us analyze our solution. First of all, we may point out that the equation for $N_0(t)$ is practically useless at least to the current research, since we have not any interest in studying the activity in the whole body but an organ. So, our attention must be focused on $N_1(t)$; the eigenvalues of the transition matrix M, which now can be written in the extended form

$$M = \begin{pmatrix} -\lambda - h - l & k \\ h & -\lambda - k \end{pmatrix} \tag{4.17}$$

assume a fundamental role in the regulation of our biodistribution in a ROI. Looking at Eq. 4.8, we immediately realize that $\tau_2 < 0$ when the system makes physical sense, as all its addends are negative,
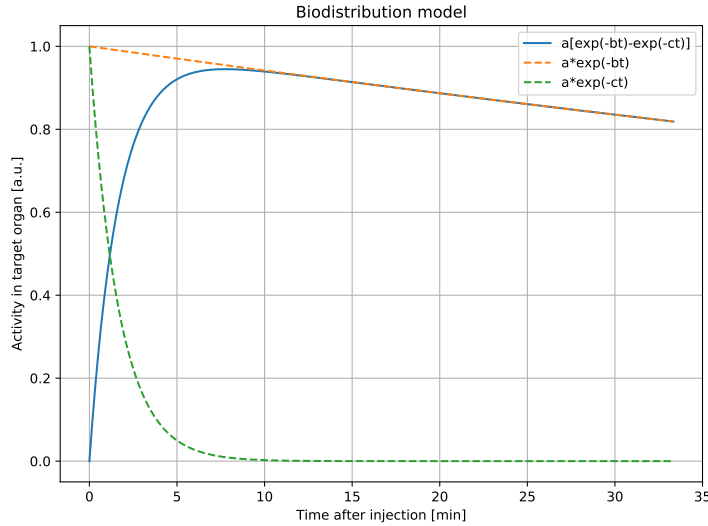
Figure 4.4: TRT-likely example of activity in a region of interest applying the biodistribution model; the dashed lines represent separately the two exponential contributions. Parameters setting: $a = 1$ in arbitrary units, $b = 0.0001$ s^{-1}, $c = 0.01$ s^{-1}.

thus the subtracted exponential is decreasing. What about τ_1? We should check its sign, for example investigating when $\tau_1 \geq 0$:

$$\tau_1 = \frac{h' + k' + \sqrt{(h' - k')^2 + 4hk}}{2} \overset{!}{\geq} 0 \tag{4.18}$$

We can erase the $1/2$ factor and subtract $h' + k'$ to both members, getting

$$\sqrt{(h' - k')^2 + 4hk} \geq -h' - k' \tag{4.19}$$

and, since the second member is always positive, we can square both members, obtaining

$$\cancel{h'^2} + \cancel{k'^2} - 2h'k' + 4hk \geq \cancel{h'^2} + \cancel{k'^2} + 2h'k' \tag{4.20}$$

and then

$$\cancel{4}(hk - h'k') \geq 0 \tag{4.21}$$

At this point, we had better expand h' and k':

$$\cancel{hk} - \lambda^2 - \lambda k - \lambda h - \cancel{hk} - kl \geq 0 \tag{4.22}$$

which is never true in the physical conditions of our system. In other words, we have just found out that $\tau_1 < 0$ as well: we can state that the law regulating the concentration of a radionuclide in a selected ROI is proportional to a difference between two negative exponentials with decaying constants τ_1 and τ_2, where $\tau_1 > \tau_2$, corresponding to the eigenvalues of the transition matrix M as defined before.

With a further step we can switch to activity by multiplying λ times, namely

$$A_1(t) = \lambda N_1(t) = \lambda N_{in} \frac{h}{\tau_1 - \tau_2}(e^{\tau_1 t} - e^{\tau_2 t}) \tag{4.23}$$

or equivalently, with a smarter notation,

$$A(t) = a(e^{-bt} - e^{-ct}) \tag{4.24}$$

where a is directly proportional to the TIA, $b = -\tau_1$ and $c = -\tau_2$. A representative graph of this situation is visible in Figure 4.4, where the initial conditions set were $a = 1$ in arbitrary units,

$b = 0.0001 \text{ s}^{-1}$ and $c = 0.01 \text{ s}^{-1}$. Such values of b and c were chosen in order to visualize a typical TRT trend. The blue curve illustrates the activity in the ROI: as expected, at $t = 0$ there is totally no radiopharmaceutical arrived yet, but its amount soon increases, reaches a maximum and slowly starts decaying; the dashed lines just show the two negative exponentials separately. This can lead to a few considerations: while the c exponential is strongly involved in the initial growth of the curve, the b contribution tends to approximate the decay for $t \to +\infty$; thus, a configuration with $b \ll c$ is desirable for a target organ. Anyway, it is more than a radioactive decay and in fact, if we analyze the coefficients in detail, we discover that

$$
\begin{aligned}
b = -\tau_1 &= -\frac{h' + k' + \sqrt{(h' - k')^2 + 4hk}}{2} \\
&= -\frac{-2\lambda - h - k - l + \sqrt{(\lambda + k - \lambda - h - l)^2 + 4hk}}{2} \\
&= \lambda + \frac{h + k + l - \sqrt{(k - h - l)^2 + 4hk}}{2} \\
&\equiv \lambda_{rad} + \lambda_{bio}
\end{aligned}
\tag{4.25}
$$

In conclusion, in such systems, the radioactive decay expressed by $\lambda \equiv \lambda_{rad}$ is combined with the so-called *biological decay*, modulated by this new constant λ_{bio} depending on the transition rates between the compartments and the elimination rate. Since $b = -\tau_1 > 0$ and λ_{rad} can be chosen arbitrarily small (actually up to $\lambda_{rad} = 0$ in the non-radioactive case), one can easily demonstrate that $\lambda_{bio} > 0$. An analogous argument can be applied to c, yielding $c \equiv \lambda_{rad} + \bar{\lambda}_{bio}$.

4.4 Dynamic imaging

Now, we can try to exploit our mathematical model for the biodistribution of a radiopharmaceutical. In particular, since dose calculation is our priority, we could assume that, together with activity, also the dose rate approximately follows a law of the kind

$$
\dot{D}(t) \sim a(e^{-bt} - e^{-ct})
\tag{4.26}
$$

with the parameters a, b and c maintaining the same properties as before: $a \propto$ TIA and $0 < b < c$. In fact, as we have seen with the MIRD schema, to a first approximation the largest contribution to the dose absorbed by a ROI is self-absorbed, although some events may penetrate from the external body and generate a cross-absorbed contribution; the latter would be anyway a surface effect in a volumetric context. If this assumption is fine and if we have several data to interpolate, then we will be able to compute the absorbed dose by integration over a period T

$$
\begin{aligned}
D(T) &= a \int_0^T (e^{-bt} - e^{-ct})\, dt \\[2mm]
&= a \left(\frac{e^{-bt}}{b} - \frac{e^{-ct}}{c} \right) \Bigg|_0^T \\[2mm]
&= a \left(\frac{e^{-bT} - 1}{b} - \frac{e^{-cT} - 1}{c} \right)
\end{aligned}
\tag{4.27}
$$

and when $T \to +\infty$, which is not an unlikely possibility considering that the radiopharmaceutical decays only physically and biologically and continues indefinitely, one finds the very simple formula

$$
D_\infty = a \left(\frac{1}{c} - \frac{1}{b} \right)
\tag{4.28}
$$

that will always be positive according to our restrictions for b and c. In order to apply this, we need at least two things:
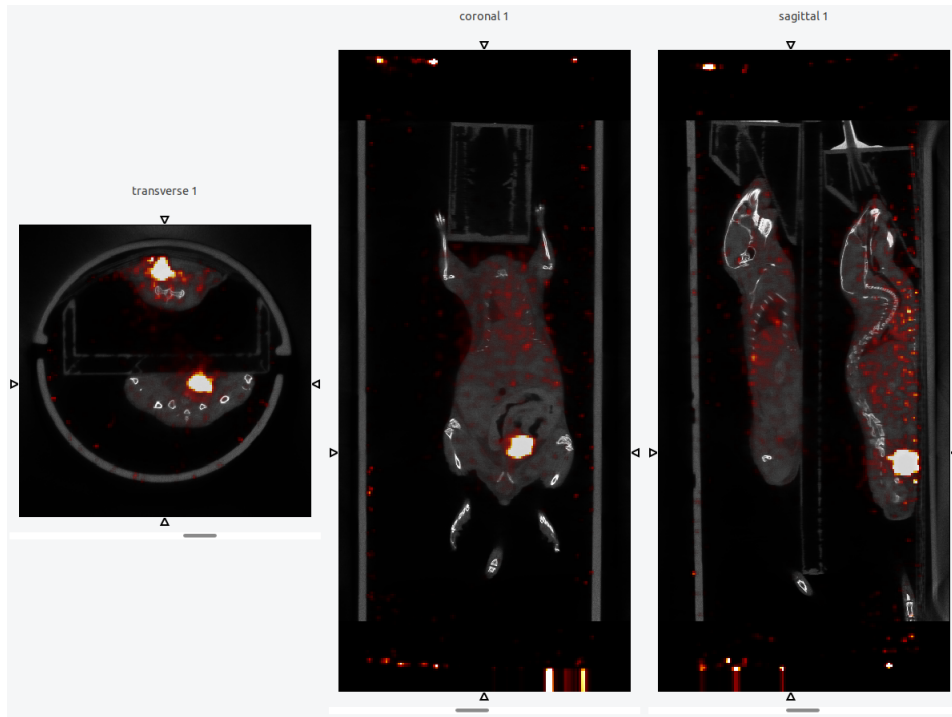
Figure 4.5: AMIDE representation of the activity distribution (arbitrary units) after 2 h from the injection of ^{111}In-IP-001 in two BIOEMTECH mice; the coronal plane shows the upper mouse, whereas the transverse section is upside down with respect to our dose maps.

- a series of PET or SPECT images at different moments after the injection;

- a higher precision in the tissue individuation to facilitate the dose calculation in a ROI.

This features will be achieved thanks to the supplementary material of a published study connected to the ISOLPHARM project. Such a research, identified as Verona et al., 2021 [44], had the aim of evaluating pre-clinically the reliability of a radiopharmaceutical containing ^{111}In and capable to bind the cholecystokinin-2 receptor (CCK-2R), overexpressed in the plasma membrane of several cancer cells and poorly expressed by healthy cells. The radionuclide is bound to a 1,5-benzodiazepine-derivative, forming the radiolabelled drug ^{111}In-IP-001. As we already know, such a radioisotope is suitable for SPECT imaging, and in fact we could count on a series of hybrid SPECT/CT images distributed in time provided by the Greek group BIOEMTECH [45], specialized in molecular imaging and collaborating with ISOLPHARM. Such data were acquired on a population of male adult mice with a tumour mass stimulated on their right shoulder.

From a morphological point of view, the new CT images have a higher resolution than the one used before — namely 0.2 mm versus 0.5 mm — and will allow a more precise definition of the borders between tissues; this will be illustrated in detail in the next paragraph, where certain organs will be selected and cut with different approaches. A better resolution implies a higher number of voxels, in our case $600 \times 350 \times 350$, that may put in trouble the volume construction in Geant4. For this reason, exploiting the fact that Geant4 can easily center both the volume and the source distribution in its proper reference frame, the CT images underwent some marginal cuts (obviously including only air and instrumentation) in order to lighten the occupation of computational memory.

Regarding the time distribution, a SPECT/CT study of two mice together — having the names of MX (upper mouse) and M16 (lower) — at 2, 4 and 8 h after the injection of ^{111}In-IP-001 was chosen. The resolution of the SPECT images was actually still 0.5 mm, for a total amount of $308 \times 125 \times 125$ (2 h) or $307 \times 125 \times 125$ (4 and 8 h) voxels, but this was not a problem as we decided to use a Direct Monte Carlo approach rather than a series of tissue-dependent convolutions. Also the SPECT images were cut at their farthest ends, because of the presence of a loud noise in activity despite the complete absence of any living tissue in those regions. Figure 4.5 shows a representation, obtained with the AMIDE toolkit [46], of the activity after 2 h from the intravenous injection of ^{111}In-IP-001;
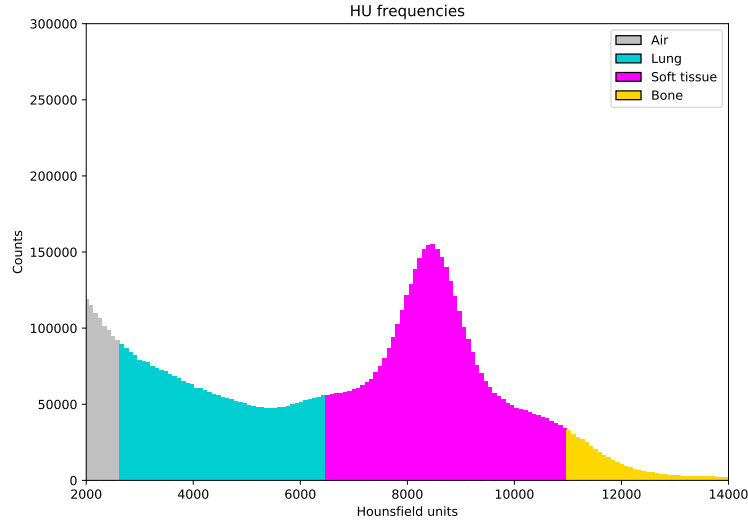
Figure 4.6: Histogram of the Hounsfield units frequencies for BIOEMTECH mice highlighting the most characteristic tissues.

Tissues	HU interval
Air	$[0, 4000]$
Lung	$[4000, 6000]$
Soft tissue	$[6000, 11000]$
Instrumentation	$[10000, 12000]$
Compact bone	$[11000, 65535]$

Table 4.2: Hounsfield units intervals corresponding to the main tissues in BIOEMTECH mice.

the SPECT noise, then removed on Geant4, is still visible in the coronal and sagittal planes. We note that this time the activity in the urinary bladder is way higher than in the rest of the mouse, and particular cancer regions do not emerge.

Using this SPECT/CT series combined to Direct Monte Carlo, a dosimetry study can be performed. We could begin with a calibration of the Hounsfied units, e.g. from the CT at 2 h, exactly like it was done in Chapter 3 with the imaging from LNS. This time, they stay in a completely different window, namely HU $\in [0, 65535]$; since from Eq. 1.20 we know that materials less dense than water, like air, should have HU < 0, a different scale was probably set in this CT apparatus. Furthermore, the values are distributed like in Figure 4.6, where two cuts were applied:

- to the air contribution, which is too big to be compared with the other tissues;

- to the bone tail, now including also teeth, that proceeds with sporadic counts until the maximum HU value, bringing visualization issues.

As before, the selection of the tissues, reported in Table 4.2, was accomplished by a patient work of visualization and assessment using highlighted pictures like Figures 4.8 and 4.7. Contrary to the previous CT, instrumentation revealed higher values, in complete superimposition with bone and soft tissue, probably due to the employment of denser materials. In these two figures, the organs appear much better defined than before; the compact bone interval represents in an excellent way the murine bones and teeth, whereas the lung window includes many border effects, but has the advantage to avoid the involvement of heart and blood vessels in the rib cage, as visible mostly in the transverse plane. As we anticipated, we will now adopt the MOBY definition of lung, hence expecting higher dose rates in that ROI due to the lower density assumed. Anyway, we now have better instruments than before and it would be a shame not to try a more precise attribution of the tissues to the virtual phantom; the next paragraph will show what could be done.
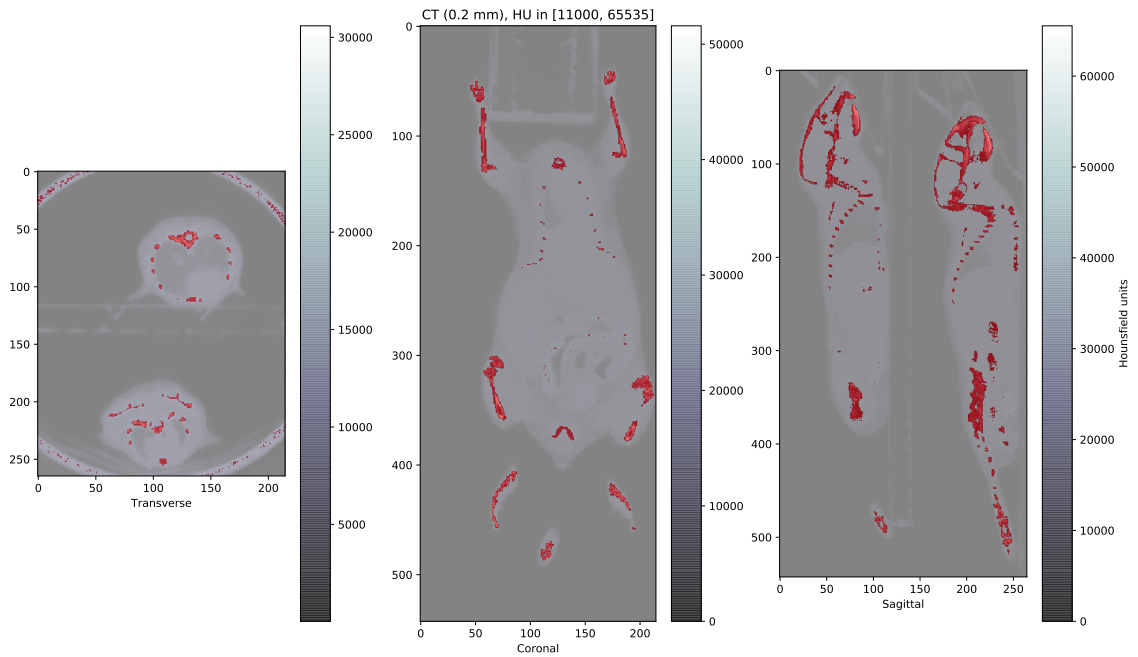
Figure 4.7: CT with the window HU ∈ [11000, 65535], supposed to host bone, highlighted in red.

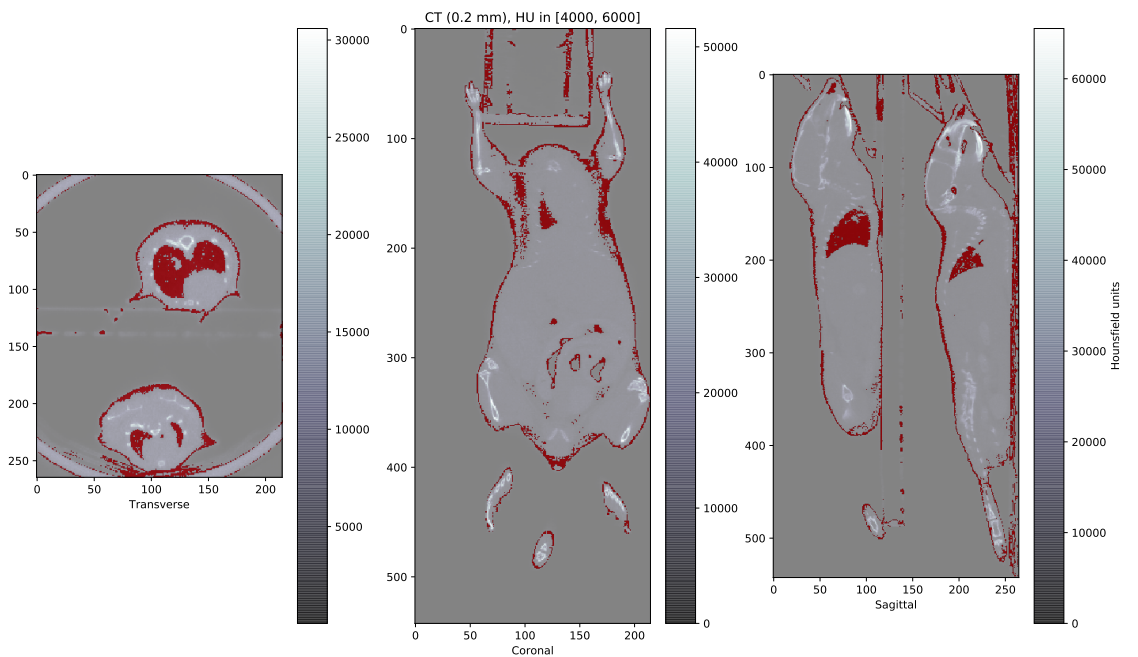Figure 4.8: CT with the window HU ∈ [4000, 6000], supposed to host the lungs, highlighted in red.

Figure 4.9: A frame from the lungs selection of mouse M16 using ImageJ.

4.4.1 Organ selection

Our current goal is to compute the absorbed dose in a time interval T by a ROI, but the results of this paragraph will also allow us to perform a better Direct Monte Carlo simulation in general. In fact, what we are going to do is selecting specific organs — remember that knowing the dose absorbed by the healthy tissues is as important as the one absorbed by the cancer — in order to:

- assign them the correct tissue, avoiding to put it in wrong places;

- have a direct access to those organs when calculating the dose rate.

Unfortunately, the presence of organs with way different shapes, reciprocal positions and compositions makes it very difficult to develop a common procedure to do it. For this reason, we will focus on two organs which are considered representative of two different situations:

- the lungs will be the pilot case for organs of whatever shape identified by a specific HU window which is in partial or total overlap with other tissues;

- the brain will represent instead organs whose borders are well-defined by a discontinuity in the Hounsfield units, which in this case corresponds to the compact bone of the skull.

Starting from the lungs, the work to do is simpler and in our case it is strongly needed also at the beginning of the simulation, in order to delete the border effects visible in Figure 4.8. The strategy is to consider a pile of cylinders with a common[2] rotation axis parallel to the coronal plane; such cylinders together have to contain the lungs and leave out all the rest that has the same HU, in this case the border effects. For other organs, different solid figures may be used for sure. This operation takes some time since the CT must be carefully analyzed by means of DICOM readers like ImageJ [47]

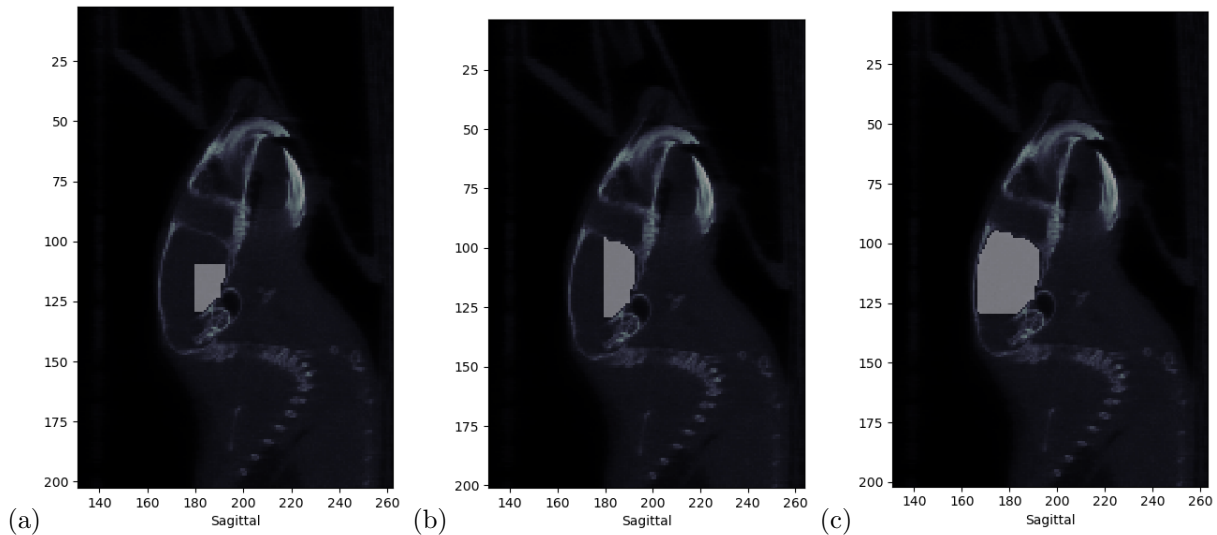[2]This is useful but not compulsory.

Figure 4.10: 2D frames from the brain selection of mouse M16 in the sagittal xy plane: (a) growth along positive x and y directions from the seed, (b) negative x added and (c) negative y added.

or AMIDE itself. An example using the former software is displayed in Figure 4.9; supposing that in our reference frame the transverse section corresponds to the yz plane, one has to identify

- the coordinates of the rotation axis (y_0, z_0);

- the interval $[x_1, x_2]$ containing each cylinder;

- the radius $r = \sqrt{(y - y_0)^2 + (z - z_0)^2}$.

When one knows these values (in terms of either voxels or mm), Geant4 can be told to assign the lung tissue to voxels presenting $HU \in [4000, 6000]$ and included in one of the defined cylinders. The border effects get drastically reduced and the lungs can be successfully cut when computing the dose rate, too.

A completely different situation occurs when analyzing the brain. In our simulations it is assimilated to the generic soft tissue, so no further actions have to be done during that step, but the following technique could be helpful if one considered brain as a stand-alone tissue. The computational problem we want to solve is the dose rate calculation in our ROI from the total map, therefore we need to access to the single brain voxels, without leaving the organ, and sum their values. To do so, the following method was developed.

1. A starting brain voxel, which can be called *seed*, is selected.

2. Using a composition of *while* cycles, the selection moves along the three directions (both positive and negative side) until it reaches the HU discontinuity.

3. If the container tissue presents some holes, a geometric limit must be set to prevent the selection from leaving the ROI.

As an example of instruction 3., the discontinuity between brain and cerebellum is not appreciable with our CT, so a manual border along the x axis must be set. It is clear that the choice of the *seed* is not fully arbitrary, since if the selection along a direction meets a border too early, a part of the organ might not be reached at all. Figure 4.10 shows a sequence of the brain voxels selection of mouse M16, in the sagittal xy plane. A straight border is visible in the lower part: as anticipated, in absence of skull on that side, the discontinuity between brain and cerebellum had to be drawn manually.

Finally, dealing with the cost of computational time of the two methods introduced, no significant worsening is registered when calculating the dose rate in lungs, while a small increase happens with brain, anyway remaining in the acceptable order of magnitude of a few seconds with our devices.
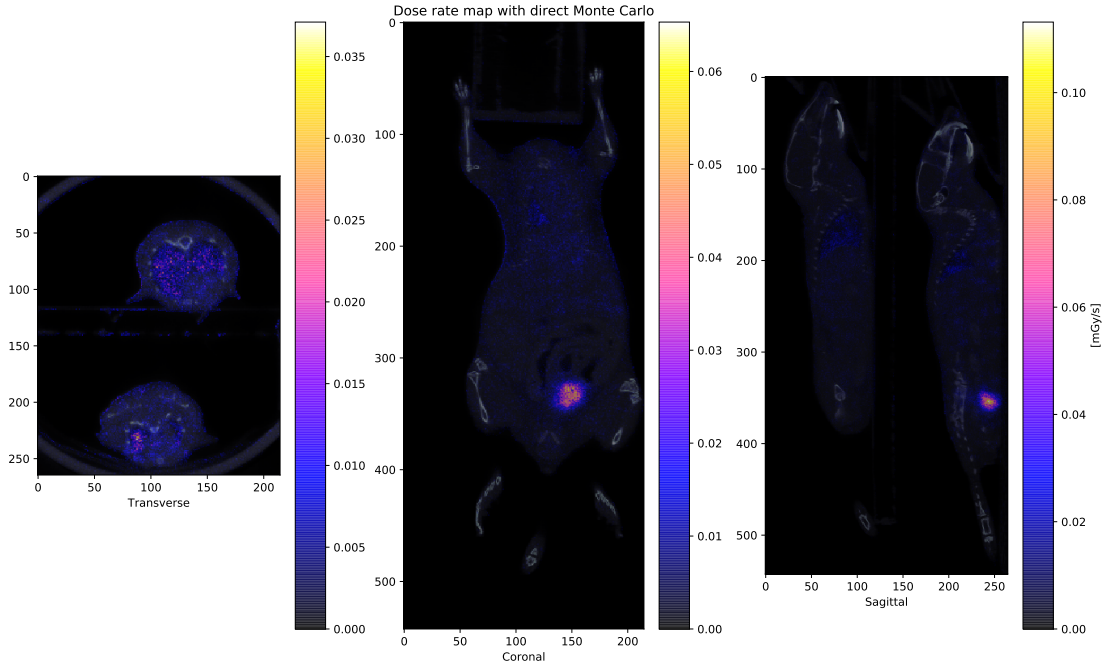
Figure 4.11: Dose rate map of BIOEMTECH mice computed by Direct Monte Carlo with ^{111}In in the air-soft-bone-lung approximation after 2 h from a 7.40 MBq injection; the coronal plane shows the upper mouse.

4.4.2 Absorbed dose calculation

We are now ready to proceed with the Direct Monte Carlo simulations and compute the dose rate, applying the organ selection for lungs and brain as explained in the previous paragraph to the whole series of murine CTs. As the activity in each image was expressed in arbitrary units, a TIA of 7.40 MBq was considered for each mouse as reported in Verona et al., 2021; letting it decay exponentially for 2 h with the proper λ of ^{111}In ($t_{1/2} = 2.8047$ d), 7.25 MBq were obtained and the same number of events was simulated to get the dose per second, in the rough assumption that the mice did not urinate during the first 120 min.[3] Alternatively, an arbitrarily high number of events can also be run and later normalized. A calibration factor was obtained for each mouse dividing 7.25 MBq by its total activity expressed by the SPECT counts at 2 h. Letting ^{111}In decay until 4 and 8 h, one obtains respectively 7.10 MBq and 6.81 MBq, but applying the calibration factors to the new SPECT counts it turned out that

- at 4 h both mice had about 6.27 MBq, so 0.83 MBq could be considered expelled by urination;

- at 8 h MX had 4.14 MBq and M16 had 3.64 MBq, meaning different multiple expulsions.

The dose rate maps for the whole time distribution are illustrated in Figures 4.11, 4.12 and 4.13, and some considerations may be made. A higher dose rate is reached in lungs without appreciable border effects, as visible mostly — but not only — in the transverse sections, meaning that our strategy to set the MOBY definition of lung tissue and isolate such organs during the HU assignment is working. Anyway, some thickened border lines are visible also far from the rib cage, probably due to the noise that implied the presence of decay events occurring in air and arriving to the mouse's external surface. This observation is corroborated by the deposition of a certain amount of dose on the instrumentation; moreover, a suspicious noisy pattern appears near the belly of the lower mouse, M16.
Now, Geant4 allows the user to switch the selected radionuclide and associate a different one to the ^{111}In-IP-001 biodistribution. Since ISOLPHARM is mainly interested in the behavior of ^{111}Ag and it

---

[3]Such data were unfortunately missing.

Figure 4.12: Dose rate map of BIOEMTECH mice computed by Direct Monte Carlo with ^{111}In in the air-soft-bone-lung approximation after 4 h from a 7.40 MBq injection; the coronal plane shows the upper mouse.
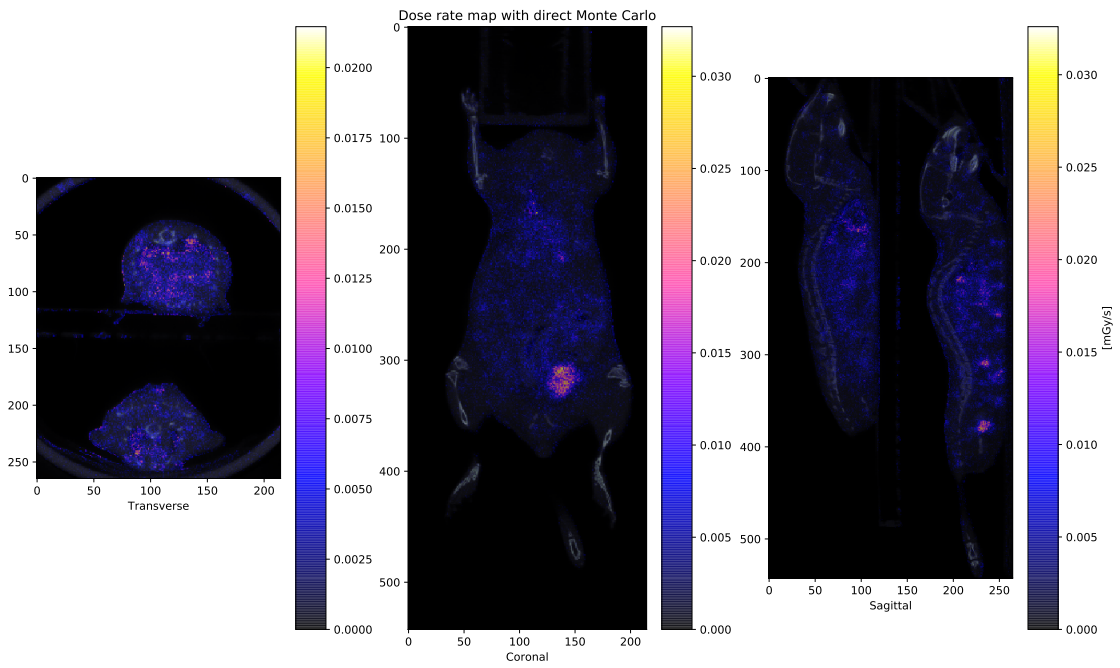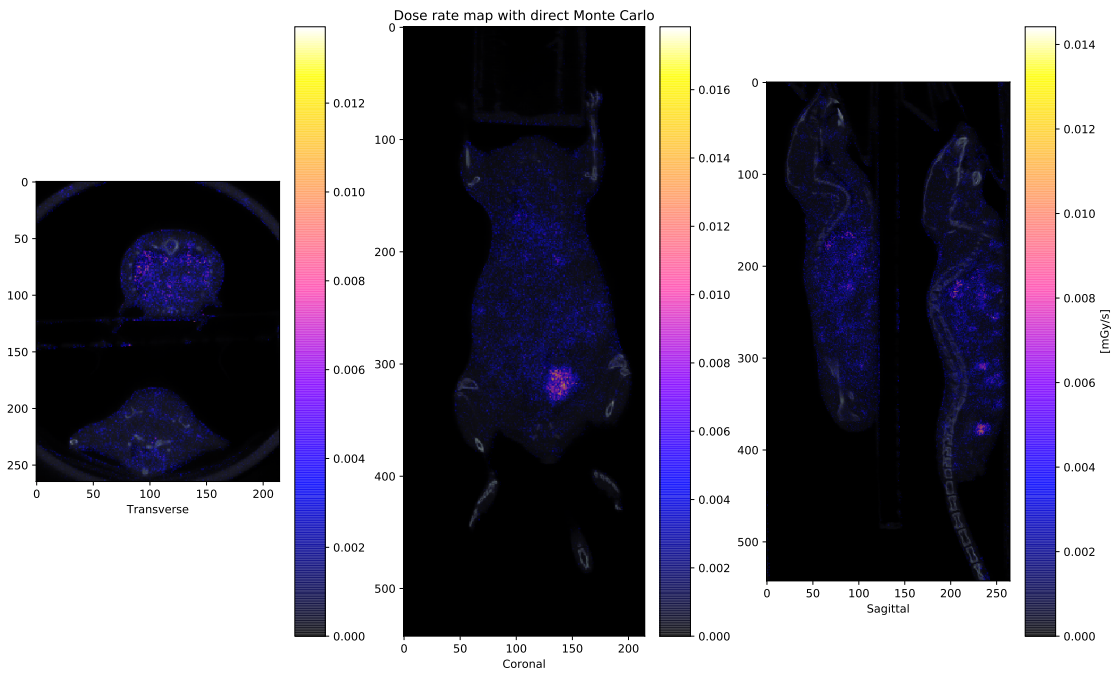

Figure 4.13: Dose rate map of BIOEMTECH mice computed by Direct Monte Carlo with ^{111}In in the air-soft-bone-lung approximation after 8 h from a 7.40 MBq injection; the coronal plane shows the upper mouse.
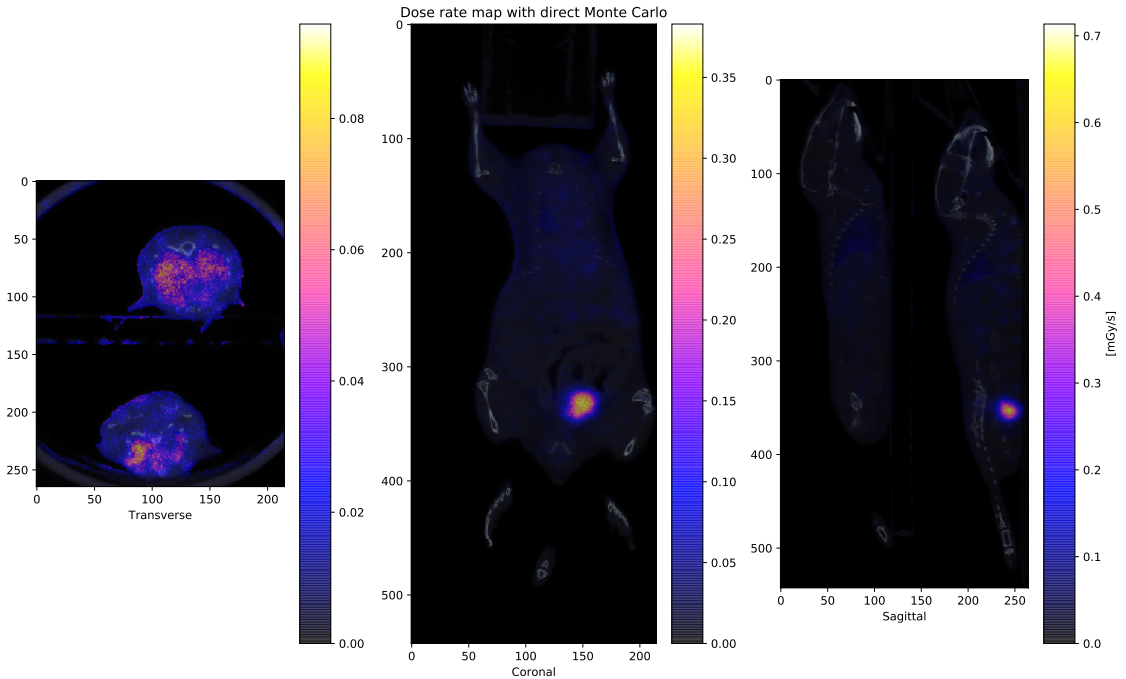
Figure 4.14: Dose rate map of BIOEMTECH mice computed by Direct Monte Carlo with ^{111}Ag in the air-soft-bone-lung approximation with 7.25 MBq 2 h after the injection; the coronal plane shows the upper mouse.

is not unlikely that such a drug could be radiolabelled with the silver isobar as well, bringing a similar distribution, we can change and insert it. Naturally, we expect a pretty higher short range dose due to the β^- emission; the same activity may be kept at the injection (or in a single frame), recalling that now the population has changed its decay rate, but a configuration with the same number of nuclides — i.e. the same quantity of radiopharmaceutical — is also reproducible by adding a factor which represents the ratio between the two half-lives. Remember that $t_{1/2} = 7.45$ d for ^{111}Ag, so identifying the number of nuclides (activity) would imply a lower activity (higher number of nuclides). For instance, Figure 4.14 shows the result of such a substitution maintaining an activity of 7.25 MBq after 2 h from the injection.

Of course such a modality of visualization is a little disturbed by the troublesome presence of the highly radioactive urinary bladders, mainly in the pictures at 2 h. However, with the help of the instruments developed for the organ selection, we are now able to distinguish separately either lungs or brain and check the time evolution of their dose rate. Due to the lack of points close to the injection time, only an approximate interpolation exploiting the condition $b \ll c$, hence neglecting the subtracted exponential in Eq. 4.26 (see also again Figure 4.4), could be carried out, using the function

$$\dot{D}(t) \approx a\,e^{-bt} \tag{4.29}$$

whose integral over $[0, T]$ yields the absorbed dose

$$D(T) = a\frac{1 - e^{-bT}}{b} \tag{4.30}$$

and, in the $T \to +\infty$ limit,

$$D_\infty = \frac{a}{b} \tag{4.31}$$

The plots for ^{111}In in lungs and brain of both mice are shown in Figure 4.15, whereas Table 4.3 illustrates the fit parameters a and b, the dose integral D_∞ and $\lambda_{bio} = b - \lambda_{rad}$. Dose rates appear
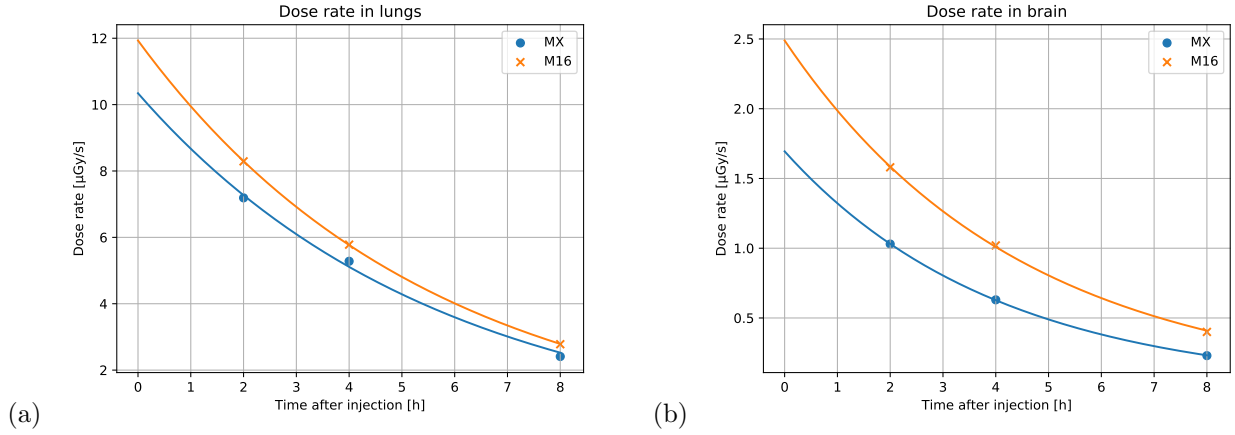
(a)   (b)

Figure 4.15: Dose rate of mice MX and M16 in (a) lungs and (b) brain at 2, 4 and 8 h after the ^{111}In injection with exponential fit.

Organ	a [μGy/s]	b [s^{-1}]	D_∞ [mGy]	λ_{bio} [s^{-1}]
Lungs MX	10.34	$4.90 \cdot 10^{-5}$	211	$4.61 \cdot 10^{-5}$
Lungs M16	11.93	$5.05 \cdot 10^{-5}$	236	$4.76 \cdot 10^{-5}$
Brain MX	1.69	$6.90 \cdot 10^{-5}$	25	$6.61 \cdot 10^{-5}$
Brain M16	2.49	$6.27 \cdot 10^{-5}$	40	$5.98 \cdot 10^{-5}$

Table 4.3: Exponential fit parameters, absorbed dose integral and λ_{bio} for BIOEMTECH mice in lungs and brain with ^{111}In-IP-001.

lower now due to the division by the organ volume V, namely:

$$\dot{D}_{organ} = \frac{E_{organ}}{\rho V} = \frac{v}{V} \frac{\sum E_{voxel}}{\rho v} = \frac{1}{n} \sum \dot{D}_{voxel} \tag{4.32}$$

where voxel volume v and organ density ρ are constant and $n \equiv V/v$ is the number of voxels composing the organ. Recall anyway that these values represent a demonstrative toy-model and should not be taken as likely estimates, because of:

- the coarse assumption of no urination within the first 120 min we were forced to adopt;

- the fact that repeated CTs required different masks for the same organ;

- the radiation produced by noise from outside the mice;

- the fact that we neglected the c exponential since our SPECTs were taken long after the injection, so that we did not consider at all the organ uptake phase.

Regarding the difference between the two mice, brain has a worse agreement than lungs, meaning that its cutting algorithm can still be improved. More reliable results would be obtained by using a longer and closer to injection SPECT or PET series with anesthetized mice, as done for instance by Gupta et al., 2019: in this way, the urination issue could be controlled and a single CT could be used. However, our absorbed dose values seem to belong to the same order of magnitude as the ones found in the cited reference study, where hundreds of mGy were obtained simulating a 15.22 MBq injection of [18]F — more energetic and radioactive than [111]In — in a murine population.

Having this data, we could further exploit our toy-model to show how one can estimate the dose released by another radiolabelling of the same pharmaceutical. Let us call λ_{Ag} the disintegration constant of [111]Ag and suppose to have 7.25 MBq of it at time $t = 2$ h, like in Figure 4.14. The new exponential parameters would become

$$b' = \lambda_{Ag} + \lambda_{bio} \tag{4.33}$$
$$c' = \lambda_{Ag} + \bar{\lambda}_{bio} \tag{4.34}$$

Organ	$\dot{D}(2\,\mathrm{h})$ [μGy/s]	b' [s^{-1}]	a' [μGy/s]	D_∞ [mGy]
Lungs MX	39.70	$5.01 \cdot 10^{-5}$	56.94	1137
Lungs M16	46.19	$5.16 \cdot 10^{-5}$	66.97	1298
Brain MX	5.15	$7.01 \cdot 10^{-5}$	8.53	122
Brain M16	7.98	$6.38 \cdot 10^{-5}$	12.63	198

Table 4.4: Exponential parameters and absorbed dose integral for BIOEMTECH mice in lungs and brain with a hypothetical radiopharmaceutical labelled with ^{111}Ag following the biodistribution of ^{111}In-IP-001, calibrated on 7.25 MBq at 2 h.

although, obviously, c' will be missing; a' could instead be extracted, applying the ROI cuts to the dose rate map of Figure 4.14, from Eq. 4.29:

$$a' = \frac{\dot{D}(t)}{e^{-b't}} \tag{4.35}$$

The results for the silver isobar are summarized in Table 4.4; as expected, $\dot{D}_\infty$ shows higher values due to the β^- emission of ^{111}Ag. Remember that, though we previously chose to calibrate the new radionuclide with 7.25 MBq after 2 h from the injection, one could also fix a particular value of TIA: therefore, this mechanism could become a useful instrument to estimate the absorbed dose in future pre-clinical experiments.

Conclusions

The main purpose of this master thesis was to develop different methods of computed dosimetry for nuclear medicine in the context of the ISOLPHARM project (INFN-LNL), by means of instruments including Monte Carlo codes (mainly Geant4) and PET/CT or SPECT/CT imaging. After an introductory part that provided some basic information about the underlying concepts of medical physics and ISOLPHARM in general, Chapter 3 followed the dosimetric procedure developed by the MIRD. This technique is based on a convolution between a 3D function expressing the activity distribution in the patient — namely a PET or a SPECT — and a 3D kernel whose coefficients reflect the effectiveness of a radiation source in a tissue. Such a kernel could be built simulating multiple decay events on Geant4 in virtual volumes of several tissues, subdivided in either concentric shells (DPK coefficients) or voxels (VSV). A database containing DPKs and VSVs of the main radionuclides of medical interest for ISOLPHARM was produced and, when possible, compared with literature. Furthermore, the energy deposition of the sources was evaluated: in particular, it turned out that ^{111}Ag, the most promising and innovative radioisotope of the project, behaves similarly to the theranostic nuclide ^{177}Lu, thus a future use in nuclear medicine of this silver isotope can be hypothesized.

Once the database was completed, some examples of convolution were given using a PET/CT hybrid pre-clinical imaging carried out at INFN-LNS with ^{18}F-FDG. The related VSVs were utilized to compute the dose rate map in a murine phantom

- in the 100% soft tissue approximation;

- in the three tissues approximation, involving compact bone, lung and soft tissue, which was possible thanks to the morphological information contained by the CT.

Moreover, the former map was compared to an equivalent one drawn using DPKs; the resulting dose rate distribution was less peaked on the sources, probably because, contrary to the small DPK core, the size of the source voxel was comparable to the mean range in water of the e$^+$ emitted by ^{18}F. It is important to underline that the construction of the dataset was computationally time-expensive, but then the convolutions took a negligible time.

Subsequently, Chapter 4 began with the exposition of another computed dosimetry method, which was named Direct Monte Carlo: indeed, it consists in a complete simulation of the decay events suggested by an emission tomography in the Geant4 virtual reproduction of a CT, where the dose rate is counted in every voxel. This strategy was tried on the same LNS mouse and a comparison with the MIRD schema results was made. Direct Monte Carlo is more time-expensive but it is also expected to be more precise: in this assumption we noticed that, when using more than one tissue, some discrepancies occur near the borders. Our explanation was that the MIRD schema neglected the dose rate contributions at long range and, mostly, the cross-absorbed dose passing through the discontinuities between tissues.

In the second half of Chapter 4, a theoretical model for the biodistribution of the activity in regions of interest was introduced and later applied to a dynamic SPECT/CT pre-clinical imaging. The mathematical formalization of the problem showed that the activity decrease in an organ is modulated by the the radioactive disintegration constant, λ_{rad}, together with a biological decay constant, λ_{bio}. The sum of such constants is related to the eigenvalues of the Markov transition matrix of the body-organ system, including radioactive decay and physiological elimination of the radiopharmaceutical. The dynamical imaging was provided by the BIOEMTECH group and allowed us to study three subsequent SPECT/CTs of two mice after an injection of ^{111}In-IP-001. Exploiting the higher resolution of those

CTs, two methods to select specific organs from a 3D map were developed. Using all these tools, it was possible to calculate the absorbed dose by integration over a period; the reconstructed dose rate curves were approximated due to the long time distance from the injection of our SPECTs, however the results for ^{111}In appeared compatible with the reference literature. Finally, since it is thought that future radiopharmaceuticals labelled with ^{111}Ag may follow the same biodistribution, the method was extended to predict a hypothetical pre-clinical experiment with this nuclide.

We can conclude by pointing out some possible future steps of this research in the ISOLPHARM project. First, Direct Monte Carlo appeared to have an appropriate CPU timing for pre-clinical studies, but it could be interesting to exploit the MIRD schema toghether with the former to investigate the contribution of cross-absorbed dose in addition to self-absorbed dose. Moreover, further simulations based on dynamic imaging taken at short times after the injection would allow to improve the theoretical characterization of the biodistribution and to have more reliable predictions for future pre-clinical experiments. Finally, trying to automatize the selection process of all the murine and human organs from a CT could be an engaging challenge.

Appendix A

Radioactive source DPK This appendix shows Geant4 DPK curves in water for radioactive sources not present in our literature of reference: ^{18}F (100% pure β^+-emitter), ^{64}Cu (β^+, β^- and γ) and ^{89}Sr (pure β^-).
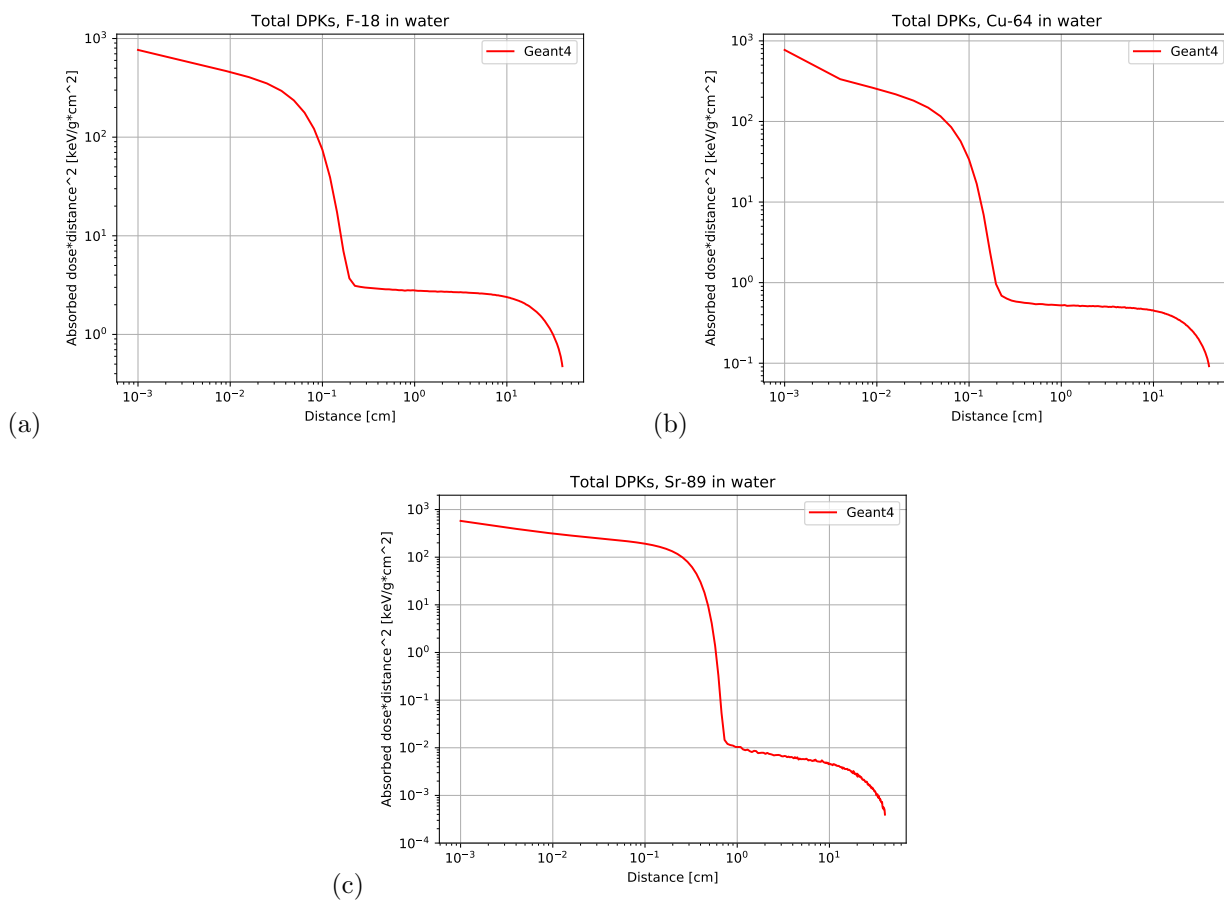

(a)

(b)

(c)

Figure A.1: DPK curves of (a) ^{18}F, (b) ^{64}Cu and (c) ^{89}Sr in water using Geant4 with 10^7 events.

Appendix B

Convolution of subsequent decays The current paragraph will formalize a simple model for the convolution of sources decaying twice with different half-lives, following the MIRD schema; the example of technetium will be used, but the conclusion will be absolutely general. In radioactivity and nuclear physics, a couple of mother and daughter nuclei like ^{99m}Tc and ^{99}Tc g.s. can be classified in the *non-equilibrium* condition since $t^m_{1/2} < t^g_{1/2}$; solving Bateman's differential equations for the number N of metastable and g.s. nuclei [15] [16]

$$\begin{cases} \dot{N}_m(t) = -\lambda_m N_m(t) \\ \dot{N}_g(t) = \lambda_m N_m(t) - \lambda_g N_g(t) \end{cases}$$

we obtain

$$\begin{cases} N_m(t) = N_{0m}\, e^{-\lambda_m t} \\ N_g(t) = \lambda_m N_{0m} \frac{e^{-\lambda_m t} - e^{-\lambda_g t}}{\lambda_g - \lambda_m} + N_{0g}\, e^{-\lambda_g t} \end{cases}$$

where λ and N_0 indicate the radioactive disintegration constants and the initial quantities of nuclides. The resulting trend is illustrated in Figure B.1(a), where the g.s. curve seems like it is not decaying because of its very long half-life. Recall that, as we said in Section 1.1, the activity of a population of radionuclides $A(t)$ is trivially connected to $N(t)$ by Eq. 1.4. Now, let us suppose to have two different VSV kernels S_m and S_g for the two nuclides, like in Figure B.1(b); in fact, with Geant4 it is possible to compute

- S_m by placing ^{99m}Tc as radioactive source and killing all the ^{99}Tc g.s. ions as soon as they are produced;

- S_g by using directly ^{99}Tc as source.

Regarding the activity, which could be realistically taken from a SPECT, it would be referred to ^{99m}Tc, namely $A_m(t) = \lambda_m N_m(t)$. In order to calculate $A_g(t)$, it is fundamental to know the initial ratio N_{0g}/N_{0m} at the production of the radiopharmaceutical or at the injection moment. If this happens,
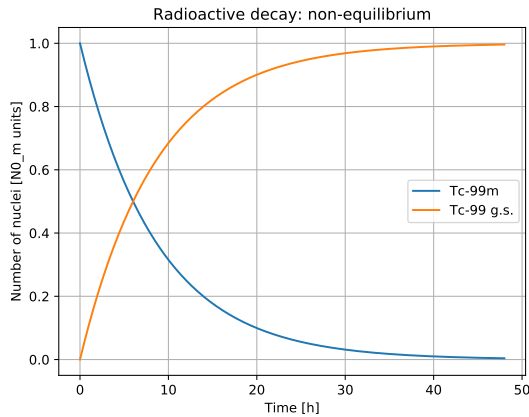
(a)
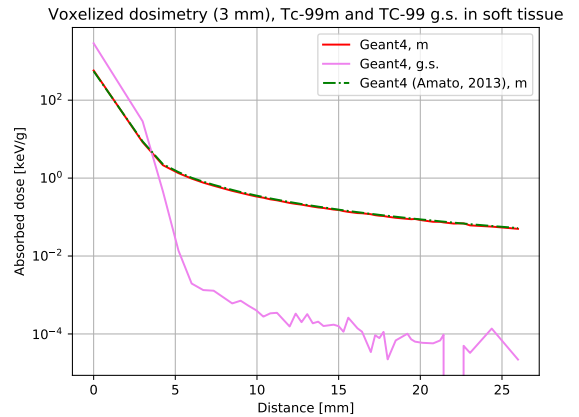
(b)

Figure B.1: (a) Decay curves of a ^{99m}Tc and ^{99}Tc population assuming $N_{0g} = 0$. (b) VSV curves of ^{99m}Tc, compared with Amato et al., 2013, and ^{99}Tc in soft tissue using Geant4.

one can find N_{0m} from Bateman's equations (if it is not known itself) using an appropriate value for t, calculate N_{0g} and then $A_g(t) = \lambda_g N_g(t)$. Therefore, the total dose rate in the MIRD formalism will result

$$\dot{D}(r_t, t) = \sum_s A_m(r_s, t)\, S_m(r_t \leftarrow r_s) + A_g(r_s, t)\, S_g(r_t \leftarrow r_s)$$

Having a series of subsequent SPECT each activity could obviously be integrated, yielding the absorbed dose in a time window. These considerations can be extended to a generic medical radioisotope whose daughter nucleus decays again once or even more times.

Bibliography

[1] https://isolpharm.pd.infn.it/web/ (consulted: July 2021).

[2] https://geant4.web.cern.ch/node/1 (consulted: July 2021).

[3] J. Valentin, *ICRP Publication 103 – The 2007 Recommendations of the International Commission on Radiological Protection*, Annals of the ICRP (Vol. 37), 2007.

[4] D. L. Bailey et al., *Nuclear Medicine Physics*, IAEA, 2014.

[5] E. J. Hall, A. J. Giaccia, *Radiobiology for the Radiologist*, Wolters Kluwer – Lippincott Williams & Wilkins, 2012.

[6] M. Goitein, *Trials and tribulations in charged particle radiotherapy*, Radiotherapy and Oncology Vol. 95, 2010, pp, 23–31.

[7] E. B. Podgorsak, *Radiation Oncology Physics*, IAEA, 2005.

[8] S. Aghevlian et al., *Radioimmunotherapy of cancer with high linear energy transfer (LET) radiation delivered by radionuclides emitting α-particles or Auger electrons*, Advanced Drug Delivery Reviews Vol. 109, 2017, pp. 102-118.

[9] S. Webb, *The Physics of Medical Imaging*, Taylor & Francis Group LLC, 1988.

[10] https://www.researchgate.net/figure/Graphical-representation-of-the-anatomical-planes-that-divides-the-body-Mrabet-2008-The_fig1_221927468 (consulted: August 2021).

[11] https://commons.wikimedia.org/wiki/File:Tomographic_fig1.png (consulted: August 2021).

[12] https://www-nds.iaea.org/ (consulted: August 2021).

[13] F. Borgna, A. Andrighetto et al., *A preliminary study for the production of high specific activity radionuclides for nuclear medicine obtained with the isotope separation on line technique*, Applied Radiation and Isotopes, 2017, pp. 214-226.

[14] M. Ballan, *Development of targets for the production of radionuclides of medical interest according to the ISOL technique*, PhD Thesis – Università degli Studi di Ferrara, 2018.

[15] A. Arzenton, *Study of the activity of radionuclides produced in the SPES-ISOLPHARM target*, Bachelor Degree Thesis – Università degli Studi di Padova, 2019.

[16] H. Bateman, *The solution of a system of differential equations occurring in the theory of radioactive transformations*, Proceedings of the Cambridge Philosophical Society Vol. 15, 1910, pp. 423–427.

[17] W. E. Bolch et al., *MIRD Pamphlet No. 21: A Generalized Schema for Radiopharmaceutical Dosimetry – Standardization of Nomenclature*, The Journal of Nuclear Medicine Vol. 50 No. 3, 2009, pp. 477-484.

[18] F. Botta et al., *Calculation of electron and isotopes dose point kernels with FLUKA Monte Carlo code for dosimetry in nuclear medicine therapy*, Medical Physics Vol. 38 No. 7, 2011, pp. 3944-3954.

[19] http://www.fluka.org/fluka.php (consulted: August 2021).

[20] https://www.python.org/ (consulted: August 2021).

[21] https://physics.nist.gov/PhysRefData/Star/Text/ESTAR.html (consulted: August 2021).

[22] P. Papadimitroulas et al., *A dose point kernel database using GATE Monte Carlo simulation toolkit for nuclear medicine applications: Comparison with other Monte Carlo codes*, Medical Physics Vol. 39 No. 8, 2012, pp. 5238-5247.

[23] S. A. Graves et al., *Dose point kernels for 2,174 radionuclides*, Medical Physics Vol. 46 No. 11, 2019, pp. 5284-5293.

[24] http://www.opengatecollaboration.org/ (consulted: August 2021).

[25] https://mcnp.lanl.gov/ (consulted: August 2021).

[26] B. M. Mendes et al., *Calculation of dose point kernel values for monoenergetic electrons and beta emitting radionuclides: Intercomparison of Monte Carlo codes*, Radiation Physics and Chemistry Vol. 181, 2021.

[27] https://commons.wikimedia.org/wiki/File:Iodine-131-decay-scheme-simplified.svg (consulted: August 2021).

[28] R. R. do Nascimento et al., *Metal coordination study at Ag and Cd sites in crown thioether complexes through DFT calculations and hyperfine parameters*, Journal of Molecular Modeling Vol. 21 No. 97, 2015.

[29] N. Lanconelli et al., *A free database of radionuclide voxel S values for the dosimetry of nonuniform activity distributions*, Physics in Medicine and Biology Vol. 57, 2012, pp. 517-533.

[30] E. Amato et al., *Monte Carlo study of voxel S factor dependence on tissue density and atomic composition*, Nuclear Instruments and Methods in Physics Research A Vol. 279, 2013, pp. 870-876.

[31] I. Kawrakow, B. R. B. Walters, *Efficient photon beam dose calculations using DOSXYZnrc with BEAMnrc*, Medical Physics Vol. 33, pp. 3046-3056.

[32] M. Pacilio et al., *Differences among Monte Carlo codes in the calculations of voxel S values for radionuclide targeted therapy and analysis of their impact on absorbed dose evaluations*, Medical Physics Vol. 36 No. 5, 2009, pp. 1543-1552.

[33] M. S. Lee et al., *Whole-body voxel-based personalized dosimetry: the multiple voxel S-value approach for heterogeneous media with nonuniform activity distributions*, The Journal of Nuclear Medicine Vol. 59, 2018, pp. 1133-1139.

[34] T. Das, S. Banerjee, *Theranostic Applications of Lutetium-177 in Radionuclide Therapy*, Current Radiopharmaceuticals Vol. 9, 2016, pp. 94-101.

[35] G. Sgouros et al., *Radiopharmaceutical therapy in cancer: clinical advances and challenges*, Nature Reviews – Drug Discovery Vol. 19, September 2020, pp. 589-608.

[36] A. Gupta et al., *Preclinical voxel-based dosimetry through GATE Monte Carlo simulation using PET/CT imaging of mice*, Physics in Medicine and Biology Vol. 64 No. 095007, 2019.

[37] D. Pistone et al., *Monte Carlo based dose-rate assessment in ^{18}F-choline PET examination: a comparison between GATE and GAMOS codes*, Atti della Accademia Peloritana dei Pericolanti – Classe di Scienze Fisiche, Matematiche e Naturali Vol. 98 No. 1 A5, 2020.

[38] https://root.cern/ (consulted: August 2021).

[39] https://www.icru.org/ (consulted: August 2021).

[40] https://www.hopkinsmedicine.org/radiology/research/divisions/radiological-physics/research/projects/imaging-simulation-computer-phantoms.html (consulted: August 2021).

[41] O. N. Shevtsova, V. K. Shevtsova, *Mathematical Simulation of Transport Kinetics of Tumor-Imaging Radiopharmaceutical ^{99m}Tc-MIBI*, Hindawi – Computational and Mathematical Methods in Medicine No. 2414878, 2017.

[42] T. Sato et al., *Individual dosimetry system for targeted alpha therapy based on PHITS coupled with microdosimetric kinetic model*, EJNMMI Physics Vol. 8 No. 4, 2021.

[43] H. Watabe et al., *PET kinetic analysis – compartmental model*, Annals of Nuclear Medicine Vol. 20 No. 9, 2006, pp. 583-588.

[44] M. Verona et al., *Preliminary Study of a 1,5-Benzodiazepine-Derivative Labelled with Indium-111 for CCK-2 Receptor Targeting*, Molecules Vol. 26 No. 918, 2021.

[45] https://bioemtech.com/ (consulted: August 2021).

[46] http://amide.sourceforge.net/ (consulted: August 2021).

[47] https://imagej.nih.gov/ij/ (consulted: August 2021).